Sympathetic Cooling of a Proton with Resonant Image Current Coupling

Heidelberg University

Matthew Bohman

November 6, 2020

Dissertation
submitted to the
Combined Faculty of Natural Sciences and Mathematics
of Heidelberg University, Germany
for the degree of
Doctor of Natural Sciences

Put forward by
Matthew Bohman
born in: Bellevue, WA
Oral examination: January 15, 2021

Abstract

This thesis is the realization of the long standing goal of sympathetically cooling single particles with image currents. Particles with no electronic structure such as the bare proton or antiproton, are not amenable to standard laser cooling and manipulation techniques and until now have been cooled only by coupling to cryogenic tank circuits. In measurements of the proton and antiproton g-factor however, the energy splitting used to read out the particle's spin state is larger than thermal energy fluctuations and special techniques are required to perform the measurement. The technique developed here uses a cloud of laser cooled beryllium ions to sympathetically cool a single proton by coupling to, and cooling a mode of the tank circuit. The use of this circuit resonantly enhances the energy exchange between the trapped particles and allows the cooling ions to be separated from the particle of interest over arbitrary distances. This technique, is the first demonstration of sympathetic cooling of a proton and a macroscopic LC circuit to below 25% of the environment temperature.

Sympathetically cooled protons and antiprotons with this method enable an improved g-factor measurement by increasing the duty cycle of the experiment. This will further our understanding of matter-antimatter asymmetry by constraining CPT odd new physics and enhancing sensitivity to even more exotic physics. Moreover, the technique presented here has general applications in experiments with trapped charged particles, enabling coupling of a large number of ions, distributed in many separated trapping regions to a single cold resonator.

Zusammenfassung

Diese These ist die Verwirklichung des langjährigen Ziels, einzelne gespeicherte Ionen mit Bildströmen sympathisch zu kühlen. Laserkühlungs- und etablierte Manipulationstechniken sind auf geladene Teilchen ohne eine geeignete elektronische Struktur nicht anwendbar und wurden nur durch Kopplung an kyrogene LC-Schwingkreise gekühlt. Bei Messungen des Protonen- und Antiprotonen g-Faktors ist die Detektion des Spinzustands herausfordernd, da winzige Rauschamplituden in der Falle eine eindeutige Bestimmung des Spinzustands nur bei Temperaturen weit unter der Temperatur von flüssigem Helium zulassen. Daher benötigen wir eine neue Kühltechnik um eine verbesserte g-Faktor Messung durchzuführen. Die hier entwickelte Technik verwendet eine Wolke aus lasergekühlten Berylliumionen, um ein einzelnes Proton durch Koppeln an und Abkühlen der LC-Schwingkreis durch die lasergekühlten Ionen sympathisch zu kühlen. Die Verwendung des LC-Schwingkreises verbessert den Energieaustausch zwischen den gespeicherten Ionen in Resonanz und ermöglicht deren Kühlung über beliebige Entfernungen zum lasergekühlten Teilchen. Diese Technik ist die erste Demonstration einer sympathischen Abkühlung eines Protons und eines makroskopischen LC-Kreislaufs auf unter 25% der Umgebungstemperatur.

Sympathisch gekühlte Protonen und Antiprotonen ermöglichen eine verbesserte g-Faktormessung durch einen schnelleren Messzyklus des Experiments. Dies wird das Verständnis der Asymmetrie zwischen Materie und Antimaterie weiter verbessern, indem eine mögliche Verletzung der CPT invarianz (kombinierte Ladung, Parität, und Zeitsymmetrie) eingeschränkt und die Empfindlichkeit für Effekte durch neue Physik erhöht wird. Darüber hinaus findet die hier vorgestellte Technik allgemeine Anwendung in Experimenten mit eingefangenen geladenen Teilchen, da sie zum Beispiel die Kopplung einer großen Anzahl von Ionen in vielen getrennten Fallen, die an einen einzelnen kalten Resonator angeschlossen sind ermöglicht.

Contents

List of Figures

List of Tables

Chapter 1

Introduction

Precision measurements of the properties of fundamental particles are unquestionably important in fundamental physics research. The anomalous magnetic moment of the electron, for example, helped motivate the development of quantum electrodynamics (QED), while the anomalous magnetic moment of the proton suggested that the proton had unexplained substructure. Moreover, precision measurements with fundamental particles lend themselves well to studying antimatter systems. In fact, high-precision comparisons of the properties of protons and antiprotons along with comparisons of electrons and positrons provide some of the most stringent constraints of CPT symmetry to date [1, 2, 3, 4].

The highest precision mass measurements and highest precision g-factor measurements are performed almost exclusively in Penning traps whose static fields and tractable equations of motion allow particle properties to be extracted using only image current detection systems. While certainly challenging experiments, the techniques used have lagged behind the rest of the atomic physics community, which has leaned more and more heavily on laser technology - whether in the form of precision laser spectroscopy, quantum state engineering, or preparation of ultracold particles. The work of my thesis was to take the some of the first steps to combine these two disparate yet sibling communities and to begin to bring some of the benefits of quantum control experiments with lasers to a precision Penning trap.

There has long been an idea of sympathetically laser cooling particles with no electronic structure - namely antiprotons - by coupling to laser cooled ions in another trap via image currents. First proposed in Ref. [5], coupling across large distances has been sought after in a wide variety of experimental contexts, e.g. quantum information [6], precision mass spectrometry [7], and precision spectroscopy [8]. Meanwhile sympathetic cooling of exotic particles is desired for precision spectroscopy on highly charged ions [9] and additional antimatter experiments with negative antihydrogen ions [10].

In the context of precision measurements in particular, the comparison of the proton and antiproton g-factors is uniquely sensitive to physics that violates the combined Charge-Parity-Time Symmetry (CPT), described in more detail in Chapter 2. A new generation of g-factor measurements began in 2014 with the first "double trap" measurement of the proton g-factor [11] with a precision of 9 ppb. Since then, the antiproton g-factor has also been measured with a precision of 1.5 ppb [3]. However, all of these measurements, including an improved measurement of the proton g-factor discussed in this thesis have been limited by long measurement times and high particle temperatures. In addition, frequency shifts due to magnetic field inhomogeneity will limit the precision of future experiments to around the 100 ppt level.

My thesis begins with the improved measurement of the proton g-factor which has been measured to a precision of 0.3 ppb using selective resistive cooling. In this method protons are prepared at low energy by coupling to a cryogenic circuit - typically taking around an hour per data point. The main focus of my work though, was realizing and improving the new sympathetic cooling technique in which a mode of a cryogenic circuit is cooled by laser cooled ions and ultimately used to cool the proton. This technique has achieved an axial temperature of $2.82^{+3.35}_{-2.82}\,\mathrm{K}$ - limited by the temperature resolution.

The structure of this thesis is, to a large extent, chronological. After providing the motivation for the proton and antiproton g-factor measurements, I discuss the theoretical foundations of Penning-trap experiments and summarize our measurement of the proton magnetic moment - the highest precision measurement of any nuclear magnetic moment to date. Then I show the next generation experimental apparatus used to implement sympathetic laser cooling and discuss the design, assembly, and commissioning processes which fully characterized the new experiment. From there I summarize the experiments demonstrating the laser cooling of beryllium ions including the first temperature measurement of laser cooled ions using the continuous Stern-Gerlach effect. Finally, I conclude with the capstone of my thesis work - the first sympathetic laser cooling of protons with a new resonant coupling technique and discuss a small number of possibilities for future experiments.

This thesis is the culmination of a large concerted effort but hopefully is just the beginning of a new generation of exciting experiments - with protons in Mainz and any number of trapped ion experiments.

Chapter 2

Motivation

It is well understood that the overabundance of matter compared to antimatter[1] is an enormous problem in our current understanding of the universe. As a result, the motivation for performing precision measurements on matter-antimatter pairs is clear: any deviation in these properties is an indication of new physics beyond the Standard Model of particle physics. In fact, this symmetry is linked to what we believe to be an even more fundamental symmetry - the combined Charge-Parity-Time (CPT) symmetry [13] that is a general property of all quantum field theories. What is less obvious though is why we measure the ratio of the proton-to-antiproton magnetic moments. After all, the relative precision of other matter-antimatter asymmetry experiments such as studies of kaon oscillations [14] or antihydrogen spectroscopy [15] can be orders of magnitude larger.

The answer is found by considering what happens to the Standard Model if CPT symmetry is violated. The Standard Model Extension (SME) [18, 19] is an effective field theory that perturbatively adds CPT odd and Lorentz symmetry violating terms to the Standard Model. Different systems have varying sensitivity to these CPT odd terms and measurements in Penning traps have been found to be particularly sensitive probes of CPT violating physics [20]. Fig. 2.1 shows these sensitivities in the most competitive systems and highlights the advantages of proton-antiproton comparisons in Penning traps. A particle in a Penning trap can be thought of as an artificial atom (see Chapter 3 for more details), with motional and spin energy levels analogous to electronic energy levels. As a result, if some of these CPT odd terms are nonzero, the energy levels of a proton in a Penning trap and those of an antiproton in a Penning trap will differ. Illustrated in Fig. 2.2, the a terms of the SME characterize an offset from the zero point energy while the b terms characterize an offset in the transition energies. More concretely, these energy

[1] This is characterized by the baryon photon ratio $\eta = \frac{N_B - N_{\bar{B}}}{N_\gamma} \approx \frac{N_B}{N_\gamma}$, which is found experimentally to be nearly ten orders of magnitude too large with $N_{\bar{B}}$ also inexplicably small. For a theoretical review, including the Sakharov conditions that describe how a matter-antimatter asymmetry can arise, see [12].

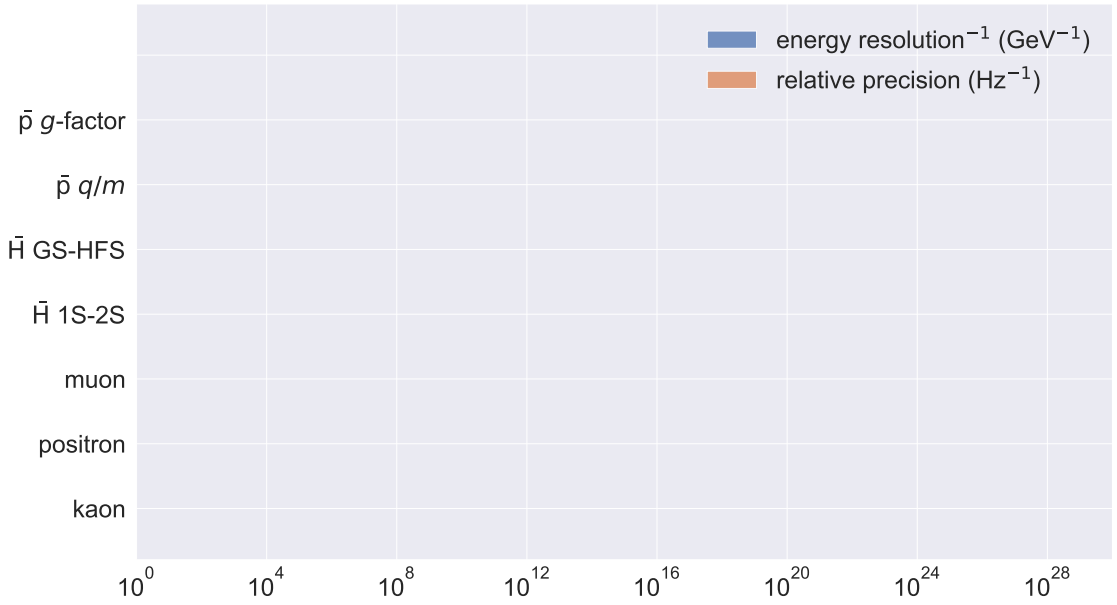

Figure 2.1: The relative precision and energy resolution of matter-antimatter comparisons are given and the top two measurements, with antiprotons are performed by the BASE collaboration. The limits are given in [3, 1, 16, 16, 17, 4, 14] from top to bottom, respectively. Measurements with antiprotons are highly sensitive to new physics on an absolute energy scale.

levels can be cyclotron energy levels in a magnetic field or spin energy levels. In our case, the measurement of the ratio of the proton magnetic moment to the antiproton magnetic moment is sensitive to both through the relation

$$\vec{\mu} = g\frac{e}{2m}\vec{S}. \tag{2.1}$$

The dimensionless g-factor is given by

$$g = 2\frac{\omega_L}{\omega_c} \tag{2.2}$$

where ω_L, ω_c are the Larmor and free cyclotron frequencies in a magnetic field with energy levels $E_L = \hbar\omega_L$, $E_c = \hbar\omega_c$. Details about measurements of the free cyclotron and Larmor frequencies are described in Chapter 3 and a description of the g-factor measurement can be found in Chapter 4.

As a result, precision measurements of exactly this quantity are the main focus of this thesis and of the BASE collaboration in general [21]. The BASE collaboration performs precision measurements on antiprotons and negative hydrogen ions at the Antiproton Decelerator (AD) facility at CERN and precision measurements protons at the University of Mainz[2]. As part of the collaboration, my work

[2]The remaining group of the collaboration (along with collaborators at the Max Planck Institute for Nuclear Physics (MPIK) and RIKEN) is based at the University of Hannover and is focused on developing new measurement techniques based on quantum logic spectroscopy (QLS) [8].

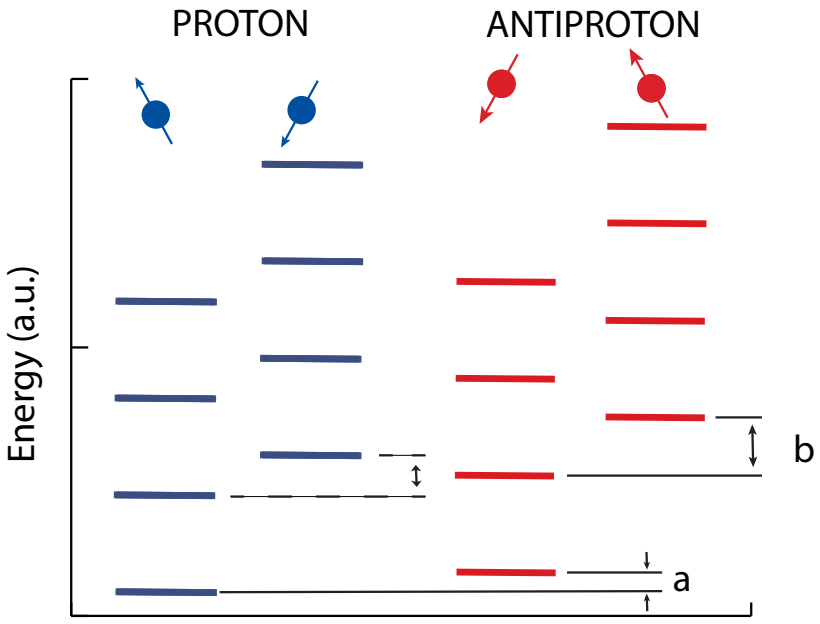

Figure 2.2: The Standard Model Extension (SME) characterizes the changes in energy levels, illustrated here not to scale, due to nonzero CPT odd interaction terms for the proton and antiproton in a Penning trap. The a terms quantify the difference in ground state energies while the b terms quantify the difference in transition energies. See text for details.

during the course of this thesis has been focused on developing a new technique that will allow measurements of the proton and antiproton g-factor to be performed at higher duty cycle and even higher precision. A major problem in the latest measurement was the large amount of time it took to prepare a cold particle - described in more detail in Chapter 3 and Chapter 4. In fact, this was the limiting factor of our measurement, the error of which is still dominated by statistics. Meanwhile further precision will also be limited by the temperature of the proton in an inhomogenous magnetic field. The sympathetic cooling techniques developed in this thesis have been designed with the primary goal of improving this measurement. Improved statistics will directly improve the precision of the proton and antiproton g-factor measurements and the high duty cycle can enable even more experiments, such as improving our recent limits on exotic antimatter couplings to dark matter [22]. Without further delay then, the main content of this thesis follows, beginning with a theoretical understanding of the Penning traps that are the foundation of all these experiments.

Chapter 3

Theoretical Background

3.1 Penning Traps

3.1.1 Potential and Motion

Earnshaw's Theorem disallows the creation of an electrostatic potential with a three dimensional minimum and, in the absence of charge, Gauss's law states

$$\nabla \cdot \mathbf{E} = 0. \tag{3.1}$$

Of course, traps for charged particles do exist. In an rf, or Paul trap, for example, the trapping potential is created by introducing a time-varying potential while in a Penning trap an additional magnetic force traps causes the particle to move around the axial potential. Developed by Hans Dehmelt in the early 1960s but proposed as early as 1947 in a patent application [23], the Penning trap has proven to be uniquely suited to precision measurements. Using only static fields, Penning traps have extremely low heating rates, and even more importantly relate the fundamental properties of a charged particle to easily measurable trap frequencies[1].

A particle with charge q and mass m in a magnetic field $\mathbf{B}$ and electric field $\mathbf{E}$ is subject to the Lorentz force

$$\mathbf{F} = q\left(\mathbf{E} + \mathbf{v} \times \mathbf{B}\right). \tag{3.2}$$

A Penning trap is constructed by choosing the magnetic field to be along the z-axis, $\mathbf{B} = B_0\hat{z}$, of geometrically well-defined electrodes that produce an axial potential,

$$\phi = V_r C_2 \left(z^2 - \frac{r}{2}\right) \tag{3.3}$$

[1]Note that this thesis follows the semi-established tradition of using angular frequencies, ω_i in theoretical contexts and frequency ν in experimental contexts.

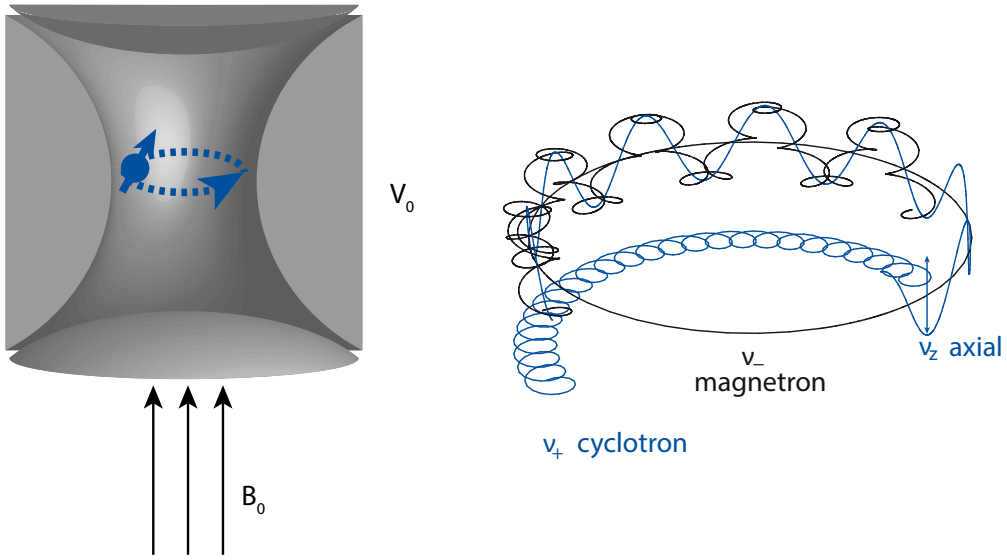

(a) (b)

Figure 3.1: **(a)** An illustration of a Penning trap, with electrostatic fields that give rise to three nearly harmonic oscillatory motions. This potential, V_0 can be applied to physical, hyperbolic electrodes or can be approximated by a series of cylindrical electrodes, shown later. **(b)** The motion of the particle is pictured, a combination of the magnetron, axial, and cyclotron motion.

in cylindrical coordinates. In Fig. 3.1, $V_r = V_0$ is the applied voltage and C_2 is a constant defined by the electrode geometry. The axial motion then decouples from the radial motion and, following [24], yields an axial equation of motion,

$$\ddot{z} = -\omega_z^2 z, \tag{3.4}$$

with,

$$\omega_z^2 = \frac{2qC_2V_0}{m}. \tag{3.5}$$

The radial motion is found by solving the equations of motion in Cartesian coordinates,

$$\ddot{y} = \frac{q}{m}\left(C_2V_0x + B_0\dot{y}\right) \tag{3.6}$$

$$\ddot{x} = \frac{q}{m}\left(C_2V_0y + B_0\dot{x}\right) \tag{3.7}$$

with the resulting eigenvalues given by

$$\omega_\pm = \frac{\omega_c}{2} \pm \frac{1}{2}\sqrt{\omega_c^2 - 2\omega_z^2}. \tag{3.8}$$

Finally, ω_c is the free cyclotron frequency

$$\omega_c = \frac{q}{m}B_0. \tag{3.9}$$

The three trap frequencies, ω_+, ω_z, and ω_- are known as the modified cyclotron, axial, and magnetron frequencies, respectively and follow the hierarchy $\omega_+ > \omega_z > \omega_-$ under typical trapping conditions. From Eq. (3.8) the trapping criterion is clear: $\omega_\pm$ is complex unless $\omega_z \leq \omega_c/\sqrt{2}$, setting an upper bound on trap stability in the absence of trap imperfections. Still following [24], an important set of equations arise in the presence of trap imperfections. These imperfections are characterized by parameters ϵ, which defines the ellipticity of the trapping potential and θ, ϕ defined by,

$$\begin{aligned} B_z &= |\mathbf{B}| \cos\theta \\ B_x &= |\mathbf{B}| \sin\theta \cos\phi \\ B_y &= |\mathbf{B}| \sin\theta \sin\phi. \end{aligned} \tag{3.10}$$

Finally, after relabeling the observed axial frequency as ω_z and the constant in Eq. (3.5) as ω_v, the complete equations of motion are then,

$$\mathbf{F} = \begin{pmatrix} \omega^2 + \frac{1}{2}\omega_v^2\left(1+\epsilon\right) & -i\omega_c\cos\theta & i\omega\omega_c\sin\theta\sin\phi \\ i\omega_c\cos\theta & \omega^2 + \frac{1}{2}\omega_v^2\left(1+\epsilon\right) & -i\omega\omega_c\sin\theta\cos\phi \\ -i\omega\omega_c\sin\theta\sin\phi & i\omega\omega_c\sin\theta\cos\phi & \omega^2 - \omega_v^2 \end{pmatrix}. \tag{3.11}$$

Eigenvalues are again given by ω_z, ω_-, and ω_+, which obey the relations

$$\omega_+^2\omega_z^2\omega_-^2 = \frac{1}{4}\omega_v^6\left(1-\epsilon^2\right) \tag{3.12}$$

$$\omega_+^2\omega_z^2 + \omega_+^2\omega_-^2 + \omega_z^2\omega_-^2 = \omega_c^2\omega_v^2\left(1 - \tfrac{3}{2}\sin^2\theta - \tfrac{1}{2}\epsilon\sin^2\theta\cos 2\theta\right) - \frac{3}{4}\omega_v^4\left(1+\tfrac{1}{3}\epsilon^2\right) \tag{3.13}$$

$$\omega_+^2 + \omega_z^2 + \omega_-^2 = \omega_c^2. \tag{3.14}$$

Particularly important is Eq. (3.14). Known as the invariance theorem [24], it directly relates the observable trap frequencies to the mass of the trapped particle. Since the magnetic field is not known to high precision, both g-factor measurements and mass measurements measure frequency ratios. In mass measurements, this is simply the ratio of the cyclotron frequencies of the two ions of interest:

$$\frac{m_1}{m_2} = \frac{\omega_{c,1}}{\omega_{c,2}}. \tag{3.15}$$

However, for g-factor measurements the Larmor, or spin precession, frequency

$$\omega_L = g\frac{q}{2m}B_z, \tag{3.16}$$

must be used, and the g-factor can be extracted from the ratio of Larmor frequency to cyclotron frequency,

$$g = 2\frac{\omega_L}{\omega_c}. \tag{3.17}$$

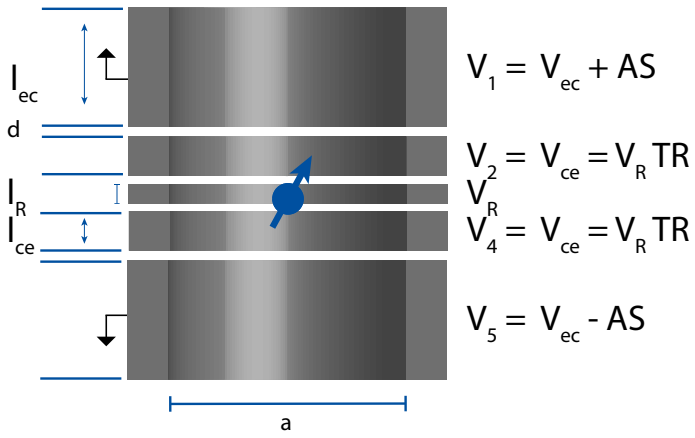

Figure 3.2: A cylindrical, open endcap Penning trap. All measurements described in this thesis are conducted with a similar five electrode trap with an orthogonal, compensated design as described in the text.

3.1.2 The Cylindrical Penning Trap

In the first Penning traps, hyperbolic electrodes produced the electric field C_2V_0 used in Eqs. (3.5 - 3.7) - illustrated in Figure 3.1. Most modern traps however, now use a multi-electrode cylindrical configuration. For the proton g-factor experiment specifically, we use a cylindrical, five electrode design as in Figure 3.2. The derivation of the trapping potential has been done many times, e.g. in [24, 25], but the main results are summarized here.

The axial potential in our experiment is produced by a stack of five open cylindrical electrodes consisting of a central ring electrode, surrounded by two identical correction electrodes, and two identical endcap electrodes. The endcap electrodes are typically kept at 0 V and as in [26], the total potential of a stack of $p = 5$ such electrodes separated by a gap d can be written as

$$\Phi(\rho, z) = \frac{2}{\Lambda}\sum_{n=1}^{\infty}\left[\frac{V_1\cos k_n z_0 - V_p\cos k_n\Lambda}{k_n} + \sum_{i=2}^{p}\frac{V_i - V_{i-1}}{k_n^2 d}\sin k_n z_{2i} - \sin k_n z_{2i-1}\right] \times \frac{I_0(k_n\rho)}{I_0(k_n a)}\sin k_n z. \quad (3.18)$$

Here the coordinates defined in Fig. 3.2 and I_0 is the modified Bessel function of the first kind. Eq. (3.18) can then be expanded in terms of the coefficients C_j and the potential can be rewritten as

$$\Phi(0, z) = V_0\sum_{j=0}^{n} C_j z^j \quad (3.19)$$

with

$$C_j = \frac{1}{j!\Lambda V_0}\sum_{n=1}^{n}\left[\frac{V_1 k_n z_0 - V_5 k_{n\Lambda}}{k_n} + \sum_{i=2}^{5}\frac{V_i - V_{i-1}}{k_n^2 d}\left(\sin k_n z_{2i} - \sin k_n z_{2_{i-1}}\right)\right] \times \frac{(n\pi/\Lambda)^j}{I_0\left(k_n a\right)\sin\frac{\pi}{2}\left(n+j\right)}. \quad (3.20)$$

Again, the endcap voltages are set to $V_1 = V_5 = V_{ec} = 0$ while the correction electrode voltages are set to $V_2 = V_4 = V_{ce}$, and the ring voltage is set to to $V_3 = V_0 = V_r$. A tuning ratio, $\mathrm{TR} = V_{ce}/V_r$, is then defined so that the C_j coefficients can be written as

$$C_j = E_j + D_j\,\mathrm{TR}. \quad (3.21)$$

Precision Penning traps are also designed to be simultaneously "compensated" and "orthogonal". A careful selection of the trap radius a, ring electrode length l_r, and correction electrode length l_{ce} produces an ideal tuning ratio, $\mathrm{TR_{id}}$. At this tuning ratio, $C_4(\mathrm{TR_{id}}) = C_6(\mathrm{TR_{id}}) = 0$ with odd coefficients also zero due to mirror symmetry about the trap center. Although not used in this work, traps have also been designed and used in recent experiments [27, 28, 29], that have seven electrodes to null higher order C_8 and C_{10}. It is not strictly necessary to ground the endcap electrodes although this configuration produces the lowest fluctuations in trapping potential due to voltage supply noise. In the course of this work, the endcap electrodes have occasionally been set to positive voltage to achieve lower equivalent ring voltages, and the correction electrodes have occasionally been set to $V_{ce} = 0$ to overcome technical limitations. In each configuration the tuning ratio TR is replaced by an effective tuning ratio so that Eq. (3.21) still holds. C_2 is the dominant coefficient determining the axial frequency, which is also a function of applied voltage and tuning ratio. In a compensated trap D_2 is zero, while E_2 is a constant offset that accounts for roughly 97% of the value of C_2.

C_4, and additional higher order terms, give rise to energy dependent shifts of the axial mode. These are characterized by the matrix equation [30]

$$\begin{pmatrix}\Delta\omega_+/\omega_+\\ \Delta\omega_z/\omega_z\\ \Delta\omega_-/\omega_-\end{pmatrix} = \mathcal{M}_{C_4}\begin{pmatrix}E_+\\ E_z\\ E_-\end{pmatrix} + \mathcal{M}_{C_6}\begin{pmatrix}E_+^2\\ E_z^2\\ E_-^2\\ E_+E_z\\ E_+E_-\\ E_zE_-\end{pmatrix} + \mathcal{O}\left(C_8\right), \quad (3.22)$$

where $\Omega = \omega_z/\omega_+$,

$$\mathcal{M}_{C_4} = \frac{1}{qV_0}\frac{C_4}{C_2^2}\begin{pmatrix} \frac{3}{4}\Omega^4 & -\frac{3}{2}\Omega^2 & -3\Omega^2 \\ -\frac{3}{2}\Omega^2 & \frac{3}{4} & 3 \\ -3\Omega^2 & 3 & 3 \end{pmatrix}, \tag{3.23}$$

(3.24)

and

$$\mathcal{M}_{C_6} = \frac{1}{qV_0}\frac{C_6}{C_2^3}\begin{pmatrix} -\frac{15}{16}\Omega^6 & -\frac{45}{16}\Omega^2 & \frac{45}{8}\Omega^4 & \frac{45}{4}\Omega^4 & \frac{45}{4}\Omega^4 & -\frac{45}{2}\Omega^2 \\ -\frac{45}{16}\Omega^4 & \frac{15}{16} & \frac{45}{4} & -\frac{45}{8}\Omega^2 & -\frac{45}{2}\Omega^2 & \frac{45}{4} \\ -\frac{45}{8}\Omega^4 & \frac{45}{8} & \frac{15}{2} & -\frac{45}{2}\Omega^2 & -\frac{45}{2}\Omega^2 & \frac{45}{2} \end{pmatrix}. \tag{3.25}$$

In practice, C_4 and C_6 as a function of ΔTR, the offset in the applied tuning ratio to the ideal tuning ratio, $\mathrm{TR}_{\mathrm{applied}} = \mathrm{TR}_{\mathrm{id}} + \Delta\mathrm{TR}$. It is useful though to introduce here the notation used throughout this thesis of κ_i - the frequency shift due, $\Delta\mathrm{TR}\,\Delta T_i$ where ΔT_i is the temperature of one of the motional modes or E_i/k_{B}. For example, in later chapters we measure shifts of the axial frequency $\Delta\nu_z = k_{D_4}\Delta\mathrm{TR}\,T_z$. These shifts are extremely important in characterizing the trap and are used in temperature measurements in later chapters.

Due to patch potentials and extraneous charges that can build up on the surface of the electrodes, the particle motion can also be offset from the center of the trap. We then introduce asymmetry parameters for the correction and endcap electrodes AS_{ce} and AS_{ec}, defined by

$$\begin{aligned} V_{1,5} &= V_{ec} \pm AS_{ec} \\ V_{2,4} &= V_{ce} \pm AS_{ce}. \end{aligned} \tag{3.26}$$

As a result, the trapping potential is fully characterized by four parameters that can be adjusted independently: V_r, TR, AS_{ce}, AS_{ec} [26]. As shown in Chapter 6, these parameters define the harmonicity of the trapping potential and are crucial to setting up a new Penning trap experiment.

3.1.3 Image Current Detection and the Circuit Model

The modified cyclotron, axial, and magnetron motions can be modeled as decoupled simple harmonic oscillators. Following [31, 32], we further model the trapped ion system as an LC circuit with inductance and capacitance,

$$l = \frac{m{D_{\mathrm{eff}}}^2}{Nq^2}, \tag{3.27}$$

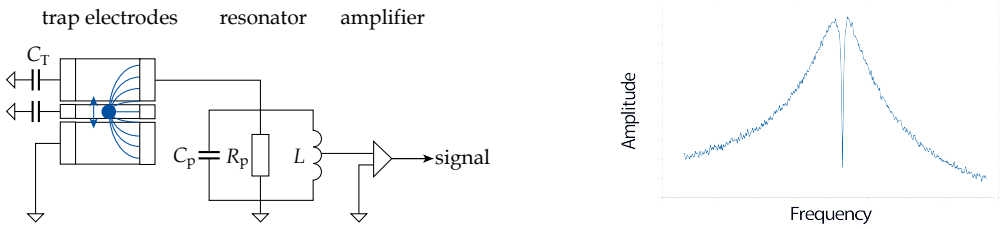

(a) (b)

Figure 3.3: **(a)** A trapped particle can be modeled as a series LC circuit coupled in parallel to a high-Q resonator and a cryogenic amplifier that reads out the image current signal. **(b)** The frequency spectrum of the particle-resonator system has a characteristic dip feature and on resonance the particle shorts to the noise spectrum of the resonator.

$$c = \frac{1}{\omega_z^2 l}, \tag{3.28}$$

respectively. Here D_{eff} is the characteristic length scale of the trap and N is the number of stored ions. A trapped charged particle induces image charges on the trapping electrodes and particle oscillations give rise to image currents which can be read out by a current detector. In practice, this is achieved by connecting a high-Q, superconducting resonator to the trap with resonant frequency $\omega_D \approx \omega_z$.

Using this circuit model, the system can then be treated as a series LC circuit connected in parallel to the parallel RLC circuit of the detection system. Under this modification the ion-trap system is damped with damping constant,

$$\gamma = \frac{q^2}{D_{\text{eff}}^2}\frac{R}{m}. \tag{3.29}$$

Here, R is the effective resistance of the resonator, $R = Re\,(Z) = Q\omega L$. D_{eff} is known as the effective electrode distance [33] and is equivalent to the charge induced by the particle in a parallel plate capacitor separated by distance D_{eff}.

The equation of motion for the axial mode then needs to be modified and Eq. (3.4) becomes,

$$m\left(\ddot{z} - \gamma\dot{z} + \omega_z^2 z\right) = F_{\text{noise}}, \tag{3.30}$$

where F_{noise} is the force of the detection system on the trapped particle due to the combined Johnson and amplifier noise with effective temperature, T. The solution to Eq. (3.30) has a transient and steady state solution and the axial frequency ω_z remains, to high approximation, unchanged. Finally, the axial amplitude is given by [24],

$$\left\langle z^2 \right\rangle = \frac{E_z}{2m\omega_z} \tag{3.31}$$

where the axial energy is $E_z = k_B T_z$. Likewise, the radius of the other radial modes

is given by,

$$\begin{aligned} r_-^2 &= \frac{-E_-}{\frac{1}{2}m\left(\omega_-^2 - \frac{1}{2}\omega_z^2\right)} \\ r_+^2 &= \frac{E_+}{\frac{1}{2}m\omega_+^2}. \end{aligned} \tag{3.32}$$

Notably, as is evident from Eq. (3.32), the energy in the magnetron mode is negative and the Penning trap is only pseudo-stable due to radiative damping. The damping constants describing the radiation are [24],

$$\begin{aligned} \gamma_+ &= \frac{4q^2\omega_+^2}{3mc^3}\frac{\omega_+}{\omega_+ - \omega_-} \\ \gamma_- &= \left(\frac{\omega_-}{\omega_+}\right)^3 \gamma_+ \, l \end{aligned} \tag{3.33}$$

and can be safely ignored for heavy particles with mass $m \gg m_e$.

In addition to damping, the resonator allows the trap frequencies to be easily read out via image current detection. Considering only the case of the axial motion, the current induced by the particle coupled to the resonator with damping constant γ is given by [33],

$$J_z = A_z \sin \omega_z t \, \gamma. \tag{3.34}$$

On resonance, the particle-detector system are impedance matched and the power dissipated in the detector can be written as

$$\langle P \rangle = J_z^2 R = k_B T_{\text{noise}} \Delta f. \tag{3.35}$$

Again T_{noise} is the noise temperature of the resonator-amplifier system, typically near 4 K but in some cases higher due to feedback. Substituting Eq. (3.29) and Eq. (3.31), $T_z = T_{\text{noise}}$ and the lineshape of the frequency spectrum of two coupled oscillators is well known [24]. On resonance the particle acts as a short or "dip" with bandwidth Δf given by the damping γ, or equivalently the dip width. After passing through both a cryogenic and room temperature amplification stage the signal is fed to an FFT analyzer[2] - an example is shown in Fig. 3.3.

3.1.4 The Artificial Atom

It is useful at this point to introduce the view of a trapped particle in a Penning trap as an artificial atom. The three modes are independent harmonic oscillators (or quasi-harmonic in the case of the radial modes) and easily quantized, with the

[2] in this work a Stanford Research SR780

result that [24]

$$
\begin{aligned}
|E_-| &= \hbar\omega_- \left(n_- + \frac{1}{2}\right) \\
E_z &= \hbar\omega_z \left(n_z + \frac{1}{2}\right) \\
E_+ &= \hbar\omega_+ \left(n_+ + \frac{1}{2}\right).
\end{aligned}
\tag{3.36}
$$

Here, n_- ,n_z,and n_+ are the quantum numbers of the energy eigenstates $|-\rangle$, $|z\rangle$, and $|+\rangle$ of the magnetron, axial, and cyclotron modes, respectively, in analogy to atomic quantum numbers, for example F, m_J, l.

In addition, a particle with magnetic moment μ interacts with the magnetic field with the spin Hamiltonian,

$$H_s = -\mu \cdot \mathbf{B} = \frac{g}{2}\hbar\omega_c\sigma_z, \tag{3.37}$$

where σ_z is the spin projection onto the z-axis. For spin-$\frac{1}{2}$ particles, there are two energy eigenstates $s = \pm 1$ and the energy eigenvalues are given by,

$$E_s = \frac{g}{2}\hbar\omega_c\frac{s}{2}, \tag{3.38}$$

with spin precession frequency,

$$\omega_s = \frac{g}{2}\omega_c. \tag{3.39}$$

These frequencies, to rough approximation, are given in Table 3.1, with the experimental values in the Appendix. The trapped particle has energy levels and splittings as shown in Fig. 3.4 - again similar to the hydrogen atom with discrete energy levels, fine structure, hyperfine structure, and Zeeman and Stark shifts. Much of the earlier work done with Penning traps, famously [24], explicitly call the system "geonium", with the earth replacing the heavy particle of other "true" -oniums [3].

3.1.5 Particle Manipulation

Importantly, the motion of a particle in a Penning trap can be modified and excited at rf frequencies near the motional frequencies. Although covered extensively in the literature [35, 36], a few basic results are reproduced here.

[3] Nobel Prize winner and inventor of the Penning trap, Hans Dehmelt also proposed the idea of "cosmonium" in an incredible article titled *Triton,... electron,... cosmon,...: An infinite regression?* in which the decay of the cosmonium atom, the bound state of a cosmon and anticosmon, produces the Big Bang [34].

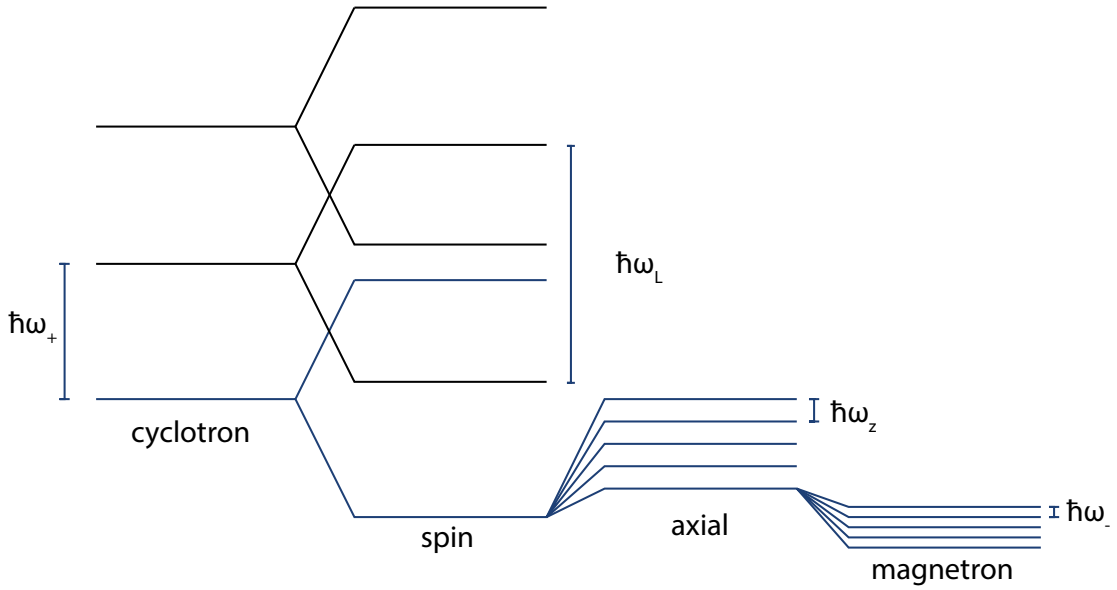

Figure 3.4: Illustrated here (not to scale) are the energy levels of a single particle in a Penning trap. These energy levels and splittings are analogous to atomic energy levels subject to e.g. Zeeman and Stark splittings.

	ω_L	ω_c	ω_+	ω_z	ω_-
p	$2\pi \times 80\,\mathrm{MHz}$	$2\pi \times 30\,\mathrm{MHz}$	$2\pi \times 30\,\mathrm{MHz}$	$2\pi \times 500\,\mathrm{kHz}$	$2\pi \times 10\,\mathrm{kHz}$
Be^+	$2\pi \times 60\,\mathrm{GHz}$	$2\pi \times 3\,\mathrm{MHz}$	$2\pi \times 2.5\,\mathrm{MHz}$	$2\pi \times 500\,\mathrm{kHz}$	$2\pi \times 30\,\mathrm{kHz}$

Table 3.1: Approximate frequencies of the proton and beryllium ion in a 2 T magnetic field axial frequencies near those used in all traps in the proton g-factor experiment. With the exception of the Larmor and free cyclotron frequencies the exact frequencies depend on the specific axial frequency used in each trap which vary from about 475 kHz to about 750 kHz. Additionally, note that ω_L for the beryllium ion, refers to the Larmor frequency of the valence electron, not the nucleus.

Parametric Excitation

In the presence of an additional rf drive, the most basic equation of motion for the axial mode, Eq. (3.4), becomes [37],

$$\dot{z} + \gamma\dot{z} + \omega_v \left(1 + A_{\mathrm{rf}} \cos(\omega_{\mathrm{rf}} t)\right) z + \frac{2C_4}{C_2}\omega_z^2 z^3 + \frac{3C_6}{C_2}\omega_z^2 z^5 = 0, \tag{3.40}$$

where A_{rf} and ω_{rf} are the amplitude and frequency of the excitation drive respectively. The particles then obey the Mathieu equation and have instability regions

where,

$$\omega_{\mathrm{rf}} = \frac{2\omega_v}{n}. \tag{3.41}$$

The result is that above a threshold defined by the coupling to the resonator, $A_{\mathrm{rf}} > 2\gamma_z/\omega_z$, the motion is bistable, the motional phase locks to the drive phase, and the motion amplitude grows without bound - ultimately limited by C_4 anharmonicities. The axial motion appears as a peak in the FFT spectrum, as in Fig. 3.5, and is an invaluable tool for trap characterization.

Sideband Coupling

Another critical tool for high-precision Penning-trap experiments is a quadrupolar drive that couples motional modes through their sidebands. These sidebands are $\omega_{\mathrm{SB}} = \omega_i \pm \omega_j$ where $\omega_{i,j}$ indicate the relevant motional frequencies. For example, the modified cyclotron motion has a lower axial sideband at $\omega_{SB,+} = \omega_+ - \omega_z$. Following [36], a quadrupolar drive at frequency ω_{rf} detuned by $\delta = \omega_{\mathrm{rf}} - \omega_+ + \omega_z$ produces an electric field,

$$\mathbf{E}_{rf} = \mathbf{Re}\left(E_{rf} \mathrm{e}^{i\omega_{\mathrm{rf}} t}\right)\left(x\hat{\mathbf{z}} + z\hat{\mathbf{x}}\right). \tag{3.42}$$

The equation of motions in the x- and z- direction can be written as,

$$\begin{aligned} \ddot{z} + \omega_z^2 z &= \mathbf{Re}\left(\frac{eE_{\mathrm{rf}}}{m} e^{i\omega_{\mathrm{rf}} t} x\right) \\ \ddot{x} + \omega_+^2 z &= \mathbf{Re}\left(\frac{eE_{\mathrm{rf}}}{m} e^{i\omega_{\mathrm{rf}} t} z\right), \end{aligned} \tag{3.43}$$

with solutions [26],

$$\begin{aligned} z\left(t\right) &= z_0 \sin\left(\frac{\Omega_R}{2} t\right) \sin(\omega_z t + \phi_z) \\ r_+\left(t\right) &= r_{+,0} \cos\left(\frac{\Omega_R}{2} t\right) \sin(\omega_+ t + \phi_+). \end{aligned} \tag{3.44}$$

The Rabi frequency,

$$\Omega_R^2 = \frac{qE_{\mathrm{rf}}}{2m\sqrt{\omega_z \omega_+}} + \delta^2, \tag{3.45}$$

is set by the drive amplitude that produces the electric field, E_{rf}, and the phases, $\phi_{z,+}$, are determined by initial conditions. The quadupolar drive at the sideband frequency leads, in the language of [36], to the exchange of the classical action - equivalent to energy exchange. However, the application of the upper sideband $\omega_{\mathrm{rf}} \approx \omega_+ + \omega_z$, results not in oscillations between the two modes but in the continual transfer of energy from the axial mode to the modified cyclotron mode. Just as in a classical oscillator or a two-state quantum harmonic oscillator, the Rabi frequency is the rate at which the motional amplitude, or energy, is modulated between $A(E =$

E_0) to $A(E = E_z + E_+)$. The same reasoning also applies to the magnetron mode, although the negative energy of the mode reverses the role of the upper and lower sidebands. With sufficiently long coupling times, $t_{\text{coupling}} \gg \Omega_R^{-1}$, the expectation value of the energy of the coupled modes is given by

$$\frac{\langle E_i \rangle}{\langle E_j \rangle} = \frac{\omega_i}{\omega_j}, \tag{3.46}$$

or equivalently,

$$\frac{T_i}{T_j} = \frac{\omega_i}{\omega_j}. \tag{3.47}$$

While a sideband drive is applied the dip spectrum of the particle splits in two, as shown in Fig. 3.5, and as expected from amplitude modulated oscillations. The dip positions also enable measurement of the radial frequencies through the relation

$$\omega_\pm = \pm\omega_l \pm \omega_r \pm \omega_z + \omega_{\text{rf}}, \tag{3.48}$$

where ω_l and ω_r are the left and right dip positions given, respectively, by

$$\omega_l = \omega_z \mp \frac{\delta}{2} - \frac{\Omega_R}{2} \tag{3.49}$$

$$\omega_r = \omega_z \mp \frac{\delta}{2} + \frac{\Omega_R}{2}. \tag{3.50}$$

Finally, sideband coupling can also be used as a cooling method. Assuming an axial resonator at roughly 500 kHz and 4 K, a magnetron temperature of $T_- < 1\,\text{K}$ is easily achievable for both the proton and beryllium ion. On the other hand, the cyclotron temperature is much higher with $T_+ \approx 150\,\text{K}$ for the proton and $T_+ \approx 50\,\text{K}$ for the beryllium ion. These energies are more than sufficient for the magnetron and axial modes, but the cyclotron mode must be significantly below 4 K to resolve spin states. This requires either an additional tuned circuit connected to the trap at the modified cyclotron frequency or an external cooling method, such as laser cooling.

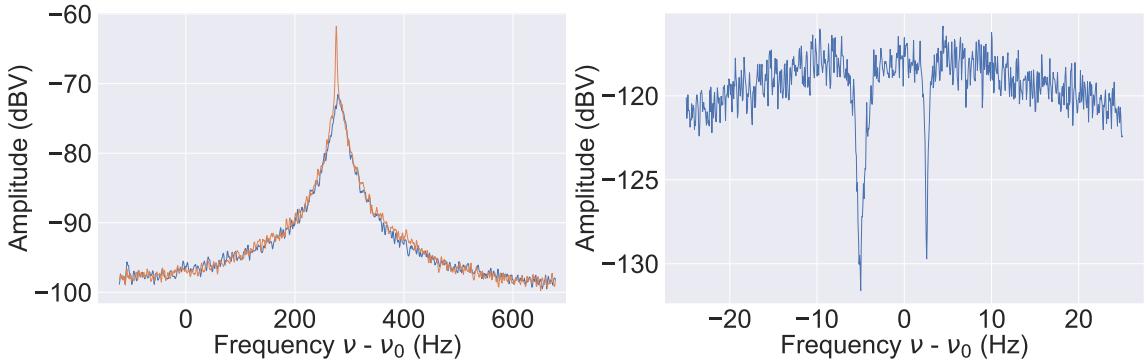

(a) (b)

Figure 3.5: **(a)** A parametric excitation at $2\omega_z$ produces a peak (in orange) in the FFT spectrum, with the undisturbed resonator (in blue) shown for reference. See text for details. **(b)** During sideband coupling the particle appears as two dips separated by the Rabi frequency Ω_R. The two dips are slightly asymmetric around the axial frequency at $\nu_z = \nu_0$.

3.2 Continuous Stern-Gerlach Effect and Magnetic Bottle

3.2.1 Essentials

Perhaps the most important tool in the precision Penning-trap toolbox is the continuous Stern-Gerlach effect [38] which allows non-destructive measurement of the trapped particle's spin state. In our case, this is implemented in a purpose-built trap known as the Analysis Trap (AT). By replacing the ring electrode with an identical, ferromagnetic electrode the magnetic field drops in proportion to to the magnetic saturation. Using a CoFe ring electrode[4] with magnetic saturation around two Tesla, the magnetic bottle reduces the field strength to around 1.2 T - illustrated in Fig. 3.6. The magnetic field gradient can then be written as,

$$\mathbf{B}(z, r) = B_0\,\hat{z} + B_2\left(\left(z^2 - r^2/2\right)\hat{z} - z\,\mathbf{r}\,\hat{z}\right), \tag{3.51}$$

where, $B_{2,\mathrm{AT}} \approx 298\,000\,\mathrm{Tm}^{-2}$. As in [24], the interaction term $-\mu \cdot \mathbf{\Delta B}$ gives rise to an interaction Hamiltonian,

$$\Delta H\,(r = 0, z) = -\mu\,B_2\,z^2. \tag{3.52}$$

It becomes evident that introducing a nonzero B_2 causes the axial motion to depend on the energy of the magnetic moment in the inhomogenous magnetic field. The magnetic moment μ is, of course, the intrinsic spin magnetic moment of the trapped

[4] VACOFLUX from VACUUMSCHMELZE GmbH

particle, μ_s, but also contains the classical magnetic moment of a charged particle in a magnetic field,

$$\mu = \mu_s + \mu_+ + \mu_-. \tag{3.53}$$

Here $\mu_\pm$ are the magnetic moments associated with the current loops of the modified cyclotron and magnetron motions. Each component of μ shifts trap frequencies and the Larmor frequency by [24, 30],

$$\begin{pmatrix} \Delta\omega_+/\omega_+ \\ \Delta\omega_z/\omega_z \\ \Delta\omega_-/\omega_- \\ \Delta\omega_L/\omega_L \end{pmatrix} = \frac{1}{m\omega_z^2}\frac{B_2}{B_0}\mathcal{M}_{B_2}\begin{pmatrix} E_+ \\ E_z \\ E_- \end{pmatrix}. \tag{3.54}$$

.

Again, $\Omega = \omega_z/\omega_+$ and

$$\mathcal{M}_{B_2} = \frac{1}{m\omega_z^2}\frac{B_2}{B_0}\begin{pmatrix} -\Omega^2 & 1 & 2 \\ 1 & 0 & -1 \\ 2 & -1 & -2 \\ -\Omega^2 & 1 & 2 \end{pmatrix} + \mathcal{O}\left(B_4\right). \tag{3.55}$$

Importantly, the shift of the axial frequency due to the spin state of the proton can then be read out as,

$$\Delta\omega_z = \frac{\hbar}{2m\omega_-}\frac{B_2}{B_0}\frac{\omega_c}{\omega_+ - \omega_-}\left(\frac{gs}{4} + n_+ + \frac{1}{2} + \frac{\omega_-}{\omega_+}\left(n_- + \frac{1}{2}\right)\right). \tag{3.56}$$

The particle is assumed to be spin-1/2, with $s = \pm 1$ and g-factor, g. Thus a change in axial frequency is quantized and arises from a change in the spin, cyclotron, or magnetron quantum number, expressed as $\Delta\omega_z/\Delta s$, $\Delta\omega_z/\Delta n_+$, and $\Delta\omega_z/\Delta n_-$, respectively. The axial frequency and dip signal can also be "smeared out" by fluctuations in the trapping potential leading to axial frequency fluctuations expressed as $\Delta\omega_{z,v}$. For the proton in the AT we have the hierarchy

$$\frac{\Delta\omega_z}{\Delta s} > \frac{\Delta\omega_z}{\Delta n_+} > \Delta\omega_{z,v} \gg \frac{\Delta\omega_z}{\Delta n_-}, \tag{3.57}$$

and parameters for the AT are summarized in Table 3.2.

3.2.2 Frequency Stability and Transition Rates in the AT

For the proton, $\Delta\omega_z/\Delta s$ is less than three times larger than $\Delta\omega_z/\Delta n_+$. As a result, no more than three cyclotron transitions can occur during a measurement of the axial frequency - typically around a minute, but determined by the optimal FFT averaging time.

	$\Delta\nu_{z,s}$	$\Delta\nu_{z,+}$	$\Delta\nu_z$	$\frac{d\nu_z}{dT_\pm}$
proton	206 mHz	74 mHz	0.04 mHz	85 Hz/K
Be^+	3.2 Hz	9 mHz	0.04 mHz	9.5 Hz/K

Table 3.2: Approximate frequency shifts of the ions in the AT due to changes in the radial energy or spin state are given. Note that for Be^+, $\Delta\omega_{z,s}$ refers to a spin transition of the valence electron. Spin transitions have a corresponding shift that can be easily resolved compared to typical axial frequency stabilities due to fluctuations of the trapping potential, but are equivalent to less than three cyclotron transitions.

The rate at which cyclotron transitions occur is given by Fermi's golden rule [39],

$$\frac{\delta n_+}{\delta t} = \frac{2\pi}{\hbar}\Delta_+\rho\left(E_+\right)\Gamma^2_{i\to f}, \tag{3.58}$$

where $\rho\left(E_+\right)$ is the density of states of a one dimensional harmonic oscillator, and $2\pi\Delta_+ = qB_2\left\langle z^2\right\rangle/m$ is the coupling strength of the cyclotron mode to the axial mode. Cyclotron transitions are driven by electric field noise with spectral noise density E_0. These transitions are dipole allowed with strength given by the transition matrix element [39],

$$\Gamma^2_{i\to f} = qE_0\sqrt{\frac{\hbar}{m\omega_+}\frac{n_+}{2}}. \tag{3.59}$$

It becomes apparent that from Eq. (3.58) and Eq. (3.59) that

$$\frac{dn_+}{dt} \propto n_+, \tag{3.60}$$

and minimizing E_+ minimizes unwanted cyclotron quantum jumps. E_0 is determined experimentally, and previous experiments [39] have found $E_0 = 0.35\,\mathrm{meVs}^{-1}$ in a nearly identical AT.

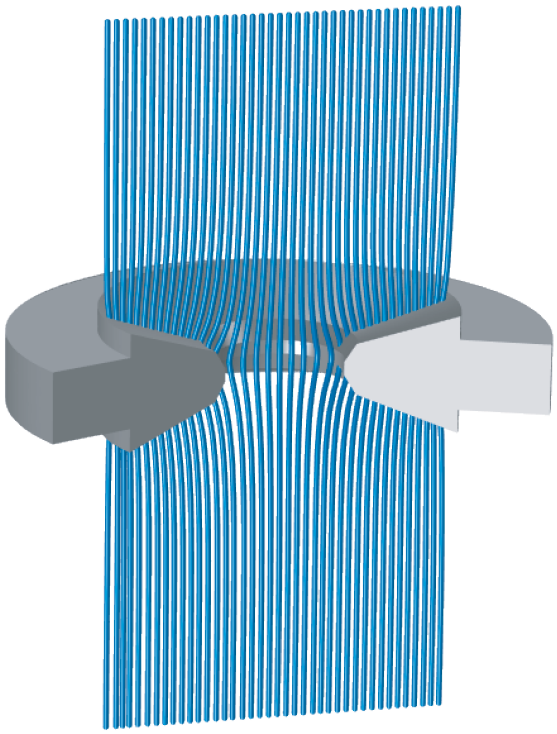

Figure 3.6: The magnetic field in the AT is illustrated. A ferromagnetic ring electrode introduces a strong B_2 term and allows spin state detection via the continuous Stern-Gerlach effect. Adapted from [30].

3.3 Cooling Schemes

3.3.1 Resistive Cooling

Given the parameters in Table 3.2 and the scaling in Eq. (3.59), single spin flips can only be resolved with cyclotron energies on the order of $100\,\mathrm{mK}/k_B$, much lower than the temperature of the apparatus. Until now, all particles have been prepared by coupling to an additional RLC circuit resonant with the cyclotron mode. Once coupled to this circuit, and then decoupled, the cyclotron energy is fixed, but non-deterministically samples the Boltzmann distribution of the circuit near 4 K - illustrated in Figure 3.7. The cyclotron mode is then re-prepared each time the particle is found to have an energy higher than the "cut", or a certain maximum energy. However, this technique is extremely time consuming. On one hand, only a small fraction of preparation attempts are successful, and on the other RLC circuits near the cyclotron frequency are much more difficult to build at high Q - resulting in very long coupling times.

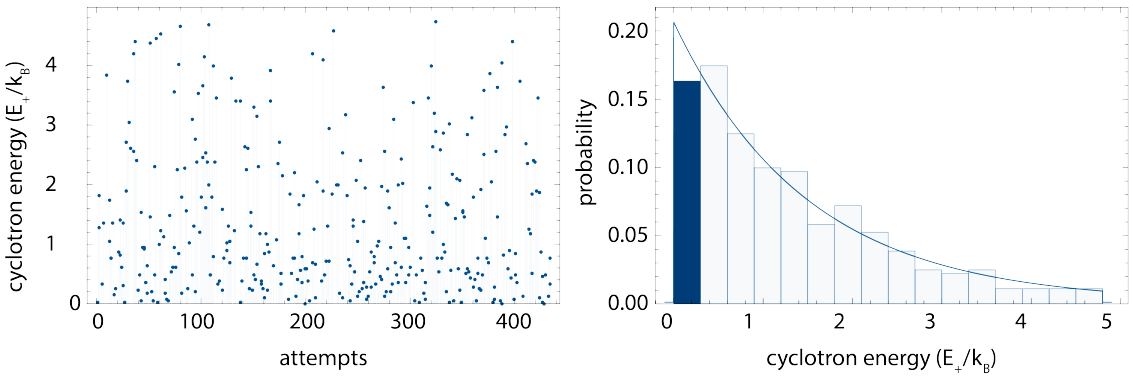

Figure 3.7: Selective resistive cooling is illustrated. On the left is an example of repeated measurements of the cyclotron energy of the proton after coupling to a detector near 4 K is shown. On the right is a histogram of these attempts and during a measurement campaign only particles found to be in the highlighted bin would be used, otherwise the procedure would need to be repeated. Figure adapted from [30].

3.3.2 Feedback Cooling and Heating

Electronic feedback can be used to change the effective temperature of the detection circuit, increasing and decreasing the effective temperature with negative and positive feedback, respectively. First described in the very early Penning-trap days [35] [5], feedback is now used in nearly every Penning-trap experiment with image current detection e.g. [40, 41]. Shown in Fig. 3.8b, a fraction of the resonator and particle signal is picked off before FFT analysis and phase shifted by $\phi = 180°$ (alternatively, with no phase shift for heating). Selective attenuation enables tuning of the effective temperature and the signal is then sent back to the resonator in the apparatus via weak ($< 0.1\,\mathrm{pF}$) capacitive coupling[6]. The following relations then determine the temperature,

$$\frac{T_0}{T_{\mathrm{FB}}} = \frac{Q_0}{Q_{\mathrm{FB}}} = \frac{\gamma_0}{\gamma_{\mathrm{FB}}}. \tag{3.61}$$

T, Q, and γ are the temperature of the system, the Q-value of the detection system, and the dip width of the particle, where the subscripts 0 and FB correspond to the unperturbed system and the system with feedback applied. Ultimately, the minimum temperature is limited by the noise of the amplifier. During the course of this work feedback cooling proved extremely useful in setting up the AT and determining the temperature of the axial detection system in the precision trap or PT.

[5] It is extremely underappreciated how good Dehmelt was at naming things, the "monoelectron oscillator" certainly adds to the canon.

[6] A "weak capacitive coupling" is nothing more than a coax cable, with shielding stripped at one end, tied to another wire.

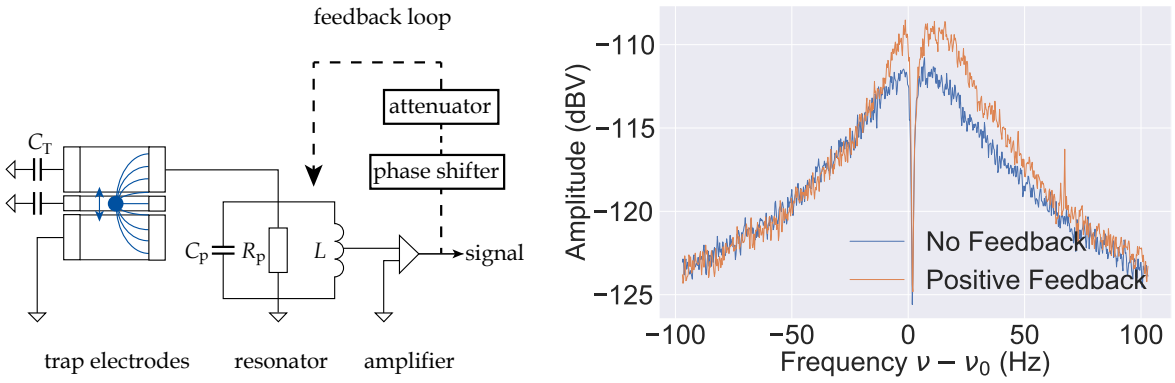

(a) (b)

Figure 3.8: **(a)** Feedback can be applied to the particle and resonator which changes the effective temperature of the system. **(b)** When feedback is applied $Q_0 \to Q_{\mathrm{FB}}$ and $\gamma_0 \to \gamma_{\mathrm{FB}}$. Using Eq. (3.61), the effective temperature of the resonator with feedback can be extracted.

3.3.3 Laser Cooling

Of course, a natural progression is to prepare particles with laser cooling. As is common in many other experiments, particles are routinely prepared with energies around or below the mK level even with simple Doppler cooling [42, 43]. However, laser cooling requires an optical or near optical transition to scatter photons, which particles like the proton obviously do not have. As a result, in order to benefit from laser cooling, such particles can only be sympathetically cooled, a technique common in many experiments [44, 45, 46] but unexplored with exotic species such as protons and antiprotons. In fact laser cooling has been used only sparingly Penning traps e.g. in [47, 48]. Sympathetic cooling uses an auxiliary species with an accessible transition, in our case Be^+, to couple to the inaccessible species, with the cooling rate of the particle of interest given by the coupling time to the cold particle. An example of the benefits of such an approach are shown in Figure 3.9, illustrating that with laser cooling spin states can be reliably prepared and read out with much improved accuracy and time cost.

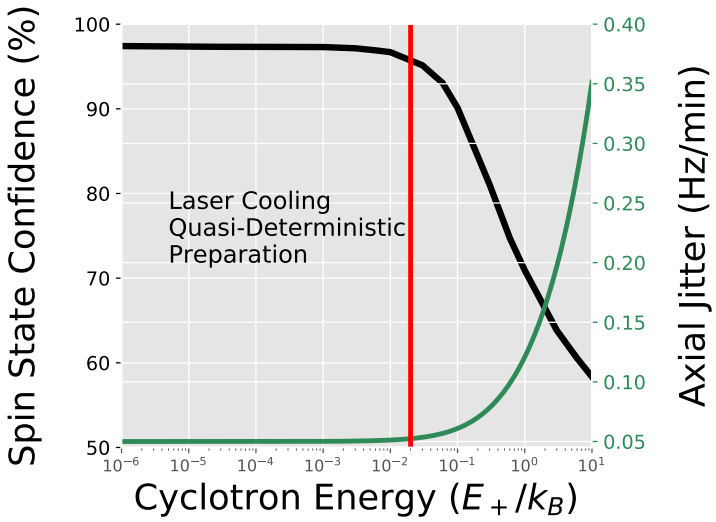

Figure 3.9: The line in green shows the axial jitter as a function of cyclotron energy. The axial frequency jitter needed to resolve spin flips, similarly determines the spin state confidence, given in black, which approaches 100% near 100 mK at which point the uncertainty is given by fluctuations in the axial frequency due to voltage supply noise. Preparing protons with laser cooling methods turns the statistical process of selective resistive cooling into a quasi-deterministic one.

3.4 Common Endcap Coupling

Traditionally, sympathetic cooling in ion traps has been performed by co-trapping the two ion species, for example along the axis of a linear Paul trap as in [44, 45, 46]. A relatively niche, alternative approach is to trap the two species in separate potentials and rely on the Coulomb interaction to couple the particles, for example as demonstrated in [49]. More exotically though, a scheme was proposed roughly three decades ago in which two ion traps share a common electrode which mediates the energy exchange via image currents [5]. Under such a scheme, the framework of Section 2.1.3 still holds and the two ion-trap systems can be thought of as two connected LC circuits, illustrated in Fig. 3.10.

Following [5] and [50] Hamiltonian of this system describes an oscillatory exchange of energy with eigenfrequencies,

$$\omega_{\pm}^2 = \frac{1}{2}[(\omega_1')^2 + (\omega_2')^2] \pm \frac{1}{2}\sqrt{[(\omega_1')^2 + (\omega_2')^2]^2 + 4g^4}. \tag{3.62}$$

Here the coupling constant is given by $g^2 = (L_1 L_2 C_T^2)^{-1/2}$, and ω_i' is the reduced

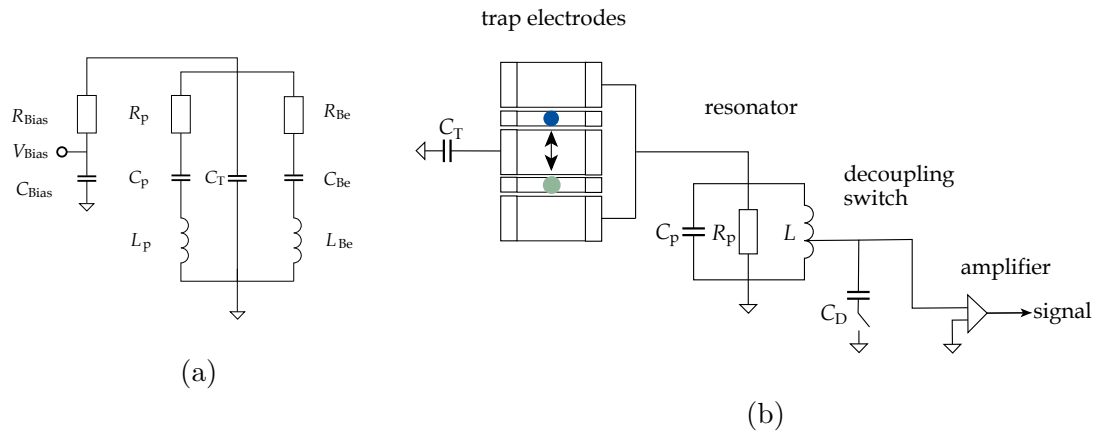

Figure 3.10: Illustration of common endcap coupling. In (a) the circuit representation is shown, where two traps are independently biased and coupled via a common electrode with capacitance C_T to ground. Mathematically this is equivalent to two coupled RLC circuits connect by a capacitor. (b) shows schematically how the system is built, the common electrodes are connected to a resonator to read out the axial frequencies and a hypothetical decoupling switch ensures that the detector does not limit the temperature.

resonance frequency

$$\omega_i^{'} = \left(L_i C_i^{'}\right)^{-1/2} \tag{3.63}$$

with

$$C_i^{'} = \frac{C_i C_T}{C_i + C_T}.^{7} \tag{3.64}$$

For the coupling to be resonant, the particles will have the same axial frequency and the following assumption holds,

$$\bar{\omega} = \frac{1}{2}[(\omega_+) + (\omega_-)] \approx (\omega_1^{'}) \approx (\omega_2^{'}), \tag{3.65}$$

where $\bar{\omega}$ is the shared axial frequency. Energy is exchanged between the two ion trap systems with a characteristic exchange time,

$$\tau = \bar{\omega_z}\pi \frac{D_1 D_2}{\sqrt{N_1 N_2} C_T \frac{\sqrt{m_1 m 2}}{q_1 q_2}}. \tag{3.66}$$

In fact, this exchange time is a general consequence of coupling two oscillators, and the relation

[7]Note that $\omega_\pm$, here does not refer to the radial trap modes, and is used only to keep consistent with the notation in the literature. In the following chapters $\omega_\pm$ refers exclusively to the radial frequencies.

$$\tau = \alpha\omega \frac{\sqrt{m_1 m_2}}{|q_1 q_2|}, \tag{3.67}$$

holds, where α is a proportionality constant that determines the strength of the interaction based on the medium of exchange.

However, as suggested by the switch in Fig. 3.10, the resonator, which is necessary to determine the axial frequency, creates an additional problem. The system shown in Fig. 3.10 is assumed to be in thermal equilibrium and, following [32] and [50], satisfies the following system of equations:

$$\begin{aligned} 0 &= -k_B \left(\frac{1}{\tau_{\text{D-p}}} + \frac{1}{\tau_{\text{Be-p}}} + \frac{1}{\tau_{bias}} \right) T_p + \frac{k_B}{\tau_{\text{D-p}}} T_D + \frac{k_B}{\tau_{\text{Be-p}}} T_{Be} + \frac{k_B}{\tau_{bias}} T_{bias} \\ 0 &= -k_B \left(\frac{1}{\tau_{Be-p}} + \frac{1}{\tau_{D-Be}} + \frac{1}{\tau_L} + \frac{1}{\tau_{bias}} \right) + \frac{k_B}{\tau_{D-Be}} T_D + \frac{k_B}{\tau_{\text{Be-p}}} T_p + \frac{k_B}{\tau_L} T_{Be} + \frac{k_B}{\tau_{bias}} T_{bias}. \end{aligned} \tag{3.68}$$

The temperature of each element in the system, i.e. T_p, T_{Be}, is determined by its coupling, τ_i to the "thermal baths" of the laser and detection system at temperatures $T_L \approx T_{\text{Doppler}} \approx 0.5\,\text{mK}$ and $T_D \approx 4\,\text{K}$, respectively.

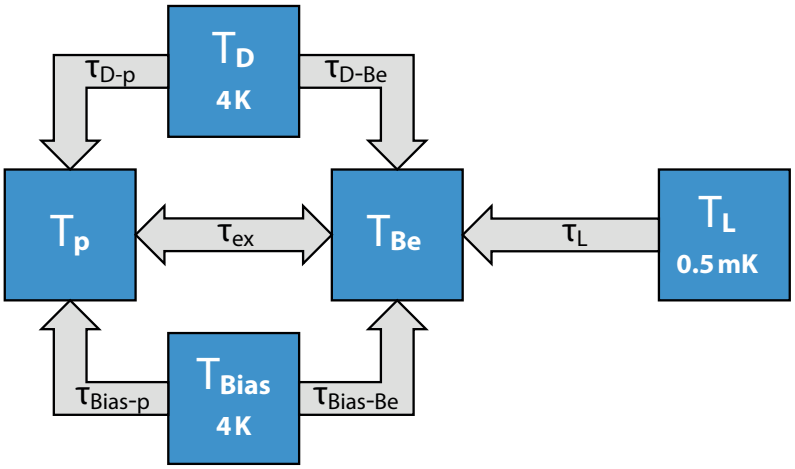

Figure 3.11: Illustration of the coupling of the proton to the detector, biasing network, and beryllium ions in a common endcap cooling scheme. The laser is coupled exclusively to the beryllium ions, which are also coupled to the detector, and in order for the cooling to be effective, we require $\tau_D \ll \tau_{ex}$. Figure adapted from [50].

As shown in Fig. 3.11, the temperature of the proton is essentially a competition between the detector coupling with time constant $\tau_{D-p} \sim 1\,\text{s}$ and the exchange coupling with time constant $\tau_{ex} \sim 1\,\text{min}$. Initially, the experiment described here

relied on a switch mechanism as illustrated in Fig. 3.10 (b), in which a switchable capacitance lowers the resonator frequency while keeping the trapping potentials unchanged. However, as implemented in this work, technical problems prevented its use. An improved version of this switchable capacitance is is currently under development[8] and will be used in the next version of the apparatus. The highlights of this work though are the results presented in Chapter 9, which use a modified version of the common endcap coupling technique. In this technique, the resonator is used to compensate the trap inductances and significantly larger coupling rates are obtained. See Chapter 9 for more details, including a detailed discussion of the model presented in Eq. (3.66) and Fig. 3.11.

[8] in the context of the Ph.D. work of Markus Wiesinger, also at MPIK

Chapter 4

Proton g-Factor Measurement

Although a limited part of my thesis work, this chapter summarizes the proton g-factor measurement that was completed in 2017 (the culmination of a large amount of previous work mainly, by Georg Schneider and Andreas Mooser). This chapter also provides some context for the sum of the work shown here. The heart of the Mainz proton experiment is the g-factor measurement and the techniques developed were in service of that goal.

4.1 Double-Trap Technique

As described earlier, a magnetic bottle is necessary to resolve spin-flips but has the unwanted side effect of shifting the Larmor frequency, as in Eq. (3.54), by,

$$\frac{\Delta\omega_L}{\omega_L} = \frac{1}{m\omega_z}\frac{B_2}{B_0}\left(-E_+\left(\frac{\omega_z}{\omega_+}\right)^2 + E_z + E_z\right). \tag{4.1}$$

This shift not only needs to be constrained as a systematic error, but also broadens the g-factor resonance due to frequency fluctuations (see Section 2.2.2). First developed by the highly charged ion group in Mainz in the 1990s, the double-trap technique solves this problem by separating g-factor measurements into two, spatially separated components. First, in the precision trap (PT) the trap frequencies ω_+, ω_z, ω_- are measured while a spin-flip drive near the Larmor frequency ω_L is applied. Then, in a second trap, the analysis trap (AT), the spin state is resolved to determine whether or not a spin flip occurred.

The apparatus used in the measurement, along with the experimental sequence, is shown in Fig. 4.1. Unlike the next generation experiment, cold protons were prepared in the PT using a dedicated cyclotron image current detector. The measurement cycle was as follows:

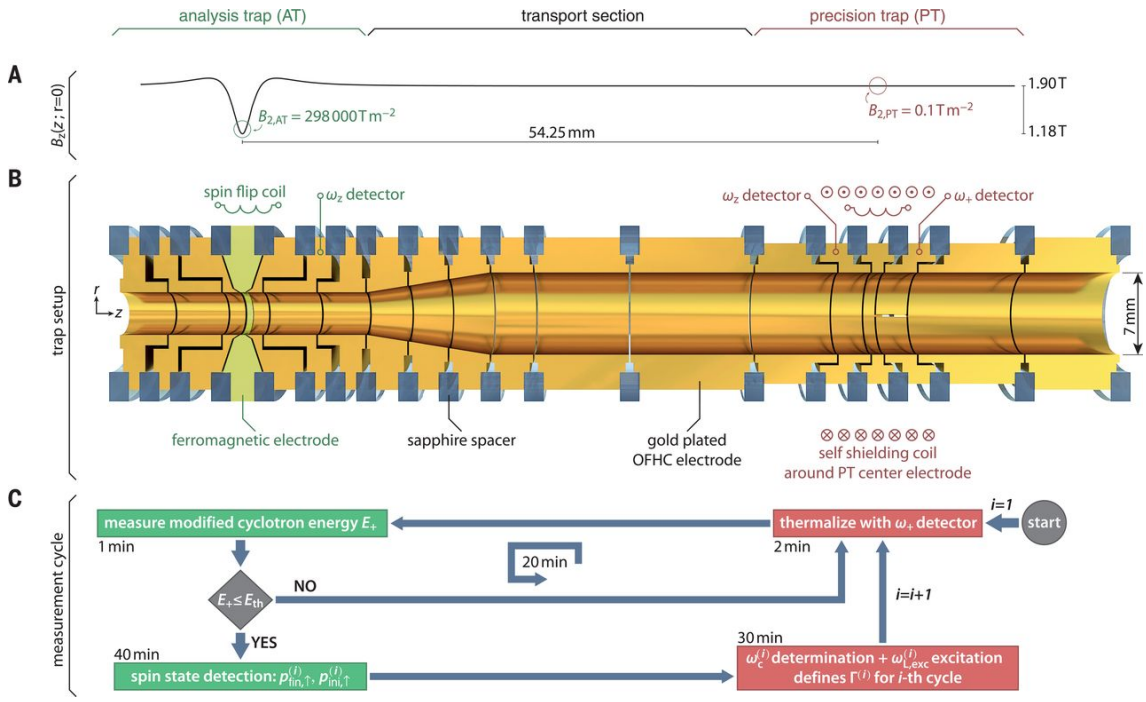

Figure 4.1: The apparatus and experimental sequence used in the 2017 proton g-factor measurement is shown. The PT is used for particle preparation and measurement of the trap and Larmor frequencies while the AT is used for spin state analysis. Image from [2, 30]. See text for more details.

1. The proton is coupled to the cyclotron detector and transported to the AT where the temperature is measured.

2. If the cyclotron mode is insufficiently cold, $E_+/k_\mathrm{B} > 600\,\mathrm{mK}$, the proton is transported back to the PT and then coupled to the cyclotron resonator again in Step 1.

3. When the cyclotron mode is sufficiently cold, $E_+/k_\mathrm{B} < 600\,\mathrm{mK}$, the spin state is initialized by driving a spin transition. This step also determines the final spin state of the previous cycle.

4. The proton is transported back to the PT where the trap frequencies are measured. A spin flip drive at the Larmor frequency, ν_L, is applied during the sideband measurement of the cyclotron frequency.

5. The cycle starts again at Step 1, until, after moving onto Step 3, the resulting spin state can be resolved.

Each of these measurement points is denoted Γ_i, a tuple with value,

$$\Gamma_i = \left\langle p_i \middle| \frac{\nu_{L,i}}{\nu_{c,i}} \right\rangle, \tag{4.2}$$

where p_i is the probability that a spin transition occurred at the drive frequency $\nu_{L,i}$ with instantaneous free cyclotron frequency $\nu_{c,i}$. Note that it is during the sideband measurement in Step 4 that the cyclotron mode is heated and it becomes necessary to re-prepare a cold particle. When the cyclotron mode is coupled to the axial mode, and thus the axial detector, it comes away with an energy $E_+ = \nu_+/\nu_z\, E_z$, where E_z is Boltzmann distributed around the resonator temperature.

4.2 Spin State Analysis

Of course, neglected until now is the determination of the spin state. There are two main analysis methods, both relying on axial frequency measurements in a strong magnetic bottle. First, the straightforward but rather primitive threshold method compares the axial frequency jitter, $\Delta\nu_z = \nu_{z,i} - \nu_{z,i-1}$, to a threshold frequency, denoted $\Delta\nu_{th}$. This threshold frequency is set near the level given by Eq. (6.12) and a spin flip is defined to have occurred when $|\Delta\nu_z| \geq \Delta\nu_{th}$. On the other hand, the Bayesian method, weights the probability of a spin transition due to a change in axial frequency $\Delta\nu_z$ by the previous frequency measurements. As a result, the complete axial frequency dataset is used and a continuous spin flip probability is assigned to each Γ_i, in contrast to a binary "0" or "1". Ultimately, while the threshold method is useful when the confidence of assigning a spin state is close to unity, the Bayesian method allows more advanced statistical methods to be used in the final g-factor analysis. What follows is a brief summary of the spin flip analysis conducted in the last measurement campaign, following the approach of Refs. [3, 30, 39].

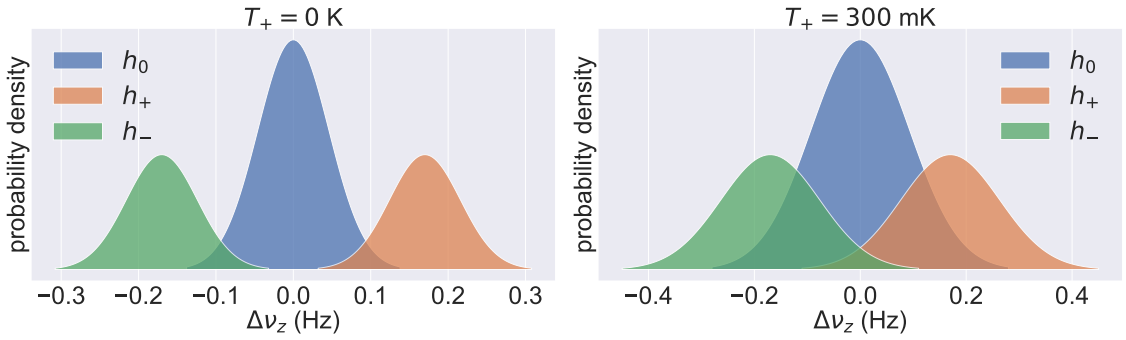

(a) (b)

Figure 4.2: **(a)** The distribution of axial frequency shifts in the AT after attempting to drive a spin transition in the PT is shown at $T_+ = 0$. **(b)** When T_+ is not zero, shown here is $T_+ = 300\,\text{mK}$, the distributions of the axial shifts are broadened. These distributions h_0, h_-, and h_+ denote the axial frequency shifts due to no spin transition, spin up, and spin down transitions, respectively.

First, the initial spin state is determined in the AT by continually measuring the axial frequency while applying a spin flip drive. The sequence of axial

frequency measurements is denoted S_1 and stops when an axial frequency jump $\Delta\nu_z = \nu_{z1,n} - \nu_{z1,n-1} \geq \Delta\nu_{th}$ is observed, with the sign of $\Delta\nu_z$ determining the spin state $|\downarrow\uparrow\rangle_{1,n}$. After attempting to drive a spin transition in the PT, the proton is transported back to the AT where, again, a series of axial frequencies, S_2, are recorded in the presence of a spin flip drive. When a sufficiently large axial frequency shift, $\Delta\nu_z = \nu_{z2,n} - \nu_{z2,n-1} \geq \Delta\nu_{th}$ is observed, the sequence is stopped and the two series of axial frequencies can be written as,

$$S_1 = \{\nu_{z1,0}, \nu_{z1,1}, ...\nu_{z1,n}\} \tag{4.3}$$

$$S_2 = \{\nu_{z2,0}, \nu_{z2,1}, ...\nu_{z2,n}\}. \tag{4.4}$$

Four spin states can then be assigned,

$$|\downarrow\uparrow\rangle_{1,0}, |\downarrow\uparrow\rangle_{1,n} \tag{4.5}$$

$$|\downarrow\uparrow\rangle_{2,0}, |\downarrow\uparrow\rangle_{2,n} \tag{4.6}$$

measured at the beginning and end of series S_1 and S_2 respectively. Then the spin flip probability, p_i, of Eq. 4.2 can be written as,

$$p_i = P\left(|\downarrow\uparrow\rangle_{1,n} \neq |\downarrow\uparrow\rangle_{2,0}\right), \tag{4.7}$$

i.e. the probability that the spin state at the start of sequence S_2 is different than the one at the end of series S_1.

However while the spin state $|\downarrow\uparrow\rangle_{1,n}$ is trivially assigned by the threshold method with no loss of confidence, the same is not true for $|\downarrow\uparrow\rangle_{2,0}$. In other words, since $|\downarrow\uparrow\rangle_{1,n}$ comes at the end of an axial frequency series, only the final state matters and can be prepared with arbitrary fidelity (although with a potentially large number of spin transitions occurring in the meantime). The final spin state on the other hand, requires the spin state to be assigned immediately - we are not afforded the luxury of being able to wait until a high visibility spin transition associated with large $\Delta\nu_z$ is observed. Rather, it is necessary to work backwards from the well determined final spin state, $|\downarrow\uparrow\rangle_{2,n}$, using Bayes' Theorem, to assign a spin state probability to the start of the series.

As shown in Fig. 7.1, there are three distributions of axial frequency fluctuations $\Delta\nu_z$, during an AT spin measurement. Labeled h_0, h_+, and h_-, these correspond to no change in spin state from measurement $\nu_{z,i}$ to $\nu_{z,i+1}$ and an "up" or "down" transition during the same window, respectively. We then need to determine to which distribution the axial frequency measurements at the beginning of S_2 belong. h_0, h_+, and h_- are normal distributions with widths $\sigma(E_+)$, determined by the proton's axial frequency jitter - whether from radial energy or the stability of the voltage supplies. Meanwhile, the centers are given by

$$\mu(h_0) = 0 \tag{4.8}$$

$$\mu(h_-) = -\Delta\nu_{z,SF} \tag{4.9}$$

$$\mu(h_+) = +\Delta\nu_{z,SF}, \tag{4.10}$$

where $\Delta\nu_{z,SF}$ is the change in axial frequency due to a change in spin state - during this campaign around 170 mHz. Now, Bayes' theorem,

$$P(A|B) = \frac{P(B|A)P(A)}{P(B)} \tag{4.11}$$

states that the probability of A given B is equal to the probability of B given A normalized by their respective marginal probabilities. In the language of spin flips, the probability of a spin-flip having occurred given a certain series of axial frequency shifts, allows us to assign a probability to the initial spin state. Using this, we assign a spin state probability, $P_i^{\uparrow} = 1 - P_i^{\downarrow}$, given the change in axial frequency $\Delta\nu_{z,i}$, the radial energy E_+, and the previous knowledge of the spin state. Derived in [30, 39], the spin state probability is assigned iteratively throughout a series S by

$$P_i^{\uparrow} = \frac{(1-p_{\mathrm{SF}})\,h_0\,(E_+)\,P_{i-1}^{\uparrow} + h_+\,(E_+)\,p_{\mathrm{SF}}\left(1-P_{i-1}^{\uparrow}\right)}{(1-p_{\mathrm{SF}})\,h_0\,(E_+) + P_{i-1}^{\uparrow}h_-\,(E_+)\,p_{\mathrm{SF}} + (1-p_{\mathrm{SF}})\,h_+\,(E_+)}, \tag{4.12}$$

where p_{SF} is the spin flip probability and the initial uncertainty is maximized by $P_0^{\uparrow} = P_0^{\downarrow} = 0.5$. Spin state analysis during the measurement campaign then uses all available tools to assign a spin state, the threshold method when the spin state can be assigned with high confidence, and the Bayesian method when a spin state probability must be assigned.

4.3 *g*-Factor Analysis

Finally, the now completed g-factor resonance data, $\{\Gamma_0, ..., \Gamma_n\}$, yields a "$g$-factor resonance" i.e. the spin-flip probability at a given Γ_i, see Eq. (4.2). This data is analyzed with a maximum likelihood parameter estimation using the likelihood function

$$\mathcal{L} = \prod_{i=0}^{n} \mathcal{L}_{1,i} \cdot p + \mathcal{L}_{2,i} \cdot (1-p)\,. \tag{4.13}$$

Here, p is the spin flip probability, $\mathcal{L}_{2,i} = 1 - \mathcal{L}_{1,i}$, and

$$\mathcal{L}_{1,i} = (1 - \chi\,(\Gamma_i, \mu, \sigma)) + \chi\,(\Gamma_i, \mu, \sigma)\,, \tag{4.14}$$

with the lineshape of the Larmor resonance given by $\chi(\Gamma, \mu, \sigma)$ [51, 2].

The final resonance is shown in Fig. 4.3 with the final result of,

$$\frac{g_p}{2} = 2.792\,847\,344\,62(75)(34) \tag{4.15}$$

where the first error is the 1-σ statistical error and the second error is the systematic uncertainty [2]. Together with an improved measurement of the antiproton g-factor [3], $\mu_p \neq \mu_{\bar{p}}$ is constrained to [52],

$$\frac{\delta\mu}{\mu_N} = \left(\frac{\mu_p}{\mu_N} + \frac{\mu_{\bar{p}}}{\mu_N}\right) = 0.3(8.3)10^{-9}, \tag{4.16}$$

where μ_N, is the nuclear magneton. These measurements set the most stringent constraints on CPT odd parameters in the baryon sector of the Standard Model Extension (SME) and the constraints are reproduced in Table 4.1, both with 95 % confidence intervals [52].

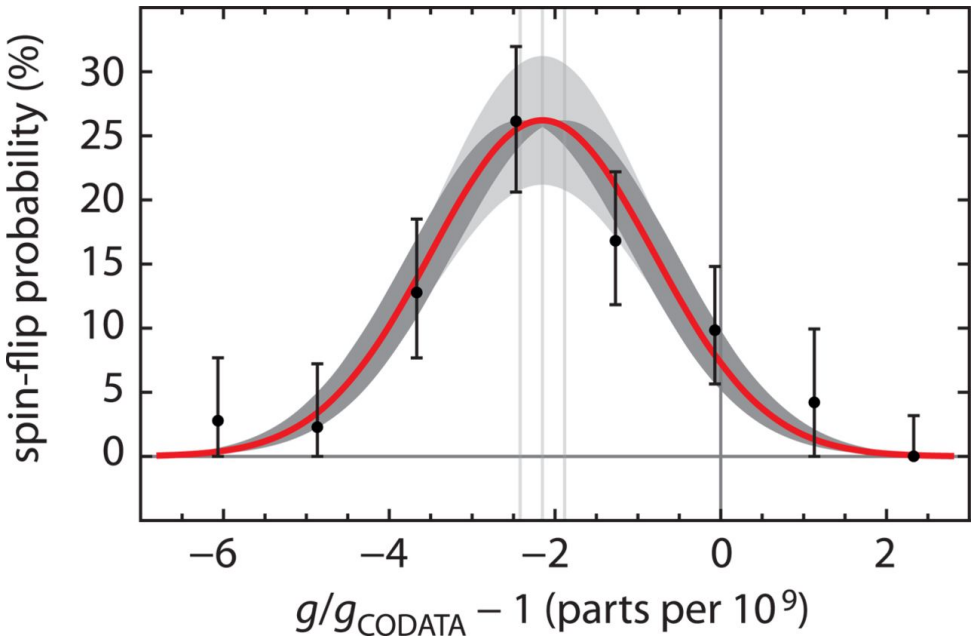

Figure 4.3: The final g-factor resonance of the 2017 measurement campaign shown in [2]. The red line comes from a maximum likelihood parameter estimation with errors on the resonance center given by the dark gray bands and errors on the spin flip amplitude given by the light gray bands. The binned data points are not used in the analysis but are shown for reference. g_{CODATA} is the previous CODATA value of $g_p = 5.585\,694\,702(17)$ [53]. Figure from [2].

$\left\lvert\tilde{b}_p^Z\right\rvert$	$< 8.1 \times 10^{-25}\,\mathrm{GeV}$
$\left\lvert\tilde{b}_{F,p}^{XX} + \tilde{b}_{F,p}^{YY}\right\rvert$	$< 4.6 \times 10^{-9}\,\mathrm{GeV}^{-1}$
$\left\lvert\tilde{b}_{F,p}^{ZZ}\right\rvert$	$< 3.3 \times 10^{-9}\,\mathrm{GeV}^{-1}$
$\left\lvert\tilde{b}_p^{*Z}\right\rvert$	$< 1.5 \times 10^{-24}\,\mathrm{GeV}$
$\left\lvert\tilde{b}_{F,p}^{*XX} + \tilde{b}_{F,p}^{*YY}\right\rvert$	$< 3.1 \times 10^{-9}\,\mathrm{GeV}^{-1}$
$\left\lvert\tilde{b}_{F,p}^{*ZZ}\right\rvert$	$< 1.1 \times 10^{-8}\,\mathrm{GeV}^{-1}$

Table 4.1: SME Constraints
CPT odd coefficients in the Standard Model Extension can be constrained with the improved limits on $\frac{\delta\mu}{\mu_N}$. See [52] for details.

4.4 Uncertainty Evaluation and Outlook

The systematic uncertainty budget is summarized in Table 4.2 and described briefly below, see [2, 30] for more details.

	Relative shift on $g_p/2$ (ppt)	Error (ppt)
Trapping Potential*	0	9
Magnetic inhomogeneity*	8	4
Relativistic Shift*	-44	26
Image current	1	1
Image charge	-98	3
Fitting	0	80
Total Systematic Uncertainty	**-133**	**123**
Total Statistical Uncertainty*		**269**

Table 4.2: The uncertainty budget of the most precise measurement of the g-factor of the proton, adapted from [2]. Shifts marked * are due to nonzero radial energies and benefit from enhanced cooling techniques.

Trapping Potential* A nonzero C_4 shifts ω_+, proportional to ΔTR and the mode temperatures, see Eq. (3.22).

Magnetic inhomogeneity* A nonzero B_2 shifts ω_+, ω_L, proportional to the mode temperatures, see Eq. (3.54).

Relativistic Shift* ω_+, ω_L are proportional to E_+. This can be thought of as a consequence of the (larger) relativistic mass of the proton with finite energy [24].

Image Charge and Image Current Image charges induced on trap electrodes are an additional force on the trapped proton and shift ω_+, ω_-. For a detailed analysis of this systematic effect see [54].

Fitting Determination of ν_z is limited by both the error in fitting the axial dip and changes to the dip lineshape due to small changes in the axial resonator spectrum.

Notably, as seen in Eq. (4.15) and Table 4.2, the precision to which g_p (along with $g_{\bar{p}}$ [3]) can be determined is still limited by statistics, largely because of the long duration of the measurement sequence described here. In addition, many of the major systematic effects, marked with * above, are the result of high particle energies. In fact, for some experiments, these are even more dominant and limit further precision, e.g. [28, 55, 56]. As a result, the rest of this thesis describes a new apparatus, new techniques, and new results that will enable increased precision in future measurements of the proton g-factor and other precision measurements.

Chapter 5

Design of the New Experiment

A new experimental apparatus was required o implement sympathetic cooling of protons. In particular, we redesigned the system of Penning traps shown in Fig. 4.1 to include optical access for both the cooling laser and an ablation laser which ultimately replaced the electron gun as our ion source. An overview is illustrated in Fig. 5.1 where, in addition, the double-trap design of previous generations, consisting of the precision trap (PT) and the analysis trap (AT), was expanded to a five-trap design. What follows is a description of these new elements and a more detailed look into the experimental apparatus.

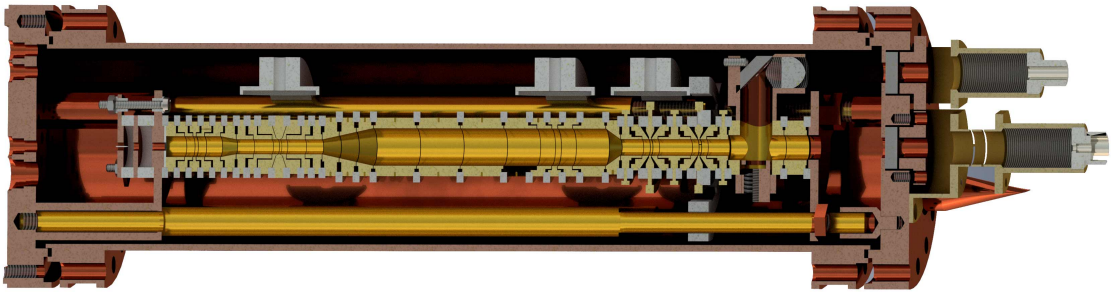

Figure 5.1: A new apparatus, replacing the one used during the latest g-factor measurements, consists of five Penning traps and includes optical access for lasers, as well as additional traps to implement p-Be^+ image current coupling.

5.1 Overview

To begin, I present an overview of the experimental concept and an overview of each of the traps used in the five-trap configuration.

Precision Trap (PT)

The precision trap (PT) is a large, homogeneous trap that retains the function of the previous generation. During a g-factor measurement, the PT is used to measure the trap frequencies and the Larmor frequency. This apparatus however, features a new design with trap radius $r = 4.5\,\mathrm{mm}$, compared to the previous value of $r = 3.5\,\mathrm{mm}$. The larger trap increases the trap volume with largest harmonicity, enabling phase sensitive detection methods [36, 57] that proved difficult in the previous version of the experiment [30].

Analysis Trap (AT)

The previous analysis trap (AT) is retained from the earlier experiment and is used to analyze the spin state of the proton. However, because the axial detection system was changed, the AT needed to be completely re-characterized, with results shown in Chapter 5.

Coupling Trap (CT/BT)

The coupling traps, consisting of a coupling trap (CT) and a nearly identical beryllium trap (BT), have been designed to implement the common endcap coupling described in Section 1.4. A single proton is stored in the CT and coupled to a large cloud of beryllium ions in the BT. The motivation for the design of these traps is described in the following section.

Storage Trap (ST)

The storage trap (ST) was designed as a production region for protons, located near the electron gun, but separating the sensitive AT electrodes from the electron beam. Over the course of my thesis work the ST was moved in between the ablation ion source and the coupling traps to act as a buffer region (see the following chapter) and protons were produced with the ablation laser. The ST has a trap radius of $r = 2.5\,\mathrm{mm}$, chosen as a compromise between homogeneity and image current signal strength. The dip width γ is proportional to the effective electrode distance D_{eff} and scales with the trap radius. Ultimately the ST and the PT were the two traps used to demonstrate sympathetic cooling - described in Chapter 9.

5.2 Trap Design and Coupling Traps

The coupling traps, the CT and the BT, feature a novel design, tailored to the sympathetic cooling experiment described in Section 2.4 and Eq. (3.66). Even a cursory inspection of this equation is instructive to guide trap design. For example, $m_1 = m_p$ and $N_1 = 1$ are clearly fixed. Meanwhile, the choice of beryllium as cooling ion gives $m_2 = m_{Be} \approx 9\,\mathrm{u}$[1]. The constraints, as $\bar{\omega}_z$ is set by the detector design and N_2 can vary, are C_T and D_1, D_2 where, to have a symmetric set of traps we chose $D_1 = D_2$. As a result, the coupling traps are designed to be as small as possible with the size of the AT used as a reference design. The capacitance of the traps to ground, C_T is also minimized through a careful selection of the geometry of the electrodes. The final design is shown in Fig. 5.2 where the angled correction electrodes and inset endcap electrodes have been designed to maximize the spacing between the conductive and isolating materials[2]. In addition, while the traps are usually kept electrically isolated with sapphire spacers, the ring electrodes of the CT and BT are held in place with quartz rings - featuring roughly a factor of two lower in relative permittivity. The common endcap that enables the coupling, is, in this design, split into two symmetric parts which are then capacitively connected. This design retains the ability to apply independent biasing voltages and reduces the electrodes' length-to-diameter ratio, lowering heating rates during transport. Table 5.1 provides an overview of the final design parameters for the coupling traps, reproduced from [30].

Finally, the BT has a unique feature where the ring electrode is split into six segments for fluorescence detection (see Section 5.4.2 and Chapter 7) and to apply a rotating wall, as in [58]. Because the magnetron motion has negative energy, naive Doppler cooling results in increasing magnetron radius [43]. The rotating wall then, is a hexapolar drive that provides a confining radial force that keeps the laser cooled ions at a constant radius[3].

[1] Although not my work, the choice of ion for these experiments is interesting. Be^+ is the lightest easily laser cooled ion, but the wavelength of the cooling transition is inconvenient and can introduce unwanted charges onto cryogenic surfaces. Nevertheless, due to the much lower charge-to-mass ratio of, e.g., Ca^+,' it's difficult to image current detection and coupling working well at all with other commonly used species.

[2] We also investigated a design of the endcap electrodes with holes in the region touching the sapphire ring. Sadly this is yet to be tested.

[3] In practice this drive was only used a few times and with limited success. In experiments with purely optical detection, the rotating wall can be a very useful tool, but in our case the benefits are minimal. The magnetron sideband drive described in Section 2.1.5 seems to be much more suited to this experiment.

	C (pF)	r (mm)	D_{ce} (mm)	D_{ec} (mm)	D_{both} (mm)
CT/BT	10	2.0	4.2	4.6	2.9

Table 5.1: Final parameters for the coupling traps, shown in Fig. 5.2. C is the estimated trap capacitance of a single trap with $C_T = 2C$ while D_{ce}, D_{ec}, and D_{both} are the effective electrode distances when connected to the correction electrode, endcap, or both, respectively.

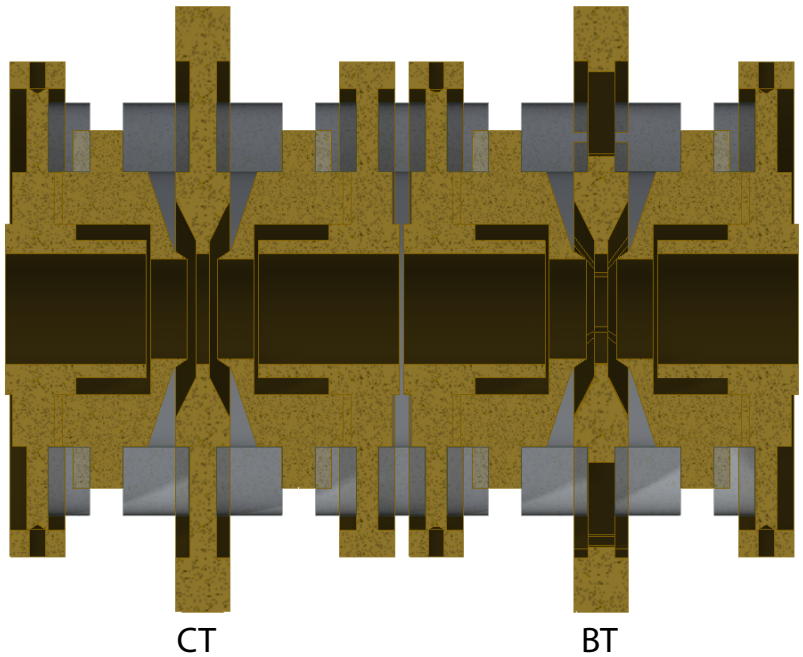

Figure 5.2: The coupling traps, the CT and the BT, are shown. As described in the text the traps employ a symmetric design and have been optimized to minimize the coupling constant, τ - see Eq. (3.66).

5.3 Trap Chamber and Assembly

Taking a very roughly "outward" approach, this section details the construction of the experiment, beginning with the electrodes themselves.

Trap electrodes are machined from oxygen-free high thermal conductivity (OFHC) copper to a tolerance of a few micrometers[4] and then gold plated with galvanic deposition of an 8 µm silver base layer and a 7 µm gold layer[5]. Afterwards, we polish the inner cylindrical surfaces and separate each electrode with polished sapphire rings, shown in Fig. 5.3. A "trap stack" is then formed, consisting of a series of gold plated electrodes that make up the precision Penning traps and the transport sections. These electrodes are pressed together and suspended by threaded brass rods inside a larger 5 cm diameter "trap can". This provides a unique advantage as, once pumped to high vacuum (HV) through a pinch-off tube, the trap can is hermetically sealed at low pressure. The trap can is then connected to a liquid helium bath cryostat at around 4 K and placed in the bore of a superconducting magnet, also at high vacuum. When brought down to cryogenic temperatures, all residual gas is frozen out (including hydrogen as there is sufficient surface area to allow residual hydrogen gas to form a single monolayer). Each electrode is then connected to alumina (or if a low loss tangent is required, as with the resonators, sapphire) vacuum feedthrough at the end of the trap chamber. These feedthroughs are soldered at high temperature to one end of the trap can which is referred to as the "pinbase". Ultimately, these connections lead to a high-precision voltage source which in this work is a UM-1-14 from Stahl Electronics. These feature precision channels that supply DC voltages to the ring and correction electrodes - stable to around $\delta V/V \cdot 1/\delta t \sim 10^{-6}\,\mathrm{h}^{-1}$. These voltages are filtered in several stages with standard surface-mounted device (SMD) RC filters, in a 4 K stage, a 77 K stage, and finally at room temperature. Excitation lines are also connected via feedthroughs to cryogenic coaxial cables and routed to external flanges on the vacuum chamber of the magnet.

As an aside, adding optical access to the new apparatus was a significant experimental challenge. First, through a collaboration with Kyocera's ceramic division, we designed a custom optical feedthrough that allows the cooling laser to pass through the trap chamber and hit an alignment silicon photomultiplier (SiPM) on the resonator housing, shown in Fig. 5.4. To withstand high temperatures during the soldering to the "pinbase" flange while remaining transparent and anti-reflective at 313 nm, we ultimately designed an angle cut sapphire feedthrough similar to our other electronic feedthroughs. On the other end of the trap chamber, the windows for the incoming lasers had similar constraints. In the end, we chose to use ⌀10 mm fused silica windows which are pressed onto an indium seal on the trap can flange.

[4] In this apparatus by the workshops at the University of Mainz and MPIK as well as Blum CNC - Technik GmbH

[5] Drollinger GmbH

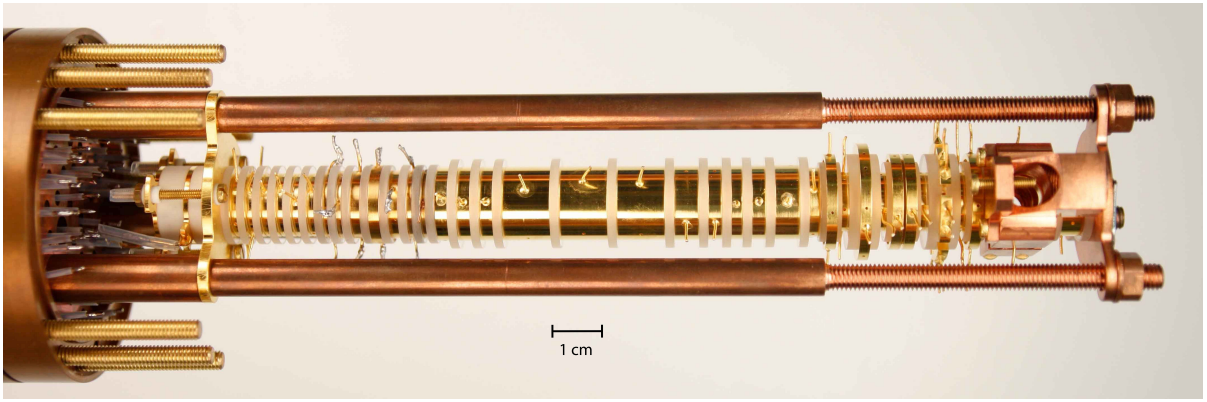

(a)

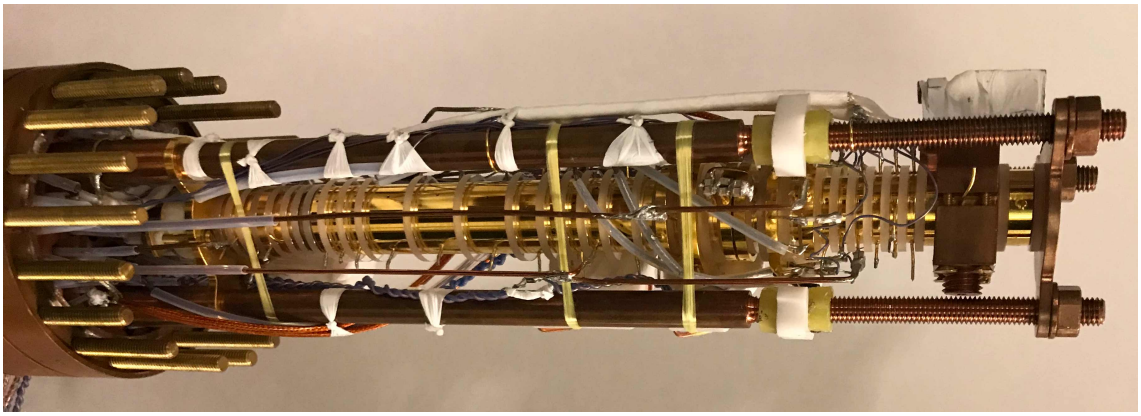

(b)

Figure 5.3: **(a)** An image of the assembled trap stack is shown along with **(b)** an image of the trap stack when wired with DC bias lines and excitation lines. Note that here the trap configuration is slightly different than shown above, as discussed in Chapter 6.

A flaw in this design, however, is that the force needed to compress the indium seal is sufficient to crack the windows if applied unevenly. An improved design would use a large scale version of the optical feedthrough described above that could be soldered onto the flange.

Finally, the two flanges are indium sealed and the trap chamber is baked out and pumped for several days until the background gas pressure is below 10^{-7} mbar at which point the trap chamber is sealed with the pinch-off tube.

5.4 Axial Detection Systems

Due to space constraints and the need for an additional resonator, the axial detection system required a complete redesign while retaining the same high Q res-

Connected Traps	ν_0 (Hz)	Q (cryocooler)	Q (magnet)	C (pF)	L (mH)
ST, PT	754 000	12 600	12 600	5.2	1.2
AT	552 000	32 500	29 000	8.7	1.5
CT, BT	502 000	3900	3400	7.8	3.0

Table 5.2: Resonator parameters in the new apparatus, where ν_0 is the center frequency and C, L are the effective capacitance and inductance respectively. Note that these values are intended only as a guide and a reference. During the course of the different measurement campaigns in this thesis the resonance frequencies and Q-values changed and different resonators were connected to different traps. Importantly, during the measurements of Chapter 9, the PT and the ST were connected to the resonator with highest Q and lowest frequency. The Appendix lists the values used in this measurement.

onators. These resonators, well described in [41, 59], consist of a toroidal PTFE core around which a few thousand windings of superconducting NbTi wire is wrapped. The resonators have a "hot" end connected to the trap, a "cold" end connected to ground, and an inductive tap connected to a cryogenic amplifier. A schematic of the amplifiers is shown in Fig. 5.5, with the basic design described in [30, 26, 60]. Importantly, the signal-to-noise ratio of the axial dip depends on the Q-value of this circuit, and care is taken at each step to minimize dielectric and other losses. For the coils, PTFE, with low loss tangent, is exclusively used as an insulating material while the toroidal geometry reduces losses induced by the magnetic field. Similarly, the amplifiers use PTFE laminate milled circuit boards, low loss SMD components, and GaAs field effect transistors (FETs) that remain operational at liquid helium temperatures. Shown in Fig. 5.4, the final axial detection system consists of three individual resonators placed in an oxygen-free high conductivity (OFHC) copper housing that thermalizes both the resonators and their amplifiers near 4 K.

The resonators and amplifiers have been tested in a cryocooler, using a test version of trap electrodes ("dummy trap") as a capacitive load. The parameters of the detection system are summarized in Table 5.2, with the largest Q-values obtained using PTFE insulated NbTi wire and lower values obtained using Formvar insulated NbTi wire. Although Q-values typically drop in the large magnetic field, dip detection is feasible and convenient, for our trap characteristics, with Q-values around 20 000. Of final note here, a variable capacitance in the form of a varactor was added to the amplifier of the CT and BT detector to detune the resonator during the common endcap coupling. However, this was of limited use and ultimately proved decisive in the decision to advance the alternate cooling technique described in Chapter 9.

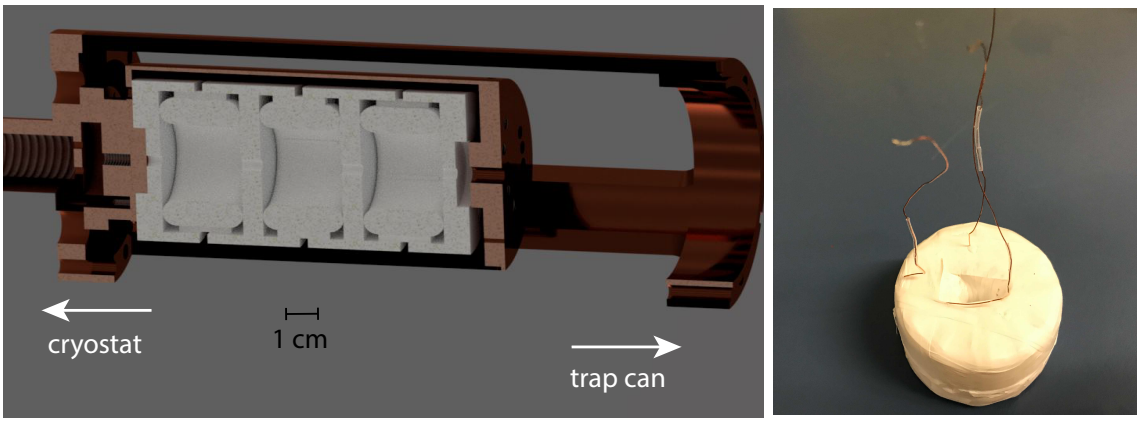

(a) (b)

Figure 5.4: **(a)** A drawing of the axial detection system is shown, consisting of three toroidal coils in an OFHC copper housing. **(b)** Also shown is an image of one of the PTFE wrapped coils.

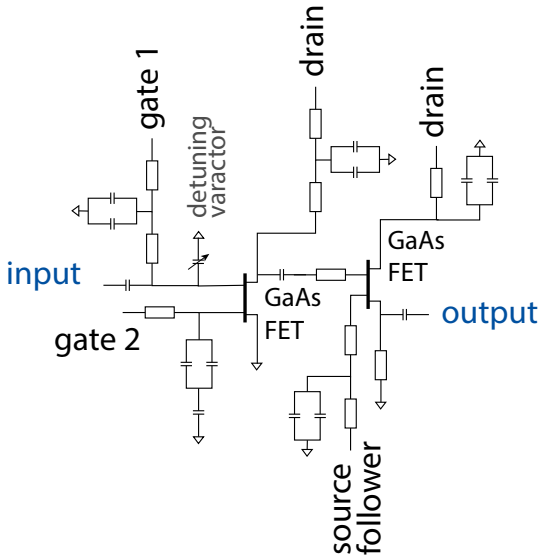

(a)

(b)

Figure 5.5: **(a)** A schematic design of the cryogenic axial amplifier features low-noise GaAs FETs that remain operational at 4 K **(b)** In the apparatus the amplifiers are assembled on small milled circuit board. The one shown here consists of two amplifiers, the AT at the top and the PT at the bottom; the CT/ BT amplifier is located on the back segment of the copper mounting piece.

5.5 Cryomechanical Assembly

First described in [61], the cryomechanical assembly of the proton g-factor experiment remains largely unchanged since the first construction. A liquid helium bath cryostat is connected via solid copper rods and braids to the trap chamber and axial detection systems, thermalizing the entire assembly near 4 K. After isolating sensitive exposed cabling with PTFE tape, the trap chamber and axial detection system is wrapped in superinsulating foil and suspended in a 77 K heat shield by Kevlar threads. This heat shield is itself then wrapped in superinsulating foil and connected to a liquid nitrogen bath cyrostat. Shown in Fig. 5.6, the traps, trap chamber, and shielding are then placed in the bore of a superconducting magnet charged to 1.98 T and pumped to high vacuum. Once cold, the apparatus can be used for months or even years. The results that follow consist of a few experimental runs conducted over nearly three years.

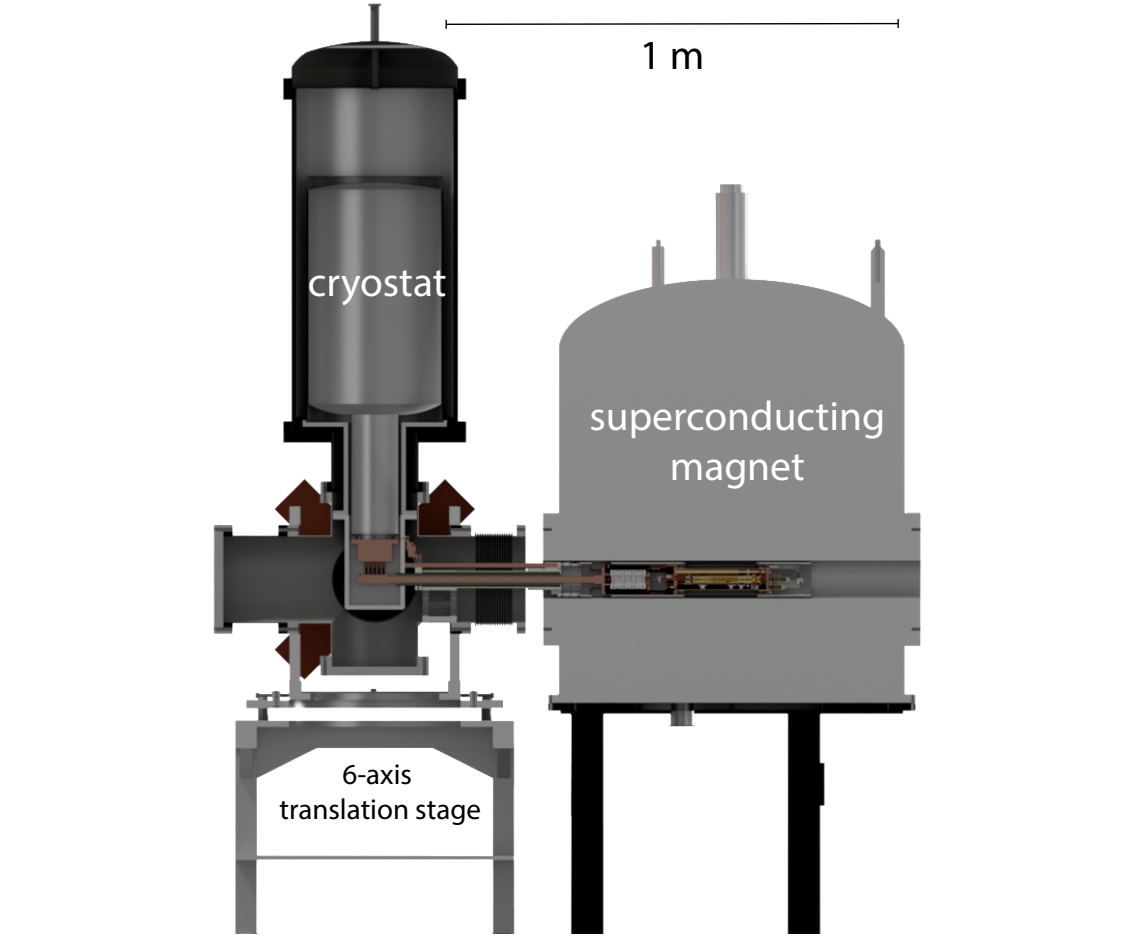

Figure 5.6: The experimental apparatus is shown, consisting of the trap stack and trap chamber inside the bore of a horizontal superconducting magnet. See text for details.

5.6 Laser and Optics Design

The most important new hardware development within this thesis was the addition of lasers to the experiment. This addition includes an ablation laser, used to produce beryllium ions and protons and a laser to address the cooling transition in Be^+ at 313 nm. A complete optical system was built around the cooling laser, including a custom made single mode UV fiber.

5.6.1 Cooing Laser and Optical Beampath

The cooling laser at 313 nm, shown in Fig. 5.7 and Fig. 5.8, is a commercial external cavity diode laser (ECDL) that consists of a fundamental beam that is amplified by a tapered amplifier (TA) and frequency doubled twice in two bow-tie cavity second harmonic generation (SHG) stages[6]. The output of this laser is variably attenuated, polarized, and optionally sent through an acousto-optic modulator (AOM) before being coupled into a UV fiber. In early runs of the experiment, the fiber then went through a vacuum feedthrough and was attached directly to the outside of the trap can. However, this scheme was quickly abandoned as mechanical shifts when the trap is cooled to cryogenic temperatures cause the beam to become misaligned. Instead, the fiber is still used as a mode cleaner but bridges only a short gap between the optical table and the magnet, where an additional optical breadboard has collimating optics and piezo actuated alignment mirrors - shown in Fig. 5.8. Finally, the laser is PID locked to a wavemeter[7], which is referenced to a frequency stabilized, narrow linewidth, 729 nm laser in the Schmidt-Kaler group at the University of Mainz. Frequency stability of the cooling laser is ultimately limited by the wavemeter resolution, around 1 MHz, but is sufficient for the Doppler cooling measurements shown in this thesis.

5.6.2 UV Fiber

While ultimately successfully implemented, the development of single mode 313 nm compatible optical fibers proved to be a major experimental effort. At low wavelengths, optical fibers suffer severe degradation due to solarization, or the formation of color centers. Qualitatively, when exposed to high-energy UV light, the molecular bonds of impurities in the silica are broken and the newly reformed molecules are no longer transparent. In a technique first developed by Yves Colombe at NIST [62], solarization can be overcome by loading the fibers with hydrogen gas and sub-

[6] Toptica TA FHG
[7] HighFinesse WSU-30

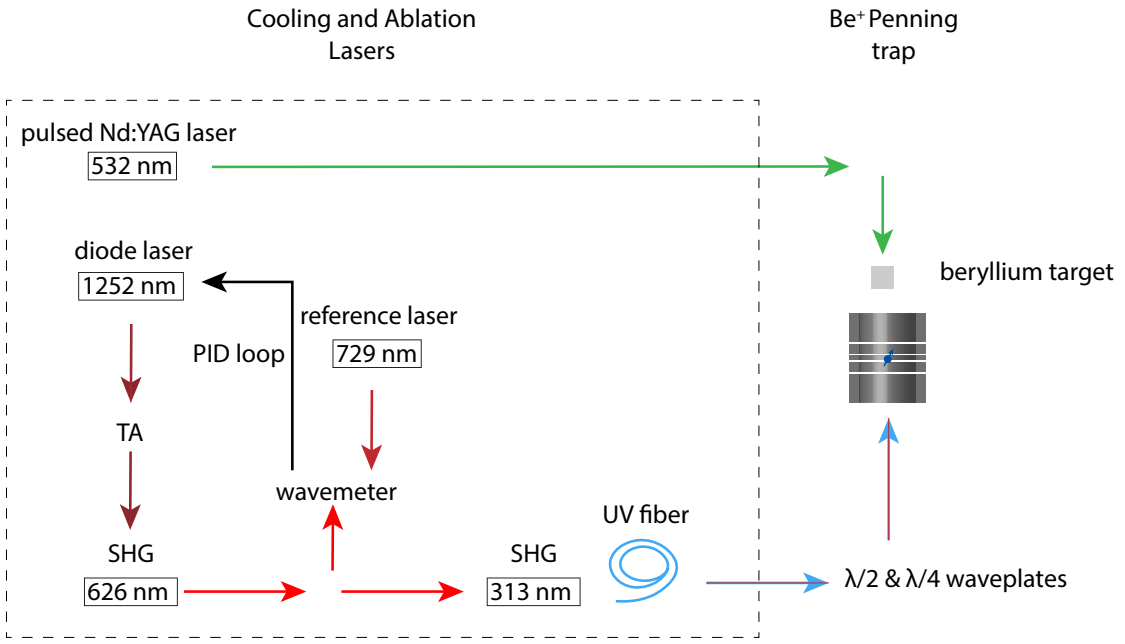

Figure 5.7: Schematic of the lasers used in the new experiment. The cooling laser is locked to a wavemeter and sent through an optical fiber before going to the magnet while a pulsed Nd:YAG laser is used for an ablation ion source, described in Section 4.5.

sequently "curing" with UV light[8]. As a result, when the impurities in the silica are broken by high energy light, the resulting ions form "harmless" hydrides which remain transparent. Once cured, the hydrogen can safely diffuse out with no loss of transmission in the fiber.

A complicating factor though, is the choice of optical fiber. In the most commonly used fibers, the core size and the wavelength of the light defines which modes are transmitted and a sufficiently low core diameter ensures single mode operation. At low wavelength however, the core diameter, or more generally, mean field diameter (MFD) necessary to ensure single mode operation becomes too low for efficient incoupling (MFD $\sim 2\,\mu m$). Photonic crystal fibers then become a more attractive option. In particular, we employ high numerical aperture (NA), "endlessly single mode" photonic crystal fibers, constructed of pure silica with a series of hollow holes around the core acting as an effective cladding[9] shown in Fig. 5.9. This hole structure presents a serious problem during hydrogen loading and care must be taken to melt, or collapse, the two ends of the fiber with a fiber splicer. The "recipe" used for preparing UV fibers is presented below, including the rather unique approach to

[8]Since 2014 a small community of "homebuilt" UV fiber users has sprung up consisting of, among others, the Schmidt group at PTB and the Blatt group at Innsbruck both of which provided valuable insight and assistance while developing these fibers in Mainz.

[9]NKT Photonics LMA-PM10-UV

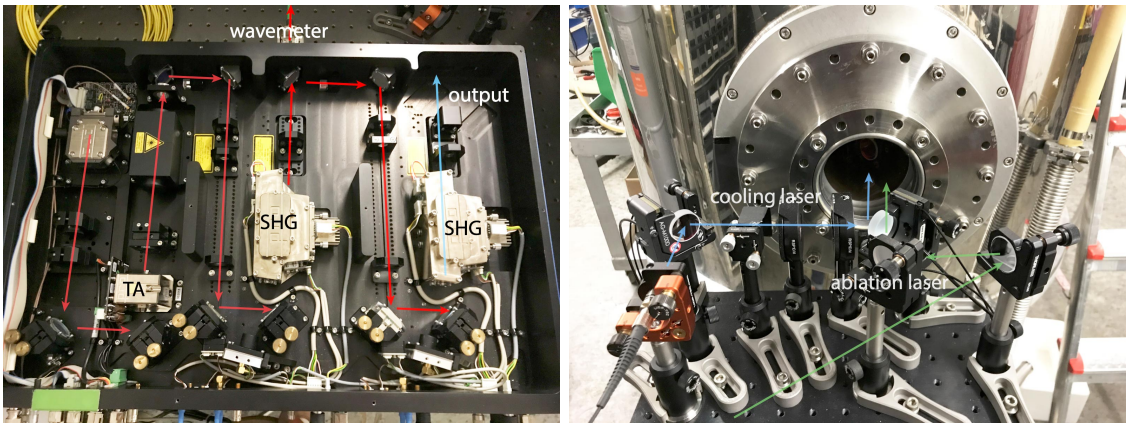

(a) (b)

Figure 5.8: **(a)** A view of the commercial ECDL used to Doppler cool beryllium ions and **(b)** the beam path of the cooling laser and ablation laser entering the magnet.

connectorization that I developed during this thesis[10].

UV Fiber Recipe

1. Collapse both ends of the photonic crystal fiber. If left unsealed, hydrogen will diffuse out of the fibers in around twelve hours.
2. Load the fibers with hydrogen gas at high pressure. Typically we send our fibers out to have this done externally[11]. The fibers are placed in a chamber filled with 100 bar of H_2 gas for ten days. The fibers are then shipped back with icepacks to slow diffusion.
3. The fibers can be safely stored in a standard 0 °F or −18 °C freezer for several months until ready to use.
4. When ready to cure, collapse one end of the fiber again if necessary. Cleave off the remaining uncollapsed region. When using the fiber splicer while the fiber is hydrogen loaded large bubbles tend to appear from rapidly expanding gas. As a result, it is best practice when collapsing the fiber to work "outward" i.e. sweeping the splicer toward the nearest open end.
5. Prepare the connector.
   (a) Prepare a repurposed syringe needle by removing any plastic attached. The needle should be sufficiently large to allow the fiber to pass cleanly through.

[10] In the near future, ready-to-use commercial UV fibers may become available. Both the Schmidt group at PTB and the Eikema group in Amsterdam have reported some success in ordering custom pre-cured and connectorized fibers in addition to the results shown in [63].

[11] AOS GmbH

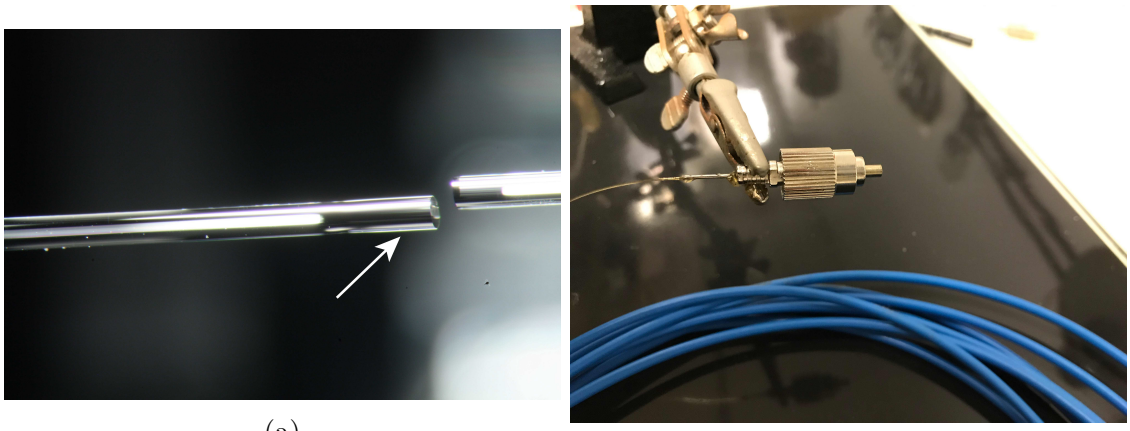

(a) (b)

Figure 5.9: **(a)** A view of a collapsed photonic crystal fiber. The illuminated bands are the result of a hole structure that acts as a cladding, while the clear region is where this structure has been re-fused, marked with an arrow. **(b)** An example of a cured, connectorized, and polished fiber following the recipe given here. The fiber is glued into an additional needle which is then glued into an FC/PC connector, reducing incoupling losses from stress induced birefringences.

(b) Slide the needle into an FC/PC connector and slide the fiber, with a small amount of coating stripped at the end, into the needle and out the face of the connector.

(c) With a durable epoxy, glue the needle into the connector and when set, glue the fiber into the needle with low expansion epoxy. The uncollapsed region of the fiber should not extend past the surface of the connector as this will be polished away. The needle allows the fiber to be glued further away from the area where the incoming light is modematched, and where stress induced birefringence must be minimized.

(d) Polish the end of the fiber, working with increasingly finer polishing sheets - here 15 µm, 6 µm, 3 µm, 1 µm, and finally 0.3 µm grit sizes. Note that at this point it is only necessary to connectorize one end of the fiber before curing.

(e) Alternatively, the fiber can be cleaved as shown in Fig. 5.9**(a)**. In contrast to other groups we found the polishing to be more robust and have used it nearly exclusively.

6. Optimize the coupling as well as possible and cure for a few days. The amount of time necessary has not been characterized in our group but working fibers have been produced after roughly 72 hours of curing with, at most, a few hundred µW of transmitted power at 313 nm.

7. Attach protective fiber shielding and connectorize the remaining end.

Although not extensively studied, fibers prepared using this method have remained operational after around two years of use with no loss in transmission. Shown in Fig. 5.10, a similar, uncured fiber rapidly solarizes within hours.

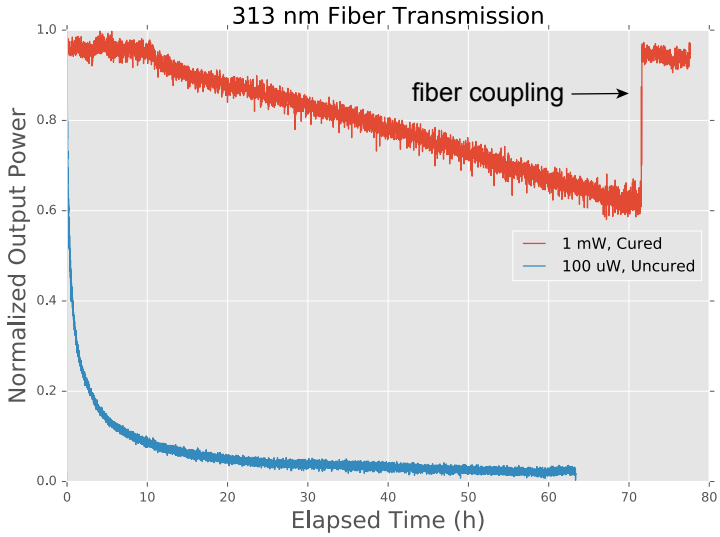

Figure 5.10: A comparison of cured and uncured optical fibers while monitoring transmission of 313 nm light is shown. During this measurement the coupling into the cured fiber drifted significantly and the coupling into both fibers was optimized at the end (see the jump at ~ 72 h). The cured fiber showed no measurable loss in transmission while the uncured fiber showed nearly complete loss in transmission.

5.6.3 Fluorescence Detection

Unique to precision Penning trap experiments based on image current detection, the latest version of the Mainz proton g-factor apparatus features an in-situ fluorescence detection system. In fact, as described in Chapter 6, the results presented here are some of the first measurements combining simultaneous image current and fluorescence detection. The constraints of the experimental apparatus made the design of this system difficult, and the focus of significant experimental developments - described both here and in [64, 65]. In particular, the combination of a cryogenic environment with the limited optical access of a small diameter magnet, $\varnothing = 9$ cm, meant that the common method of using a photomultiplier tube (PMT) or CCD camera was infeasible. Instead, as shown in Fig. 5.11, we utilize a sixfold split ring electrode in the BT, with a small gap between electrodes to collect fluorescence, which is then read out by cryogenic silicon photomultipliers (SiPMs)[12]. Featuring 6° slits between electrodes, 36° total collection angle, and quantum efficiency around 10% at 313 nm and 4 K, we estimated a fluorescence signal at the tens to hundreds

[12]SensL Series C. Cryogenic operation was first shown in [66] and the Achenbach group at the University of Mainz provided valuable assistance in soldering and working with these SiPMs.

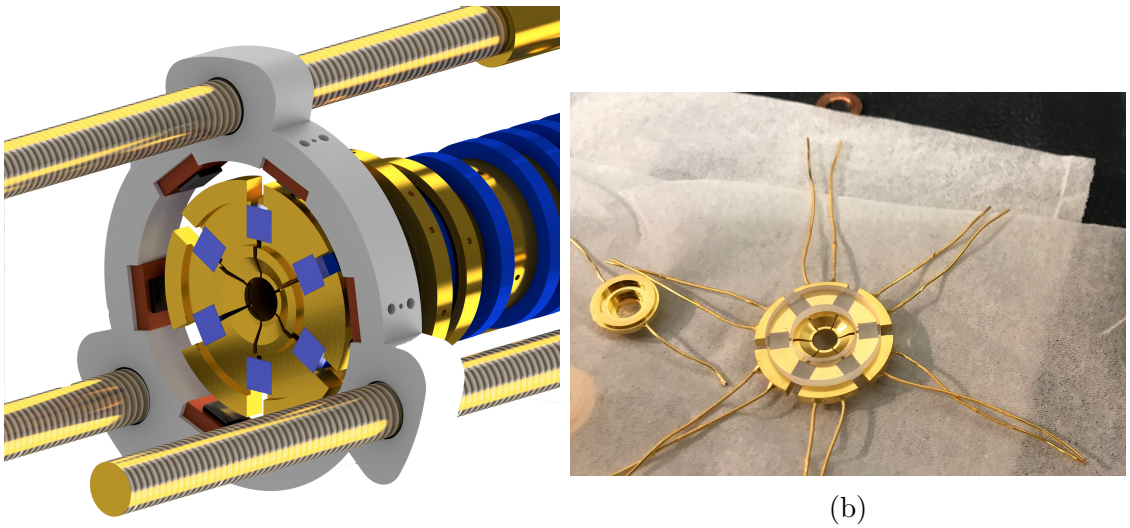

(a) (b)

Figure 5.11: **(a)** An illustration of the split BT electrode with an array of six SiPMs to read out the fluorescence signal. **(b)** The split ring electrode before assembly. The electrodes are spaced by polished quartz blocks and held in place by a large quartz ring, designed, as described in Section 4.2, to minimize the trap capacitance.

of nA level for $N_{Be} \sim 10 - 100$. In fact, using readout electronics described in [64], we have been able to count single fluorescence photons and are limited only by background counts due to scattered photons. Further results using the setup described here are given in Chapter 7 and future improvements, including stray light shielding are described in [67].

5.7 Ablation Source

In previous versions of this apparatus, protons were loaded with an electron gun. Located on one end of the trap stack, the resulting electron beam impinged upon a hydrocarbon target on the opposite side, in theory releasing and ionizing hydrogen. The design and usage of the electron gun is first described in [26], with details of the upgraded and current version described in [68]. However, it was found in our experiment, as well as the in BASE experiment at CERN, that protons could be produced even without the target, suggesting that, in reality, frozen out residual gas is liberated and ionized by the electron beam. Unfortunately, the use of an electron beam to produce beryllium ions poses some difficulty. As an alkaline earth metal, beryllium tends to be very "sticky" and earlier experiments from the highly charged ion group in Mainz [69, 70, 27] had to employ special techniques to produce calcium - even in a highly optimized electron beam ion source [27]. As a result, our new apparatus includes a new in-trap ablation source, initially used to produce beryllium

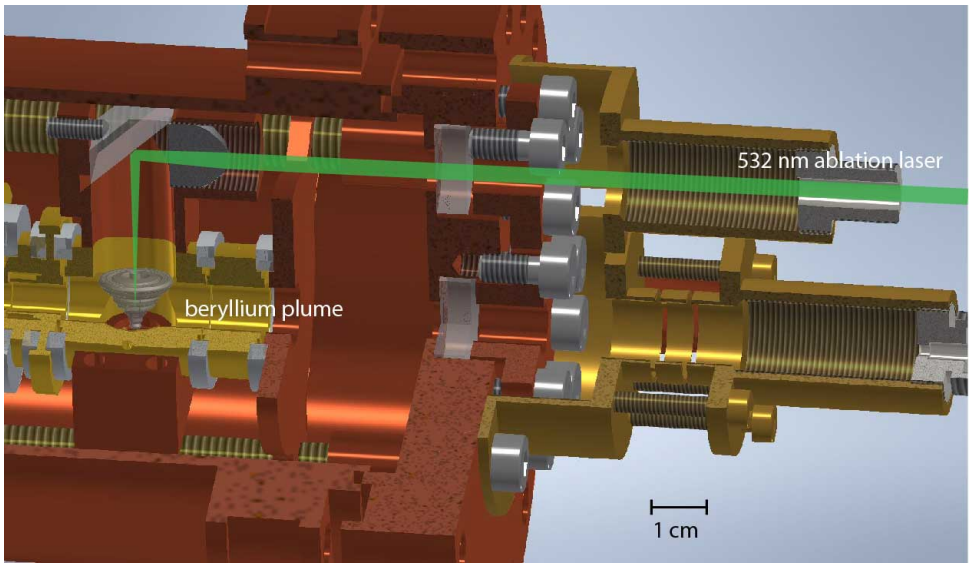

Figure 5.12: Illustration of ablation loading in the new apparatus. The pulsed 532 nm laser is sent into the trap chamber where it is tightly focused onto a beryllium target; frozen residual gas on the target also allows protons to be loaded with the same source.

ions, and later also used to produce protons.

Illustrated in Fig. 5.12, laser ablation uses a high intensity laser to rapidly heat a target, releasing a hot plume of atoms or plasma. In our case a pulsed, ns, frequency doubled Nd:YAG laser[13] at 532 nm is sent through the trap chamber and tightly focused onto a beryllium target, visible in Fig. 5.13. Originally envisioned with in situ optical fibers like with the cooling laser, the current design uses a free running beam, as the necessary pulse energy, around 1 mJ induced surface damage even before damaging the rest of the large multimode fibers. Alternatively, the source could be redesigned to use very large mode area photonic crystal fibers, although the benefits are likely to be minimal as the ablation laser light is easily brought into the trap at present. Typical parameters for the ablation source, as well as loading procedures are described in the following chapter.

[13]Continuum Minilite

(a) (b)

Figure 5.13: **(a)** An image of the assembled beryllium target and optics along with **(b)** a close-up view where the previously ablated region is visible.

Chapter 6

Trap Characterization

Following the design and assembly of the new experiment, a significant effort was made to thoroughly characterize the traps. In particular, the AT and the PT parameters are crucial for the laser cooling measurements in Chapter 8 and Chapter 9. To resolve spin flips an extremely strong magnetic bottle is required in the AT. Due to this strong magnetic bottle though, it is difficult and time consuming to find the ideal operating conditions in the trap. However, even without a g-factor measurement, it is an indispensable tool that enables highly sensitive temperature measurements. The PT, meanwhile, is comparatively easy to set up initially. However, a complete characterization, especially necessary when used for temperature determination, requires many detailed measurements. Note that while all homogeneous traps (i.e the ST, PT, CT, and BT) were used, the PT was the most characterized and the most important in demonstrating sympathetic cooling of protons. Still, the techniques shown here are broadly applicable and were used in general for all traps.

6.1 Loading and Cleaning

6.1.1 Loading and Mass Spectra

After a period of initial setup and trap characterization, it is usually sufficient to begin cleaning and particle preparation immediately. As shown in Fig. 6.1, however, a "mass spectrum" measurement provides useful identification of the trap contents and can be especially useful with a new or unknown trap. In our case, when first beginning ablation loading, little was known about the traps, the loading procedure, or the laser itself. In a mass spectrum measurement, a parametric drive (see Section 2.1.5) at $\nu_{\mathrm{rf}} = 2\nu_0$, where ν_0 is the resonator frequency, is applied and the ring voltage is swept over a large range. The detector signal, readout either with low averaging time on the FFT analyzer or with a spectrum analyzer, then shows a peak

at a time and ring voltage corresponding to

$$\omega_z\left(m_i, V_{r,i}\right) = \omega_0 \tag{6.1}$$

where m_i is the mass of the identifiable species.

Figure 6.1: Three mass spectra taken in the ST are shown. Typically beryllium ions are loaded at lower pulse energies than protons. The measurement shown here was intended to find the transition point between optimal beryllium loading energy and optimal proton loading energy. In the ST, this configuration is optimized for the beryllium ions although, as seen in the second x-axis, the different voltage supply configuration introduces offsets in the ring voltage (and thus mass). The beryllium ions appear as a large, clean peak while the proton peak is smeared out and decays with successive scans in which high energy particles escape the trap at low voltages.

Once the particle of interest is found in the mass spectrum it is relatively straightforward to continue with trap characterization, but first any other ions present must be removed.

6.1.2 Cleaning

The next essential part of preparing particles for use in measurements is cleaning, i.e. removing unwanted ions. This is especially challenging in Penning traps which provide radial confinement up to a few hundred eV. In addition, we suspect that we create ions with unusual orbits that are hard to detect since the beryllium target, and likely ionization region, is far off center. Described here are some of the cleaning

techniques used as well as a complete cleaning routine for both beryllium ions and protons.

Axial and Radial Excitations

During a simple cleaning procedure the trap is kept at a fixed ring voltage so the particle has fixed axial frequency, ν_z, and a frequency swept excitation that avoids the trap frequencies is applied. Shown below are the regions of interest, where various frequency sweeps are used to prepare an ion with mass m_i.

$\nu_- \to \nu_z$ excites the axial mode of all ions with mass $m > m_i$

$\nu_z \to \nu_+$ excites the axial mode of all ions with mass $m < m_i$

$\nu_+ \to \infty$ excites the cyclotron mode of all ions with mass $m < m_i$; usually this is not particularly effective.

After one or more of these excitations, the trap is "lowered" by ramping the ring voltage. During this ramp, $|V_r| \to |V_{r,\text{loss}}| > 0$, where $|V_{r,\text{loss}}|$ is the energy dependent ring voltage at which particles are no longer confined. More concretely, the ions of interest are kept near the temperature of the resonator while the contaminant ions are excited and undamped. When the potential is lowered the contaminant ions have energies larger than the trap depth and $|V_{r,\text{loss}}|$ can be thought of as an evaporation point.

An additional note is that while sweeps tend to be most straightforward, it is also possible to apply broadband excitations with an arbitrary waveform generator that cut out (or inversely, address) narrow frequency bands around the mode frequencies. These are referred to as stored waveform inverse Fourier transform (SWIFT) excitations and, while used initially, proved less reliable than the sweeps described here.

Instability Cleaning

Another simple, but remarkably effective cleaning procedure is to ramp the ring voltage $V_r \to V_{r,\text{ins}}$ where $V_{r,\text{ins}}$ is the instability voltage given by $\nu_z(V_{r,\text{ins}}) \approx \nu_c/\sqrt{2}$ so that all particles with mass $m > m_i$ will no longer be trapped. To implement this, we use large, high voltage compliant capacitors to filter the biasing lines of both the AT and the ST ring electrodes. This allows us to apply sufficiently high voltages to remove all ions except protons in the AT, where the lower B_0 produces a lower cyclotron frequency and the instability voltage is approximately $V_{r,\text{ins}} \approx 250\,\text{V}$. Similarly, ramping to $V_{r,\text{ins}} \approx 130\,\text{V}$ in the ST is sufficient to remove all ions with mass $m > 10\,\text{u}$.

Magnetron Cleaning

For a given ring voltage, the magnetron frequencies of all species lie roughly within 1 kHz of each other. As a result, the magnetron sideband, ν_{SB-}, can couple the magnetron mode of the ion of interest to the axial mode, which is in turn, exclusively coupled to the resonator. An excitation at and around ν_- then excites the magnetron mode of all species while the magnetron mode of the particle of interest is damped. An FFT spectrum during this procedure looks like a double dip with an additional peak at the axial frequency. When using this cleaning method, contaminant ions are not removed but excited to a large magnetron radius where the strength of the excitation field drops to zero. It is often useful then to transport to another trap with a smaller radius (e.g. ST to BT or PT to AT) to completely remove the excited particles.

Separation Cleaning

Described here, and illustrated in Fig. 6.2, separation cleaning is a new, highly deterministic cleaning method developed using some of the methods first shown in [71]. First, the ring voltage (in this case of the PT) is quickly ramped up to near the maximum of the voltage supply (for the UM-1-14, 14 V), splitting the ion cloud, along with any contaminants into two regions. One part of this cloud can be transported to a storage region while the other is be brought back into resonance with the detector. If cleaning a single particle, the presence of a dip indicates that the storage region should be emptied while the absence of a dip indicates that the contents of the storage region should be transported back. The number of contaminants will thus decrease geometrically by $N = N_0 P^n$ where N_0 is the starting population, n is the number of cycles, and P is the probabilistic fraction of the population that remains in the trap, typically $P \sim 0.5$.

In practice, the fraction of ions separated into the right or left potential well (in Fig. 6.2 the PT and the storage region) is determined by small offsets in patch potentials on the electrodes. These are compensated experimentally by applying slightly different voltages to each electrode and the population remaining in the trap can be adjusted by tuning these offsets. This cleaning technique has proven to be very reliable and extremely attractive for preparing single, clean particles. Separation cleaning works for all masses and all frequencies, relying only on an axial detection system that enables deterministic reduction of all unwanted ions.

Laser Dissociation

Present in nearly every ion trap, unwanted molecular ions can form during ion creation or from inelastic collisions with hydrogen gas. This results in trapped

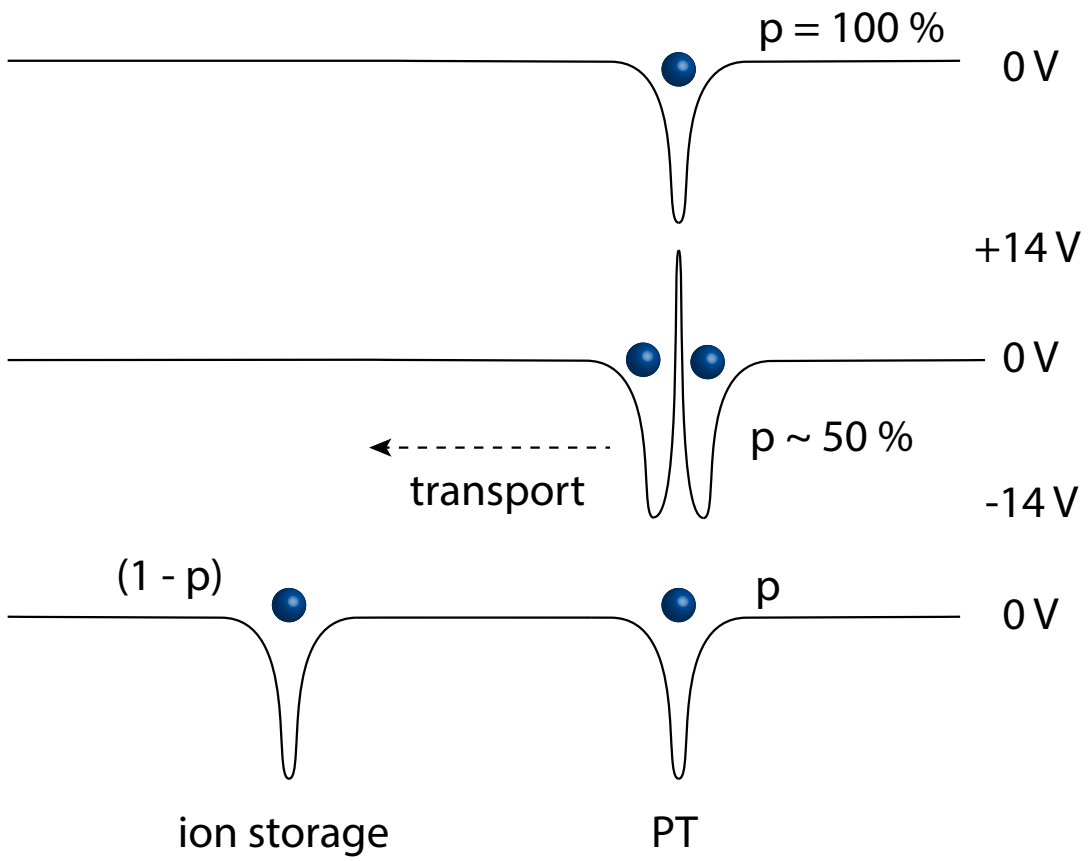

Figure 6.2: The separation routine is illustrated in which a voltage ramp in the PT splits the ion cloud along with any contaminants into two clouds - one of which is then transported to a storage region. With only ions from either the PT or the storage region retained, single, clean particles can be prepared with high confidence. See text for details.

hydrides AH^+, where A is a earth alkali (or similar) ion. While BeH^+ is extremely difficult to remove, the dissociation energy of BeH is near 2.4 eV [72], far below the energy of the cooling laser at around 4 eV. While not resonantly enhanced, we observe an increase in dip width, $\gamma_{Be} \propto N_{Be}$ when first applying the cooling laser, suggesting both the presence of BeH^+ in the trap and the effectiveness of laser dissociation as a cleaning method.

6.1.3 Particle Preparation Recipes

Although all of these techniques are well established and commonly used, preparing clean, single particles after ablation loading has consumed a very outsized fraction of my experimental work. Presented below then, is a kind of heuristic recipe that can be used to prepare single protons and stable clouds of beryllium ions.

Protons

1. Load the ST by firing a single pulse from the ablation laser with pulse energy near 1.4-1.7 mJ. The necessary pulse energy is higher for protons than for beryllium ions due to the difference in ionization potentials.

2. Ramp the ST ring voltage to $-250\,\mathrm{V}$ to remove contaminant ions with mass $m > 4\,\mathrm{u}$.

3. It is not necessary to cool or observe the protons in the ST, transport directly to the PT.

4. Apply aggressive (i.e. at amplitudes near the amplitude where the proton is lost) sweeps from $\nu_- \rightarrow \nu_z$ and ramp the ring voltage to around -100 to $-200\,\mathrm{mV}$. As described in the Axial and Radial Excitation method, this excites ions with mass $m > m_p$ which escape the trap once lowered.

5. Transport to the AT and ramp the ring voltage to $-175\,\mathrm{V}$. This should be repeated, going up to $-225\,\mathrm{V}$, but not in a single step. While the number of protons will decrease with each subsequent ramp, immediately ramping to $-225\,\mathrm{V}$ will cause the entire cloud to be lost.

6. The only particles remaining should be protons, although there could be protons trapped on a large radius which remain invisible to the detector. The final step is then separation cleaning. Ten repetitions puts the probability of having any contaminant, even given large initial populations of $N_0 \sim 1000$, to below a percent.

Beryllium

1. Load the ST with lower pulse energy - around 0.7 mJ.

2. Ramp the ST ring voltage to up to $-125\,\mathrm{V}$, starting around -75 to $-100\,\mathrm{V}$, similar to the procedure with the proton in the AT.

3. The only species remaining should have mass $m < 10\,\mathrm{u}$ and can be cleaned with sweeps of increasing amplitude from $\nu_z \rightarrow \nu_+$

4. Finally, apply the cooling laser. The laser frequency can be, but does not need to be, far from resonance. However, if near resonance, the magnetron mode will need to be cooled by the sideband drive.

6.2 Precision Trap

6.2.1 Tuning Ratio Optimization

The most important parameter in precision Penning-trap experiments using image current detection is the tuning ratio, TR, defined, as before, as $\mathrm{TR} = V_{ce}/V_r$. V_{ce} and V_r again, are the voltages on the correction and ring electrodes as illustrated in Fig. 3.2 and described in Section 2.1.2. Using the BASE convention [26], we introduce a new unit, the "Unit", defined as $1\,\mathrm{U} = 1$, with the more commonly used $1\,\mathrm{mU} = 1 \times 10^{-3}$. Typically, the ideal experimental tuning ratio must be known to around 10 mU to resolve a dip, while during precision measurements such as the 2017 g-factor measurement it was determined and set to a precision $\Delta\mathrm{TR} = |\mathrm{TR}_{\mathrm{applied}} - \mathrm{TR}_{\mathrm{ideal}}| < 1 \times 10^{-5}$. The ideal tuning ratio can be determined theoretically, but in practice the value found in experiments is used to account for voltage offsets and patch potentials.

SNR Method

The first, and easiest, method to determine the tuning ratio is to measure the signal-to-noise ratio, defined by a fit parameter as the bottom of the dip to the top of the resonator. C_4 can be written as $C_4(\mathrm{TR}_{\mathrm{applied}}) = D_4\,\Delta\mathrm{TR}$ and Eq. (3.22) gives the shift of the axial frequency due to nonzero axial temperature and nonzero C_4 as

$$\frac{\Delta\nu_z}{\nu_z} = \frac{3}{4}\frac{1}{q}\frac{1}{V_0}\frac{C_4}{C_2^2}E_z. \tag{6.2}$$

Since the proton continually samples the energies of the Boltzmann distribution of the axial resonator, the SNR of the dip is reduced and given by

$$\mathrm{SNR} = -20\,\mathrm{Log}_{10}\left(\frac{\mathrm{Re}\left[Z(\omega_z\,(C_4 = 0) + \omega_z\,(C_4 = C_{4,\mathrm{applied}}))\right]}{R_p}\right) \tag{6.3}$$

where $Z(\omega)$ is the impedance of the combined particle-detector system and R_p is the effective resistance of the detector, $R_p = Q\omega L$ on resonance. An example of this measurement is shown in Fig. 6.3 where the ideal tuning ratio is taken to be the tuning ratio that yields the largest signal-to-noise ratio. In Chapter 8, Eq. (6.3) is written explicitly and used to extract the temperature of the detection system.

Burst Method

Alternatively, and more precisely, the tuning ratio can also be found by exciting the magnetron mode and measuring the shift of the axial frequency as a function of the

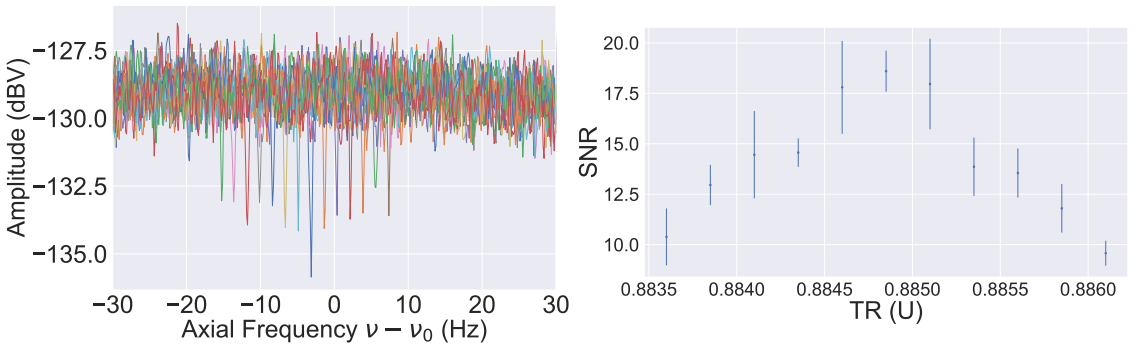

(a) (b)

Figure 6.3: **(a)** An illustrative series of dips with tuning ratios yielding varying SNR. **(b)** A different dataset here shows the results of a similar measurement in which the dip is placed at the center of the resonator for each tuning ratio, minimizing unwanted corrections to the lineshape.

magnetron energy E_-. Again, using Eq. (3.22), this shift can be written as

$$\frac{\Delta\omega_z}{\omega_z} = \frac{3}{q\,V_0}\frac{C_4}{C_2^2}E_-. \tag{6.4}$$

The magnetron mode is excited by an rf burst at the magnetron frequency ν_- and the burst number n defines the magnetron energy,

$$E_- = n^2\alpha_{-,i}. \tag{6.5}$$

Here, $\alpha_{-,i}$ is an experimental factor that depends on the parameters of the excitation lines and the drive amplitude. Fig. 6.4 **(a)** shows a measurement of the axial frequency shift $\Delta\nu_z$ and a polynomial fit gives the values of C_4 and C_6. Fig. 6.4(**b**), meanwhile, shows the shift per detuning from the ideal tuning ratio. The ideal tuning ratio, in turn, is given by the zero crossing of the C_4 shift. Although not used here, by adjusting the drive strength by a known amount, $\alpha_{-,2} = k\alpha_{-,1}$ we can take the two slopes m_1, m_2 and extract κ_{D_4} by

$$2\kappa_{D_4} = m_1 + m_2 k. \tag{6.6}$$

As discussed in Chapter 8 this an important parameter for determining the resonator temperature.

6.2.2 PT B_2 Measurement

Although many orders of magnitude lower than in the AT, the magnetic bottle in the PT produces a small, but important B_2 term. Frequency shifts due to $B_{2,\mathrm{PT}}$

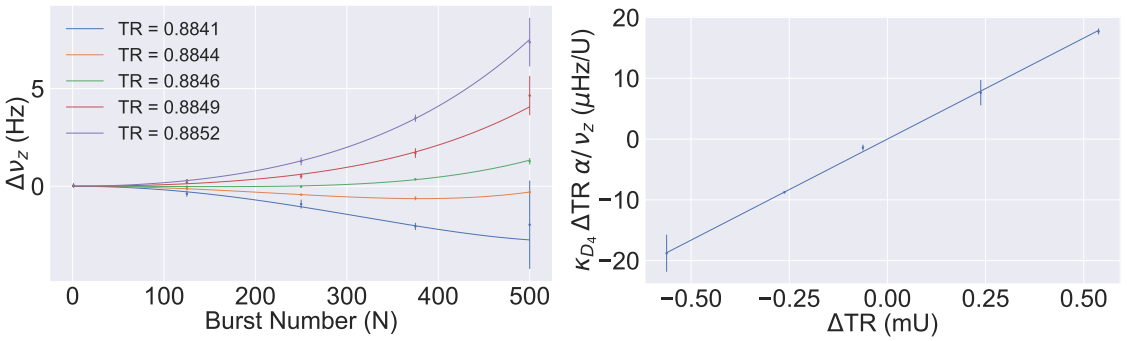

(a) (b)

Figure 6.4: **(a)** Applying a burst excitation to the trap excites the magnetron motion of the particle to an energy given by Eq. (6.5). Applying a second order polynomial fit to the points shown yields values of C_4 and C_6 for a given tuning ratio. **(b)** The quantity $\kappa_{D_4}\Delta\mathrm{TR}\alpha/\nu_z$ is given by the slope shown, with the zero crossing the ideal tuning ratio. The slope proportional to C_6, or κ_{D_6}, is not shown but consistent with zero for the range of tuning ratios shown here.

are a significant systematic effect in a g-factor measurement but can also be used to measure the temperature of the axial detection system as described at the end of this chapter.

To measure B_2 we first introduce a nonzero C_4 through a tuning ratio offset, ΔTR, and then measure the modified cyclotron and axial frequencies at a given magnetron energy. We then excite the magnetron mode with an rf burst near ν_- and measure the modified cyclotron and axial frequencies again. The two frequency shifts are then $\Delta\nu_+ = \nu_{+,2} - \nu_{+,1}$, $\Delta\nu_z = \nu_{z,2} - \nu_{z,1}$ where the subscript $1, 2$ corresponds to frequencies measured at the initial and final magnetron energies, respectively. From Eq. (3.22), the shift of the axial frequency due to nonzero magnetron energy can be written as

$$\Delta\nu_z = 6\frac{C_4}{C_2}\frac{E_-}{m\nu_z}. \tag{6.7}$$

Meanwhile from Eq. 3.54, the shift of the modified cyclotron frequency due to nonzero magnetron energy can be written as

$$\Delta\omega_+ = 2\frac{\omega_+}{\omega_z}\frac{B_2}{B_0}\frac{E_-}{m\omega_z}. \tag{6.8}$$

After rearranging Eq. (6.7) and Eq. (6.8), B_2 can be written as,

$$B_2 = 3\frac{\nu_z}{\nu_c}B_0\frac{C_4}{C_2}\frac{\Delta\nu_+}{\Delta\nu_z}, \tag{6.9}$$

and $B_{2,\mathrm{PT}}$ can be extracted from the measured ratio $\Delta\nu_+/\Delta\nu_z$. The results of such a measurement are shown in Fig. 6.5 with

$$B_{2,PT} = -0.39 \pm 0.11\,\mathrm{Tm}^{-2}. \tag{6.10}$$

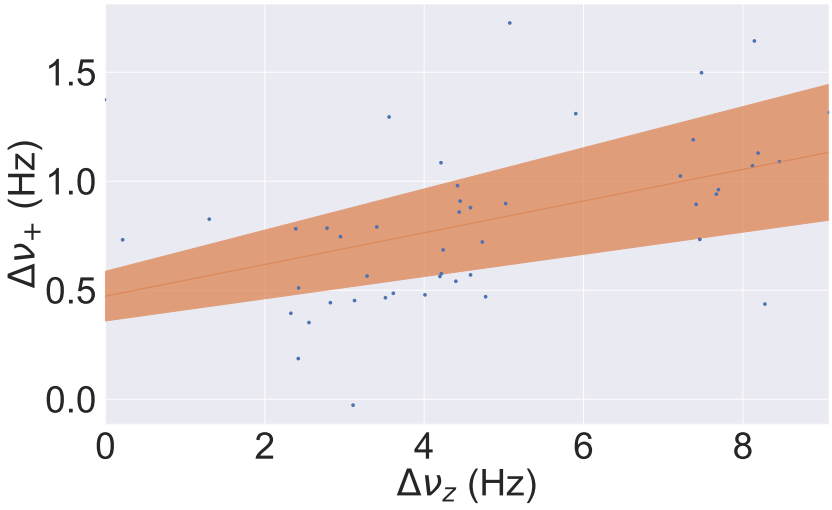

(a)

Figure 6.5: **(a)** Measurement of $B_{2,PT}$ by measuring the cyclotron frequency at varying magnetron radii. The slope shown here (orange line with error bands) is used in Eq. (6.9) to produce the value given in Eq. (6.10). The excitation strength required in this measurement was very large and cause the large scatter shown here.

6.3 Analysis Trap

Due to the size of the magnetic bottle, the AT is difficult to operate and set up. As in Section 2.2.1 and Eq. (3.54), the axial frequency shift due to B_2 can be written as,

$$\Delta\nu_z = \kappa_{B_2}\left(E_+ + |E_-|\right) \tag{6.11}$$

with

$$\kappa_{B_2} = \frac{\hbar}{4\pi m\nu_-}\frac{B_2}{B_0}k_B. \tag{6.12}$$

For the beryllium ion, $\kappa_{B_2} \approx 10\,\mathrm{Hz/K}$, and is a factor of $m_p/m_{Be} \approx 9$ larger for the proton. In more concrete terms, if the cyclotron energy of the proton is Boltzmann distributed with a temperature of $T_+ = 4\,\mathrm{K}$, the axial frequency in the AT will be distributed over a few hundred Hz. On the other hand, if the cyclotron mode is thermalized by an axial detector, with resulting temperature $T_+ = T_z\,\nu_+/\nu_z$, the axial frequency in the AT will be distributed over a few kHz, or several hundred detector linewidths. As a result, the AT was characterized first with a single beryllium ion, narrowing the trap parameter space when working with the proton.

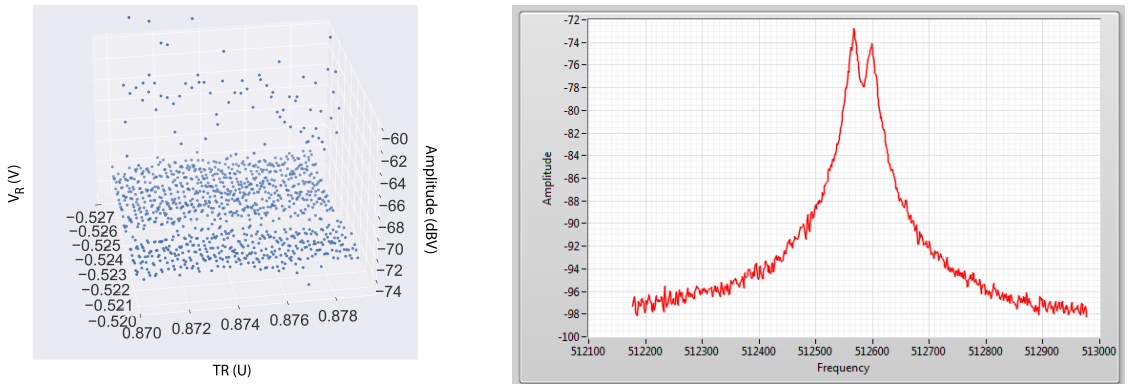

(a) (b)

Figure 6.6: **(a)** A typical example of a $2\omega_z$ search, where the tuning ratio and ring voltage are scanned and the maximum FFT signal is plotted. The range of peaks indicates a region where we can search for the dip directly. **(b)** The first proton dip in the new apparatus, following a $2\omega_z$ scan in **(a)**[1].

6.3.1 Particle Searches

When commissioning the AT, there is uncertainty in both the tuning ratio TR and ring voltage V_r, arising from patch potentials, asymmetric electrodes, or other manufacturing imperfections. This, of course, is in addition to the uncertainty in V_r and TR from the radial energy. Typically, both of these parameters can be calculated to around 5 to 10%. Afterwards, the best one can do is a two dimensional parameter scan. We proceed then in two steps, first with a "$2\omega_z$" scan in which a parametric excitation is applied to the trap and the ring voltage and tuning ratio are scanned. A typical example of such a scan is shown in Fig. 6.6, and the parameter space is narrowed down to the area in which a peak appears. This process is then repeated without the excitation drive and we search dip signals on the resonator.

6.3.2 Tuning Ratio and B_4 Measurement

As in other traps, the most important trap parameter is the tuning ratio, TR. However, the magnetic bottle also introduces a shift of the axial frequency $\Delta\nu_z \propto B_4\,\mathrm{TR}\,E_+$, meaning that the ideal tuning ratio must be found for varying cyclotron energy. At large energies, e.g. when the cyclotron mode of the proton is sideband cooled, the tuning ratio range necessary to resolve a dip can be less than a few mU. A measurement of the ideal tuning ratio for a given radial temperature yields a value of

$$\mathrm{TR}_{\mathrm{ideal}} = 0.881 \pm 0.018\,\mathrm{Hz/mU} \rightarrow B_4 = 69 \pm 2\,\mathrm{mT/mm}^4. \tag{6.13}$$

[1]This rather unremarkable and ugly dip, shown in LabView 2015 glory was the result of several months effort.

Additionally, because axial frequency shifts $\Delta\nu_z \propto C_4$ are difficult to measure in the presence of a large B_2, the ideal tuning ratio is found only by maximizing the SNR of the dip. In many cases, and during the 2017 g-factor measurement, the tuning ratio is applied through the relation,

$$\mathrm{TR}_{\mathrm{applied}} = \mathrm{TR}_{E_+=0} \cdot E_+ \, B_4 \tag{6.14}$$

where $\mathrm{TR}_{E_+=0}$ is the ideal tuning ratio at zero temperature, E_+ is the radial energy of the proton and B_4 is given by Eq. (6.13).

6.3.3 B_2 and ν_+

In homogeneous traps the radial frequencies $\nu_\pm$ are easily measured with a sideband drive (see in Section 2.1.5), yet such techniques fail in the AT. If attempted, the sideband drive would change the radial energy and shift the axial frequency until the sideband drive was no longer resonant. As a result, we measure the modified cyclotron frequency ν_+ by exciting the motion of the particle directly with a drive at $\nu_{\mathrm{rf}} = \nu_+$ as in Refs. [60, 73]. At very low amplitudes the drive introduces a small frequency jump and increases the axial frequency jitter. As shown in Fig. 6.7, a drive at $\nu_{\mathrm{rf}} = \nu_+ - \delta_n$ is continually applied and for each δ_n we measure two axial frequencies, $\nu_{z,n-1}$, $\nu_{z,n}$. At low excitation energies the jitter increases only when the drive is resonant with the modified cyclotron mode.

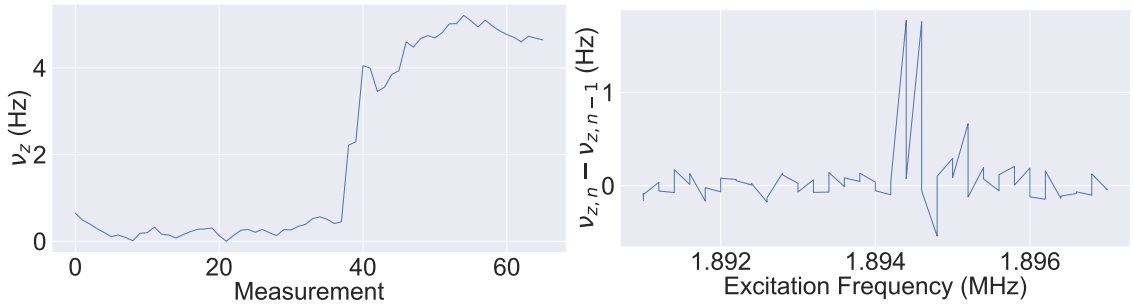

(a) (b)

Figure 6.7: **(a)** A measurement of the mean frequency while an excitation is applied near ν_+ is shown. **(b)** During the same measurement the axial frequency jitter is taken from $\nu_{z,n} - \nu_{z,n-1}$.

Using this method, we also measure ν_+ with varying axial position $\langle z \rangle$ by introducing an offset voltage to one of the electrodes. This offset shifts the center of the trapping potential deterministically, with the value $\langle z \rangle$ as a function of V_{offset} given by the trap geometry. Shown in Fig. 6.8, the measured ν_+ can be converted to a magnetic field value B, and a fit to the data gives,

$$B_{2,AT} = 297\,000 \pm 43\,000\,\mathrm{T/m^2}. \tag{6.15}$$

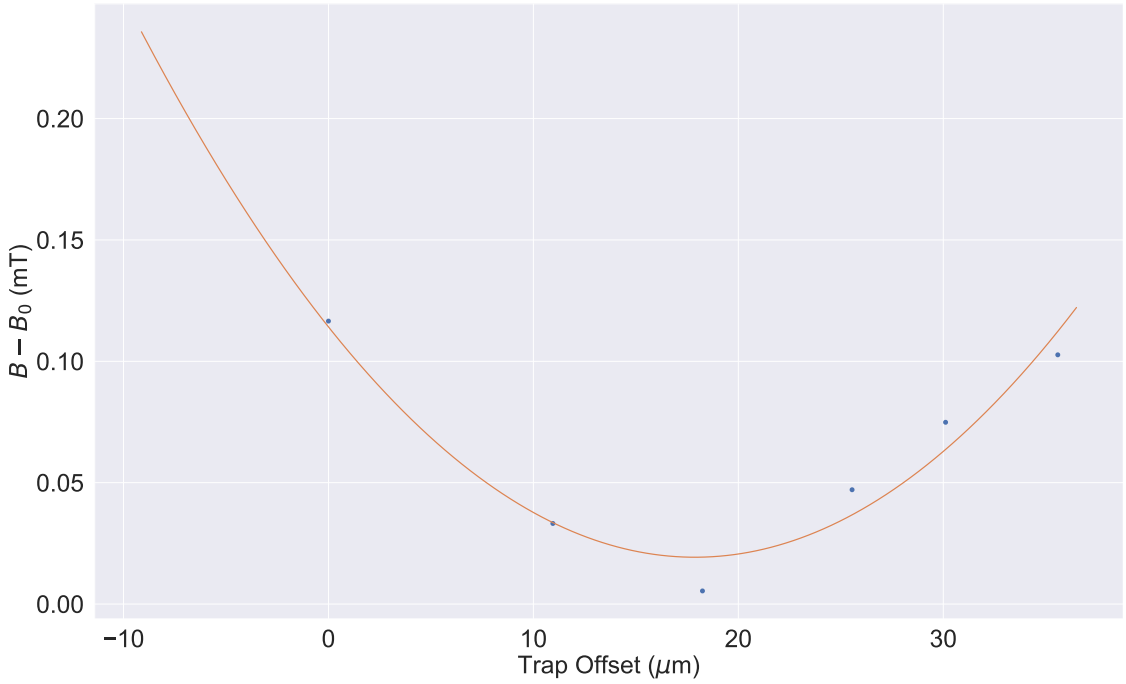

Figure 6.8: $B_{2,AT}$ is measured by introducing an offset to the trapping potential, shifting particle's center of motion, $\langle z \rangle$. The modified cyclotron frequency is then measured as in Fig. 6.7 at the offset position.

6.4 PT Resonator Temperature

The main result highlighted in this thesis is, of course, the demonstration of sympathetic cooling of a proton. However, since the proton is cooled via a sympathetically cooled LC circuit, we only measure the temperature of the LC circuit, labeled T_D. In the notation used throughout $T_{z,\mathrm{PT}}$ refers to the thermal temperature of the resonator and $T_D = T_{z,\mathrm{PT}}$ when there is no additional cooling. As a result, the final temperature of the proton and the LC circuit is given by

$$T_p = T_D = T_{z,\mathrm{PT}} - \Delta T_D, \tag{6.16}$$

where ΔT_D is the change in detector temperature and the precision of the final temperature is, to a large part, limited by the precision to which $T_{z,\mathrm{PT}}$ can be measured. Importantly, during the measurement run in which these results were taken the temperature of the axial detection system was significantly higher than the temperature of the cryogenic environment because of increased current noise of the cryogenic amplifier due to stress during thermal cycling. In the end then, we used four independent techniques to measure $T_{z,\mathrm{PT}}$ - measurements of shifts due to $B_2\,T_z$ in two separate traps and two measurements of frequency shifts due to $C_4\,T_z$.

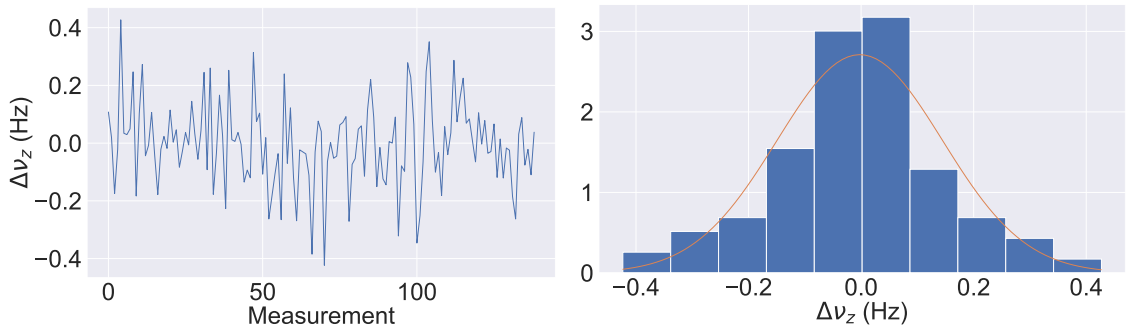

(a) (b)

Figure 6.9: A measurement of the axial frequency scatter induced by coupling to the cyclotron mode at T_+ with the fit to the data yields $\sigma(\Delta\nu_z) = 147\,\text{mHz}$ and an axial temperature of around 20 K.

6.4.1 B_2 Method

The B_2 shift of the axial frequency,

$$\Delta\nu_z = \frac{1}{4\pi^2 m\nu_z}\frac{B_2}{B_0}\left(E_+ + |E_-|\right), \tag{6.17}$$

is the most straightforward method of determining the temperature of the resonator. In such a measurement the axial mode is coupled to a radial mode with a sideband drive at $\omega_{\text{SB}\pm} = \omega_\pm \mp \omega_z$ with the resulting radial mode energy, $E_\pm = E_z\omega_\pm/\omega_z$. Repeated couplings and measurements of $\Delta\nu_z(E_\pm, B_2)$ will be Boltzmann distributed at $T_\pm$ and the axial temperature is given by

$$T_z = \langle\nu_z\rangle/\langle\nu_\pm\rangle T_\pm. \tag{6.18}$$

Here $\langle\nu_z\rangle$ indicates the mean frequency during the measurement (in practice, the frequencies can often be assumed to be fixed as the drift is much smaller than the measurement resolution).

When measured in the PT the modified cyclotron sideband, $\omega_{\text{SB}+} = \omega_+ - \omega_z$, is typically used as it produces the largest shifts. The results of a measurement performed in the PT, $T_{z,\text{PT}}$ are shown in Fig. 6.9.

with the result that

$$\begin{aligned} T_+ &= (1210 \pm 0.042)\,\text{K}, \\ T_{z,\text{PT}} &= (20.0 \pm 5.6)\,\text{K}, \end{aligned} \tag{6.19}$$

and the error is dominated by the uncertainty in $B_{2,PT}$.

The same measurement can also be performed by reading out the axial frequency shift in the AT, utilizing the much stronger B_2. In this measurement,

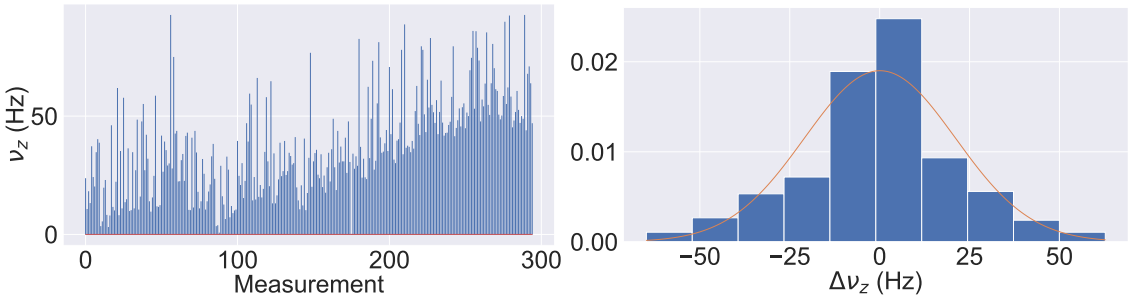

(a) (b)

Figure 6.10: **(a)** The axial frequency is measured in the AT after the cyclotron mode is coupled to the axial detection system. **(b)** The width of the resulting distribution gives the temperature of the radial modes and consequently the temperature of the axial detection system - see text for details.

the magnetron sideband is applied in the PT and the particle is transported to the AT. The distribution of axial frequency shifts is a convolution of the Boltzmann distributed energy shift and a Gaussian distributed random walk arising from additional axial frequency instability in the AT (see Sections 2.2.2 and 3.1). Using the data from the measurement shown in Fig. 6.10, the resulting temperature is found to be

$$\begin{aligned} T_- &= (0.292 \pm 0.042)\,\mathrm{K}, \\ T_{z,\mathrm{PT}} &= (17.2 \pm 2.4)\,\mathrm{K}, \end{aligned} \tag{6.20}$$

and again the error is given by the precision to which $B_{2,\mathrm{AT}}$ was measured.

6.4.2 Feedback Method

The temperature of the axial detection system can also be obtained by adjusting the effective temperature with feedback. Described in Section 3.3.2, feedback changes the Q-value of the detector and allows the temperature to be written as,

$$\frac{T_{\mathrm{FB}}}{T_0} = \frac{\gamma_{\mathrm{FB}}}{\gamma_0}. \tag{6.21}$$

Here T_0, γ_0 and T_{FB}, γ_{FB} are the temperature and dip width of the proton without and with feedback, respectively. We again adjust the TR at each feedback setting and measure the quantity $\frac{\partial \Delta\nu_z}{\partial \mathrm{TR}}$. $\Delta\nu_z$ is given by Eq. (3.22) and can be expressed as

$$\Delta\nu_z = \frac{1}{4\pi^2 m \nu_z} \frac{6}{4} \frac{D_4}{C_2}\, k_B\, T_z\, \Delta\mathrm{TR}. \tag{6.22}$$

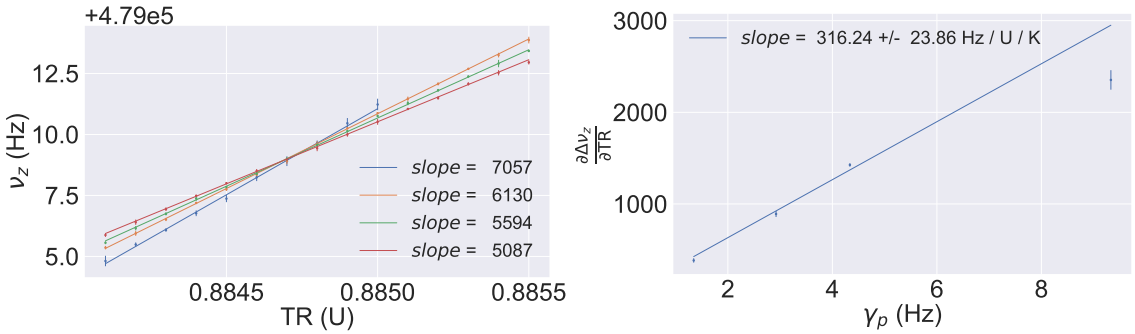

(a) (b)

Figure 6.11: **(a)** Individual measurements of $\Delta\nu_z(\mathrm{TR})$ are shown that depend on the temperature of the resonator. **(b)** These measurements can be combined to extract $\frac{\partial\Delta\nu_z}{\partial\mathrm{TR}}$ where the slope gives the axial temperature for a given κ_{D_4} and the y-intercept gives D_2 - see text for details.

D_4 is determined by the trap geometry and calculated to be $D_4 = 1.28 \times 10^9\,\mathrm{m}^{-4}$ to a precision of a few percent set by electrode tolerances during machining. Using the notation of Section 3.1.2, κ_{D_4} is defined as

$$\kappa_{D_4} = \frac{1}{4\pi^2 m\nu_z}\frac{6}{4}\frac{D_4}{C_2} = 45.4\,\mathrm{mHz/(mU\,K)} \tag{6.23}$$

and, as illustrated in Fig. 6.11, measuring the TR derivative of Eq. (6.22) allows the temperature to be extracted by,

$$\frac{\partial\Delta\nu_z}{\partial\mathrm{TR}} = D_2 + \kappa_{D_4}T. \tag{6.24}$$

With this method we ultimately find

$$T_{z,\mathrm{PT}} = (19 \pm 1.4)\,\mathrm{K}. \tag{6.25}$$

Notably, this method is very similar to the one used to measure the temperature of the sympathetically cooled proton and plays an important role in the measurements of Chapter 9.

6.4.3 Lineshape Method

Finally, just as the ideal tuning ratio can be found by maximizing the dip SNR, the scaling $\frac{d\mathrm{SNR}}{d\mathrm{TR}}$ can be used to find the temperature of the axial detection system. The complete lineshape of the particle-resonator system is given by the real part of the impedance of the resonator RLC circuit and the equivalent LC circuit of the particle [74],

$$S(\nu) = n_0 + n_1\frac{x_1^2}{x_1^2 + (x_1x_0 - 1)^2}. \tag{6.26}$$

Here the parameters x_0 and x_1, along with scaling parameters n_0 and n_1, describe the resonant behavior of the particle and axial detector respectively, by,

$$x_i(\nu) = \frac{2(\nu - \nu_i)}{\Delta\nu_i}. \tag{6.27}$$

However the axial frequency is additionally shifted by $k_{D_4} T_z$ and appears "smeared out" due to FFT averaging. The real lineshape is found by taking the convolution of Eq. (6.26) with the Boltzmann distributed frequency shifts,

$$\chi(\nu) = \int_0^\infty S(\nu) \star \frac{1}{k_{D_4}\,\Delta\mathrm{TR}\,T_z} e^{-T/Tz}\, dT. \tag{6.28}$$

With the FFT spectrum measured in units of dBV,

$$\mathrm{SNR}(\mathrm{TR}) = S_{\mathrm{ref}} - 20\log_{10}\chi\left(\nu_0 + k_{D_4}\,\Delta\mathrm{TR}\,T_z\right), \tag{6.29}$$

where S_{ref} is the reference level of the detector. The measured SNRs as a function of tuning ratio can be fit with Eq. (6.29) to extract T_z. In fact, we measure this at multiple points during the course of a measurement campaign to confirm that the noise temperature remains constant and find

$$T_{z,\mathrm{PT}} = (17.27 \pm 1.2)\,\mathrm{K}, \tag{6.30}$$

by taking the weighted average of the measurements shown in Fig. 6.12.

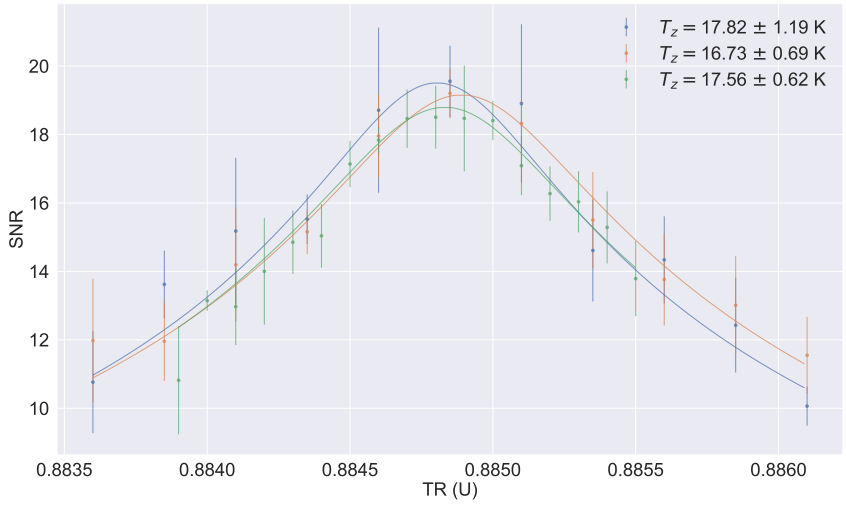

Figure 6.12: The measured dip SNRs are shown at different tuning ratios along with curves corresponding to axial resonator temperatures.

6.4.4 Axial Temperature Summary

Again, as the temperature of the sympathetically cooled proton is largely dependent on the temperature of the axial detection system considerable effort was put

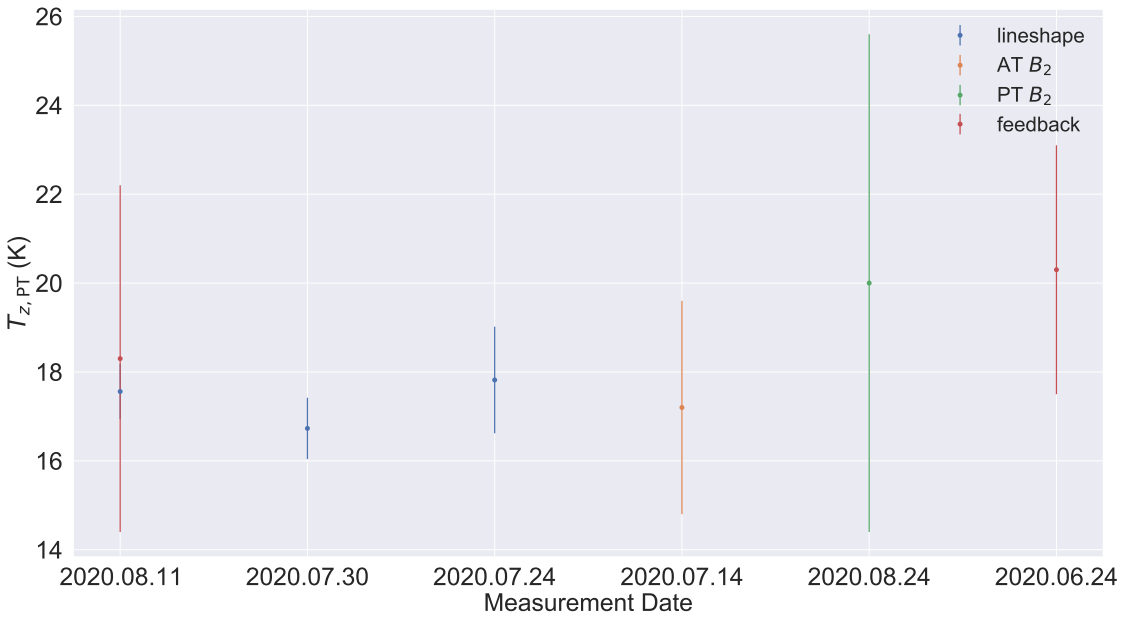

Figure 6.13: $T_{z,\mathrm{PT}}$ is measured with different methods throughout a measurement campaign. The agreement between the measurements provides assurance that the value we set is consistent and does not vary with time.

into understanding each method and confirming that all agree. The results of this analysis are summarized in Table 12.2 and Fig. 6.13 with the resulting temperature given as

$$T_{z,\mathrm{PT}} = (17.36 \pm 0.42)\,\mathrm{K}, \tag{6.31}$$

where $T_{z,\mathrm{PT}}$ is the weighted mean of the measurements in Table 12.2. The feedback method relies on a measured $\partial\Delta\nu_z/\partial\mathrm{TR}$ value, which is exactly what is measured with laser cooling. As a result, while the error on $T_{z,\mathrm{PT}}$ shown here is taken from the weighted mean of all the measurements in Table 12.2 while the measurements shown in Chapter 9 use the errors on the feedback method to account for additional uncertainty in the measurement routine.

Date	Method	T_z (K)	σ_{T_z} (K)
2020.08.11	Lineshape	17.56 K	0.62 K
2020.07.30	Lineshape	16.73 K	0.69 K
2020.07.24	Lineshape	17.82 K	1.2 K
2020.07.14	AT B_2	17.2 K	2.4 K
2020.08.24	PT B_2	20.0 K	5.6 K
2020.06.24	Feedback	20.3 K	2.8 K
2020.08.11	Feedback	18.3 K	3.9 K

Table 6.1: Summary of temperature measurements used to determine $T_{z,\mathrm{PT}}$. All methods agree and produce consistent results of a large period of time.

Chapter 7

Heating Rates

A discussion of cold, trapped particles necessarily includes heating rates. To first order, Penning traps have no driven motion and do not suffer from the "anomalous heating" present in rf traps [75, 76]. In fact, the BASE group at CERN recently observed the lowest reported heating rates of a single motional mode during a long measurement of the cyclotron energy of a single antiproton [77]. Nevertheless, these experiments are not immune to unwanted motional heating effects and this chapter aims to discuss those present in the proton g-factor experiment. First, as in [77], we observe low heating rates of the proton during transport from the PT to the AT, consistent with the predictions of Eq. (3.60). With beryllium however, unexpected heating rates arise while transporting ions to the AT. With these heating rates beryllium ions proved to be very challenging to work with and were the focus of significant experimental effort. In fact, a limiting factor in the beryllium temperature measurements performed in the magnetic bottle, as discussed in Chapter 8, is the unexpected heating described here. Interestingly, we have found that this is consistent with the phenomenon of resonantly enhanced transition probabilities due to degenerate energy levels. Such phenomena is well documented in other systems but has remained unexplored in Penning traps[1]. Finally, a characterization of the trap anharmonicities follows and problems arising from charges introduced by the cooling laser and by the ion loading procedure are discussed.

While limiting for temperature measurements involving transporting cold beryllium ions, the low observed heating rates are very promising. Together with the results from the CERN group, they suggest that in future experiments protons can be prepared with sympathetic cooling to the milli-Kelvin level and transported to the AT with no change in motional quantum numbers.

[1] Additional details can be found in [65]

7.1 Proton Heating Rates

As a highly sensitive "particle thermometer" the AT can be used to measure heating of the modified cyclotron mode via the continuous Stern-Gerlach effect - see Eq. (3.54). With $\nu_z(n_{+,i}) - \nu_z(n_{+,i+1}) \approx 74\,\text{mHz}$, dn_+/dt can be measured simply by tracking the axial frequency. However, during the measurements of this thesis, most protons were prepared with sideband coupling, resulting in subsequently large cyclotron energies. As a result, the energy stability, and thus axial frequency stability, is not competitive with [77]. Nevertheless, the stability shown in Fig. 7.1 is sufficient to enable high precision temperature measurements in the magnetic bottle.

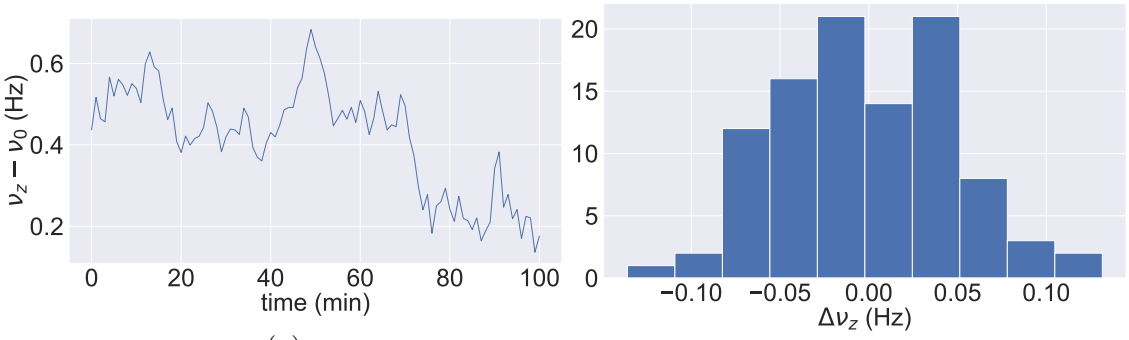

(a) (b)

Figure 7.1: **(a)** Axial frequency measurements in the AT and **(b)** the resulting axial frequency jitter, $\Delta\nu_z = \nu_{z,n} - \nu_{z,n-1}$. During these measurements $E_+/k_\text{B} < 5\,\text{K}$ and the distribution of axial frequencies is expected to narrow at lower energies.

Following [30], the axial frequency stability in the AT is composed of two components: white noise arising from fit uncertainty and (to a lesser extent) voltage instability, denoted Δ_s and the random walk of the cyclotron energy described by Eq. (3.60), denoted Δ_w. The axial frequency stability as a function of averaging and waiting time, t, can then be written as,

$$\langle \Delta\nu_z \rangle = \sqrt{\Delta_n^2(t) + \Delta_w^2(t)}. \tag{7.1}$$

For a given averaging time of 60 s, used during a g-factor measurement, the axial frequency stability scales with the cyclotron energy E_+, and is described experimentally by,

$$\langle \Delta\nu_z \rangle = \sqrt{a + b\,E_+/k_\text{B}}. \tag{7.2}$$

Here a, b are found to be $(0.055\,\text{Hz}^2$ and $(0.095\,\text{Hz/K})^2$. As a result, the measurement shown in Fig. 7.1 is consistent with Eqs. (7.1) and (7.2) and is both sufficiently low for a g-factor measurement and expected to decrease with lower radial energies.

Importantly though, we do not observe significant heating of the cyclotron mode due to transport. During a measurement in which the proton is repeatedly transported from the PT to the AT, the jitter of the radial energy is around 20 mK -

shown in Fig. 7.2. This is consistent with the predictions of Eq. (7.2) and indicates that axial frequency scatter is not induced by the transport.

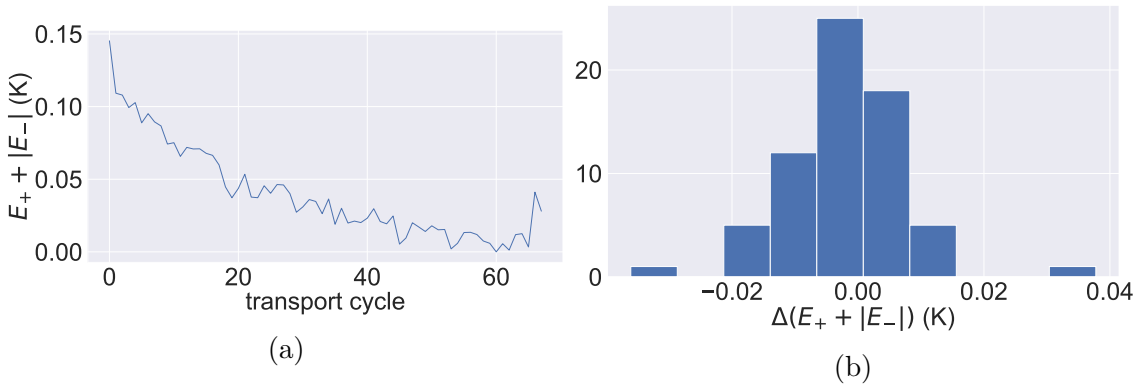

(a) (b)

Figure 7.2: **(a)** The radial energy of the proton is shown during a series of transport measurements referenced to the lowest measured radial energy. Although subject to a long term drift not present in the measurement of Fig. 7.1, the resulting distribution shown in **(b)** is consistent with the the expectations from [77], and expected to decrease with lower radial energies.

7.2 Beryllium Heating

With beryllium ions however, transporting into the AT poses a significant challenge - in particular making some of the measurements shown in the following chapter extremely difficult. During a typical transport sequence the maximum voltage of the voltage supplies, $V_T = -14\,\mathrm{V}$, is applied to two neighboring electrodes and the particle is transported by raising the potential of a following electrode while simultaneously lowering the potential of the previous electrode. However, unlike with protons, beryllium ions are subject to very large heating rates using this maximum voltage. Following a measurement campaign to optimize the transport routine, Fig. 7.4 shows the scatter of the axial frequency, and thus the change in radial energy, as a function of transport voltage V_T. There is a clear minimum around $V_T \approx -6.5\,\mathrm{V}$ and all the following measurements are conducted at this setting. However, note that the points shown in Fig. 7.4 should be considered a lower bound only. The axial frequency and ring voltage were found with a parametric excitation with limited resolution. Further measurements used dip detection to optimize further but the $-6.5\,\mathrm{V}$ setting remained unchanged.

In fact, the heating of the beryllium ions is, in some sense worse than simple transport induced heating. While remaining in the AT we observe heating of a single beryllium ion while ramping the ring voltage from $V_r = -6.5\,\mathrm{V} \rightarrow -6.0\,\mathrm{V}$, shown in Fig. 7.6. In the magnetic bottle, the magnetic field drops from $B_0 \approx 1.98\,\mathrm{T}$ to $B_0 \approx 1.18\,\mathrm{T}$. The resulting reduction of the cyclotron frequency causes the already

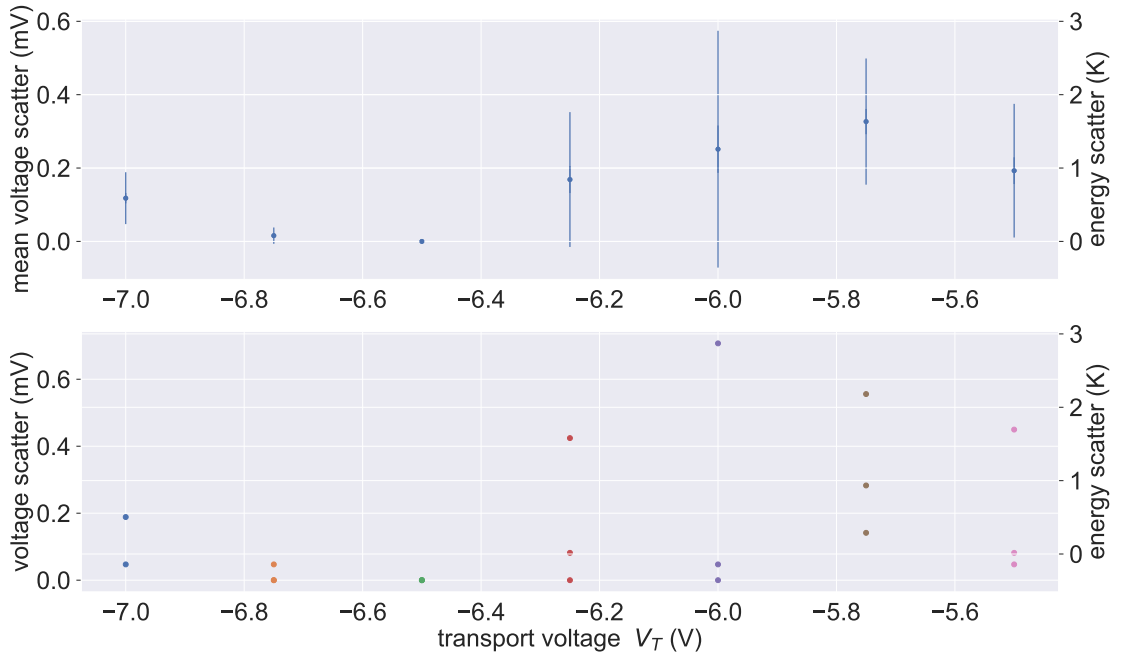

Figure 7.3: During a transport sequence the beryllium ion is heated when the trap frequencies are swept over a resonance point that enhances transition rates between the modes. Temperature measurements were ultimately performed at a transport voltage of $-6.5\,\mathrm{V}$ - see text for details.

small spacing of the trap frequencies to become even smaller. As a result, resonances can occur at certain values of the axial frequency. For example, when the ring voltage is set near $V_r \approx -6.2\,\mathrm{V}$, the trap frequencies can be written as

$$m\,\nu_- = \nu_z = \frac{1}{2m}\nu_+. \tag{7.3}$$

Here m is an integer and in this particular case $m = 3$. Illustrated in Fig. 7.5, when the trap frequencies can be described by Eq. (7.3), the energy eigenmodes of the trap motion are degenerate. Coupling between the modes, which is especially strong in the magnetic bottle, then allows energy to be exchanged. Transitions between the modes are resonantly enhanced by these degeneracies as in other atomic or nuclear systems. For example, this phenomenon is similar to neutrinoless double beta decay experiments in which mass degeneracies in two atoms enhance the probability of nuclear transitions [78]. We also observe increased scatter during a downward ramp of the ring voltage over the $m = 4$ resonance point. Ultimately, ramping over such instability points or resonances during a transport sequence is unavoidable due to monotonic changes of the radial frequencies during the transition region $B_{0,\mathrm{PT}} \rightarrow B_{0,\mathrm{AT}}$. With 50 and 20 data points respectively, we assign an average scatter of the radial energy due to transport of

$$\Delta E_{\pm,\mathrm{transport}}/k_\mathrm{B} = (2.2 \pm 0.2)\,\mathrm{K} \tag{7.4}$$

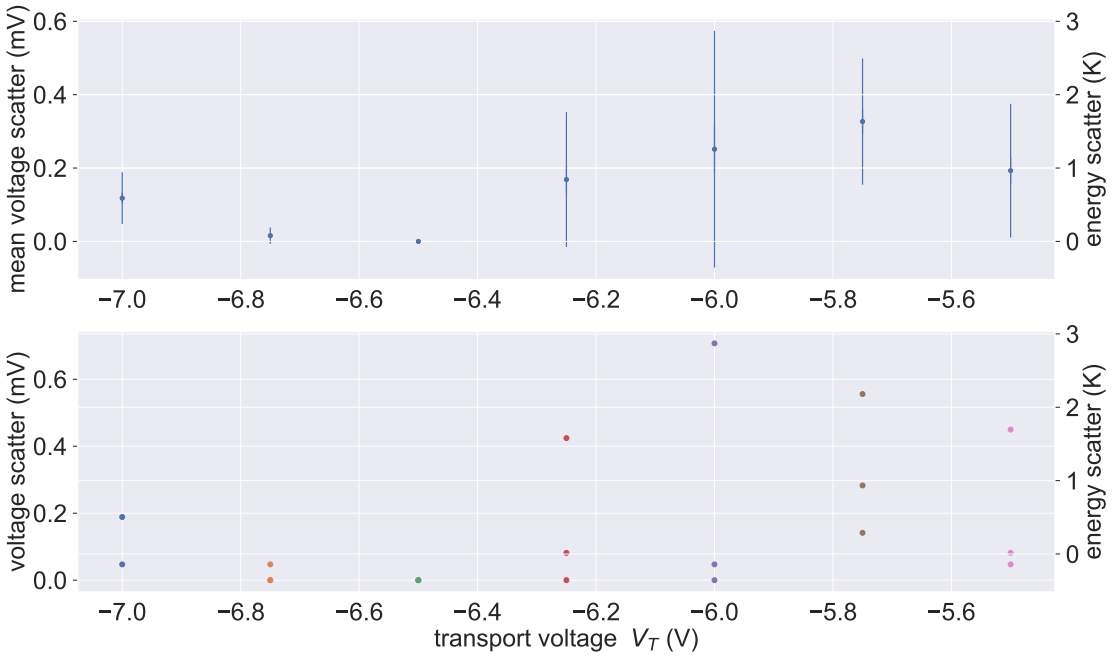

Figure 7.4: During a transport sequence the particle is stored in two electrodes which are subsequently ramped to move the particle along the trap stack. See text for details.

and an average scatter of the radial energy due to ring voltage ramps of,

$$\Delta E_{\pm,\mathrm{ramp}}/k_\mathrm{B} = (0.99 \pm 0.14)\,\mathrm{K}. \tag{7.5}$$

As a result, even with optimization significant heating rates remain and make magnetic bottle temperature measurements with beryllium ions a significant challenge.

In the future this limitation could be overcome by raising the magnetic field up to 7 T, which is possible in the existing superconducting magnet or by conducting temperature measurements in a weaker magnetic bottle. In addition, better alignment of the trap axis with the magnetic field, as will be done during the next assembly of the apparatus, is expected to reduce these heating rates with no additional modifications.

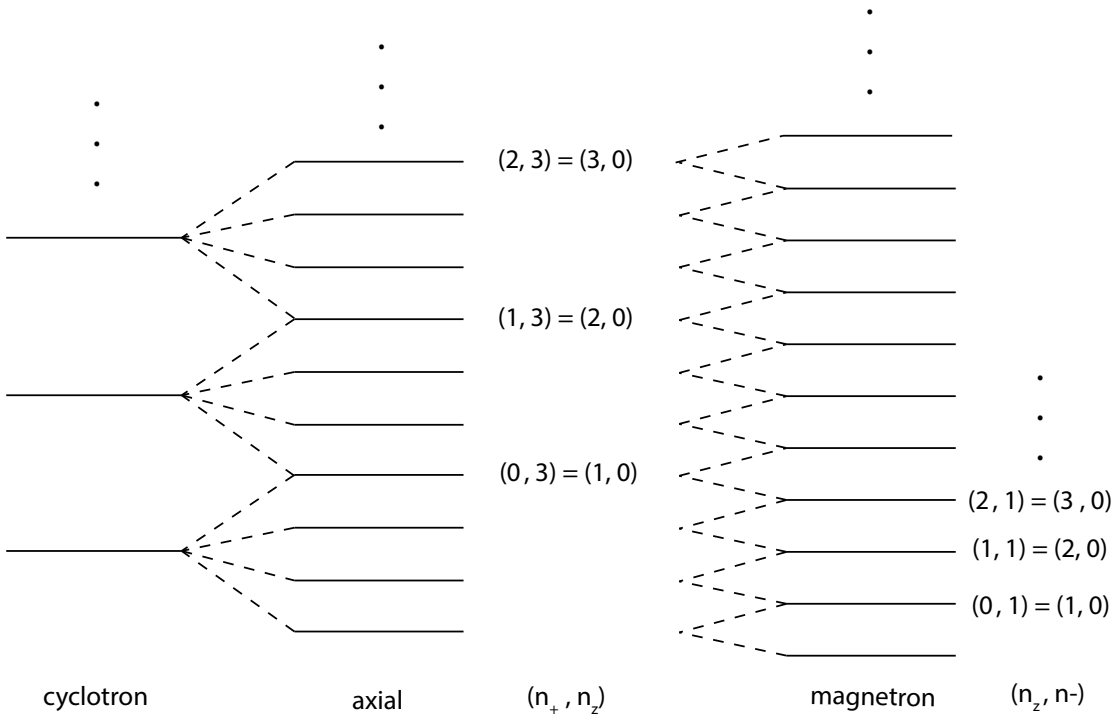

Figure 7.5: At resonance points, all trap frequencies are integer multiples of each other and lead to degeneracies of the trap eigenmodes, see Eq. (7.3). Shown here is the $m = 4$ case in which $(n_{+,i}, n_{z,0}) = (n_{+,i+1}, n_{z,3})$ and similarly, $(n_{z,i}, n_{-,0}) = (n_{z,i+1}, n_{z,1})$. Here n_+, n_z, n_- are the quantum numbers of the modified cyclotron, axial, and magnetron mode, respectively. See text for details.

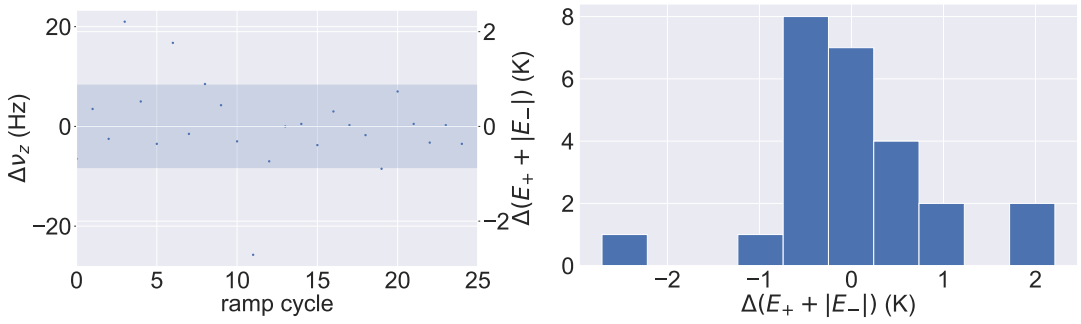

(a) (b)

Figure 7.6: Axial frequency, and thus radial energy $\Delta(E_+ + |E_-|)$, during a ramp of the ring voltage, $V_r = -6.5\,\mathrm{V} \to -6.0\,\mathrm{V}$. Changes in the radial energy are believed to come from instability points where trap frequencies are in resonance, enabling energy exchange between the modes. See text for details.

7.3 Induced Charges

While not necessarily a form of heating, the introduction of semi-permanent charges onto surfaces near the traps presents similar challenges and should be discussed in the same context. It is well documented, for example in [79, 80, 81], that bare charges can appear on trap surfaces when exposed to scattered UV light and distort the trapping potential. In these measurements, performed in rf traps, this distortion results directly in larger heating rates in the form of increased micromotion. In our case, when induced charges are present the trapping potential is distorted and shifted from the geometric center. This then necessitates asymmetry compensation as in Eq. (3.26), and reduces the signal-to-noise ratio of the dip spectrum through additional, uncorrected modifications to the trap potential. In fact, we observe induced charges from three sources: the cooling laser at 313 nm, the ablation loading procedure, and the use of the electron gun - each of which creates free electrons or ions that can attach to frozen out residual gas. An example of the shift in trapping potential due to this effect is shown in Fig. 7.7, where the ring voltage of the ST is shown and a large $\sim 0.5\,\mathrm{V}$ shift appears after many days of operation with the cooling laser and repeated loading cycles. In fact, after this large shift appeared the trap became essentially inoperable, with low dip resolution and large trap frequency drifts. However, with careful alignment of the cooling laser and judicious use of the ablation laser, these induced charges can be largely avoided and trap operation can in principle continue indefinitely. Once introduced though, these charges remain until the apparatus is warmed up to room temperature and are neutralized by collisions with background gas.

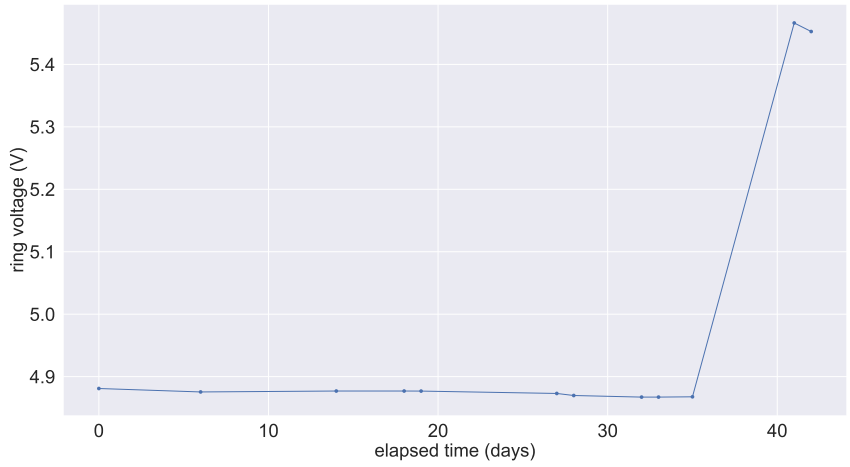

Figure 7.7: An example of shifts to the trapping potential that can arise from induced charges onto trap surfaces is given. After more than a month of operation, repeated loading cycles introduced a large shift of the trapping potential, and thus ring voltage.

While fairly noncontroversial and a well-known phenomenon, this effect was a source of considerable difficulty in the early days of commissioning the new

apparatus. With the largest shifts coming from the ablation laser, we at first considered the idea that the ablation laser was coating the trap electrodes with a layer of neutral beryllium that produced patch potentials. However, this idea was rejected after observing the electrodes in question under a microscope and seeing no discoloration or visible coating. In a later run, we also observed that warming up the apparatus to room temperature and cooling down again with no further modifications was sufficient to restore the original trapping potentials. As a final note, it should be mentioned that this effect had a significant impact on the design and construction of the experimental apparatus used for all following measurements. The design shown in Fig. 5.1 and the top of Fig. 7.8 was modified, and the ST was moved away from the AT and placed in between the ablation ion source and the coupling traps. In this configuration, the ST acts as a buffer region, adding distance between a "dirty" production region and a "clean" coupling region. Luckily, this design also enabled the measurements presented in Chapter 9, in which coupling and cooling between ions in two separate traps was demonstrated.

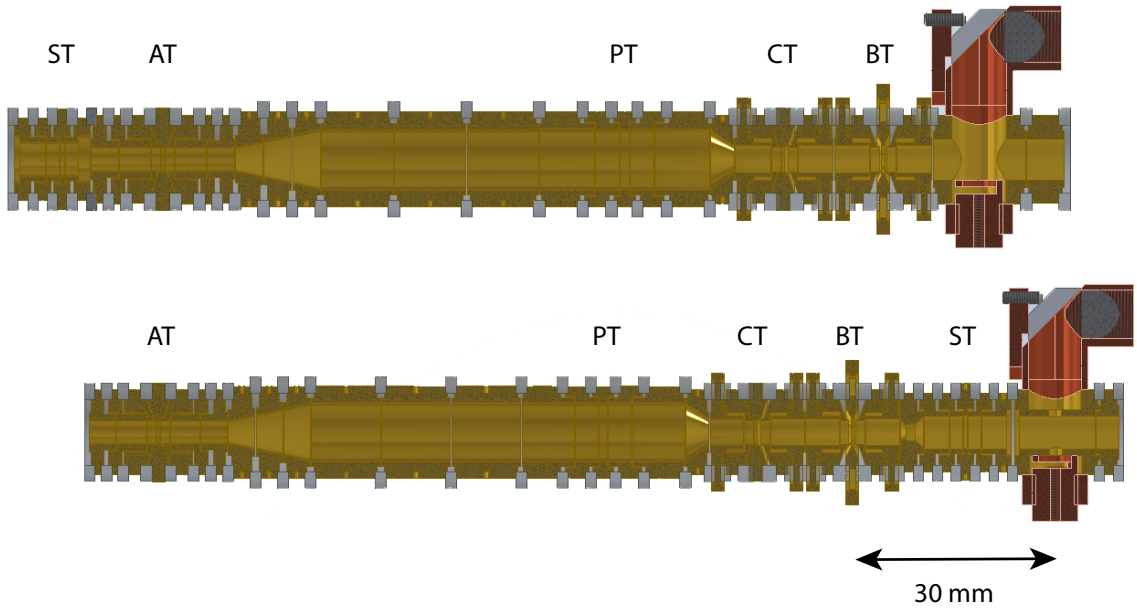

Figure 7.8: The trap apparatus was modified to place the ST between the loading region and the ablation ion source. The buffer region proved valuable in preventing the coupling traps from charging up. The results of the following chapters were conducted in the new configuration.

Chapter 8

Laser Cooling of Beryllium Ions

After much work to set up and characterize the new apparatus, a significant initial success was the demonstration of laser cooling of beryllium ions. With the correct theoretical understanding of Doppler cooling in the large magnetic field, this observation proved to be relatively straightforward, with many ways to observe reduced beryllium temperatures. Some of the first signals observed were frequency shifts due to κ_{C_4}, κ_{B_2} and the reduced radial energy. While cooling, the characteristic dip spectrum changes and provides a clear signal. We then went on to measure resulting temperature of the beryllium ions using both a magnetic bottle temperature measurement and the observed fluorescence spectrum.

8.1 Theoretical Treatment

Although laser cooling in ion traps is a common and well-established technique [32, 42], the presence of the large magnetic field is a complicating factor. In this chapter, familiarity with the basic principles of Doppler cooling is assumed, although a full treatment of the repumping scheme and the level splittings unique to our system is presented here. Fig. 8.1 shows the relevant energy levels of $^9Be^+$ in the 1.98 T magnetic field. At such large field strength the splitting of the atomic energy levels can be described by the Paschen-Back effect - the high field limit of the Zeeman effect where the spin-orbit coupling is broken by the external magnetic field. In this limit, the good quantum numbers are m_l and m_s, the magnetic and spin quantum numbers, respectively. Be^+, a lithium-like ion with a single valence electron, has atomic energy levels (denoted here E_a to distinguish from axial energy E_z) given by,

$$E_a = E_0 + B_0\,\mu_B\,(m_l + g_s\,m_s)\,. \tag{8.1}$$

Here E_0 is the unperturbed transition energy, μ_B is the Bohr magneton, and valence electron has Landé g-factor, g_s. Illustrated again in Fig. 8.1, Doppler cooling

is performed on the strong dipole allowed $^2S_{1/2} \rightarrow {}^2P_{3/2}$ transition with natural linedwith $\Gamma = 19.6\,\mathrm{MHz}$ [82]. In our case we cool mainly on the $|m_{I,0}, m_{J,0}\rangle \rightarrow |m_{I,1}, m_{J,1}\rangle = |-3/2, -1/2\rangle \rightarrow |-3/2, -3/2\rangle$ transition, where $m_{I,1}$, $m_{J,1}$ are the nuclear and electronic spin quantum numbers and 0,1 denote the ground and excited states, respectively. We have also observed cooling on the equivalent $|+3/2, +1/2\rangle \rightarrow |+3/2, +3/2\rangle$ transition, with identical behavior. Rather uniquely, Be^+, along with Mg^+, can be cooled using a single laser, relying on a rempumping scheme first described in Refs. [83, 84]. Ignoring the nuclear spin quantum number, m_J, selection rules limit the allowed driven transitions to $\Delta m_J = \pm 1$ and $\Delta m_J = 0, \pm 1$ during spontaneous emission. Possible transitions are shown in Fig. 8.1, with a dark state at $m_J = +1/2$. In experiments that require high fidelity state preparation, e.g. in [8], a second laser a few hundred GHz away can be used to repump ions in the dark state back into the cooling cycle. However, off resonant transitions driven by the cooling laser can also be used to preferentially bring the ion back into the cooling cycle. By using σ^- polarized light (again, in the case of driving the $|-3/2, -1/2\rangle \rightarrow |-3/2, -3/2\rangle$ transition), the transition that populates the $m_J = +1/2$ dark state is doubly disfavored - it can only be driven off resonantly and only with opposite polarization. On the other hand, the transition from the $m_J = +1/2$ dark state to the $m_J = -1/2$ excited state is only singly disfavored, as the transition is preferentially driven with σ^- polarized light. From the $m_J = -3/2$ excited state spontaneous emission brings the ion back to either ground state, again shown in Fig. 8.1.

Quantitatively, the population of the dark state can be found by taking the ratio

$$P_d = \frac{\rho\left(\delta_0\right)}{\rho\left(\delta_{\mathrm{off}}\right)}, \tag{8.2}$$

where δ_0, δ_{off} are the detunings of the cooling laser from the $m_J = -1/2 \rightarrow m_J = +1/2$ and $m_J = +1/2 \rightarrow m_J = -1/2$ states, respectively, and the transition rate $\rho(\delta)$ is given by [42],

$$\rho(\delta) = \Gamma \frac{S/2}{1 + S + (2\delta/\Gamma)^2}. \tag{8.3}$$

Here Γ is the natural linewidth of the $S_{1/2} \rightarrow P_{3/2}$ transition and S is the saturation parameter, assumed to be 1. Using the the values in Table 8.1, we estimate a dark state population of

$$P_d \approx 1/10, \tag{8.4}$$

for unpolarized light, and an average dark state occupation time of

$$t_{\mathrm{dark}} = 0.69\,\mathrm{s}. \tag{8.5}$$

This is sufficiently low to enable efficient cooling, even of single ions - albeit complicated by thermalization with the axial detector. With σ^- polarized light the dark state population drops to $P_d \sim 1/19$. In the measurements that follow, faulty polarization optics introduced some difficulty in maintaining the polarization of the cooling laser. As a result, $1/10 < P_{d,\mathrm{exp}} < 1/19$ although uncertainty in intensity

	Zeeman Shift	Function
$-1/2 \rightarrow -3/2$	$\nu_0 + B_0\,\mu_B\,g_{\mathrm{S}_{1/2}} - B_0\,\mu_B\,g_{\mathrm{P}_{3/2}}$	cooling
$+1/2 \rightarrow -1/2$	$\nu_0 - B_0\,\mu_B\,g_{\mathrm{S}_{1/2}} + B_0\,\mu_B\,g_{\mathrm{P}_{3/2}}$	dark state pumping
$-1/2 \rightarrow +1/2$	$\nu_0 + B_0\,\mu_B\,g_{\mathrm{S}_{1/2}} + 2B_0\,\mu_B\,g_{\mathrm{P}_{3/2}}$	cooling cycle pumping
$\Delta(+1/2 \rightarrow -1/2)$	$2B_0\,\mu_B\,g_{\mathrm{S}_{1/2}} - 2B_0\,\mu_B\,g_{\mathrm{P}_{3/2}}$	detuning from cooling laser
$\Delta(-1/2 \rightarrow +1/2)$	$-4B_0\,\mu_B\,g_{\mathrm{P}_{3/2}}$	detuning from cooling laser

Table 8.1: The Zeeman shift terms for the relevant transitions of the beryllium ion in a strong magnetic field are given where ν_0 is the ${}^2S_{1/2} \rightarrow {}^2P_{3/2}$ transition frequency at zero field and no hyperfine splitting. The dark state population is given by the relative detuning of the off resonant pumping into the dark state $\Delta(-1/2 \rightarrow +1/2)$ and the repumping into the cooling cycle $\Delta(+1/2 \rightarrow -1/2)$. See text for details.

and laser detuning during some measurements may have reduced the repumping rates given by Eqs. (8.2) and (8.3).

As a final note Doppler cooling in Penning traps is complicated slightly by the negative energy of the magnetron mode as discussed in [43]. Unless the geometry of the cooling beam is optimized or an additional force, such as a rotating wall, is applied Doppler cooling will increase the magnetron radius. As a result, the majority of the laser cooling shown in the rest of this thesis takes place with the magnetron sideband, $\nu_{rf} = \nu_z + \nu_-$, applied. This thermalizes the magnetron motion with efficiently cooled axial mode and keeps the ions on a constant radius. In the literature this is also referred to as axialization [85, 86].

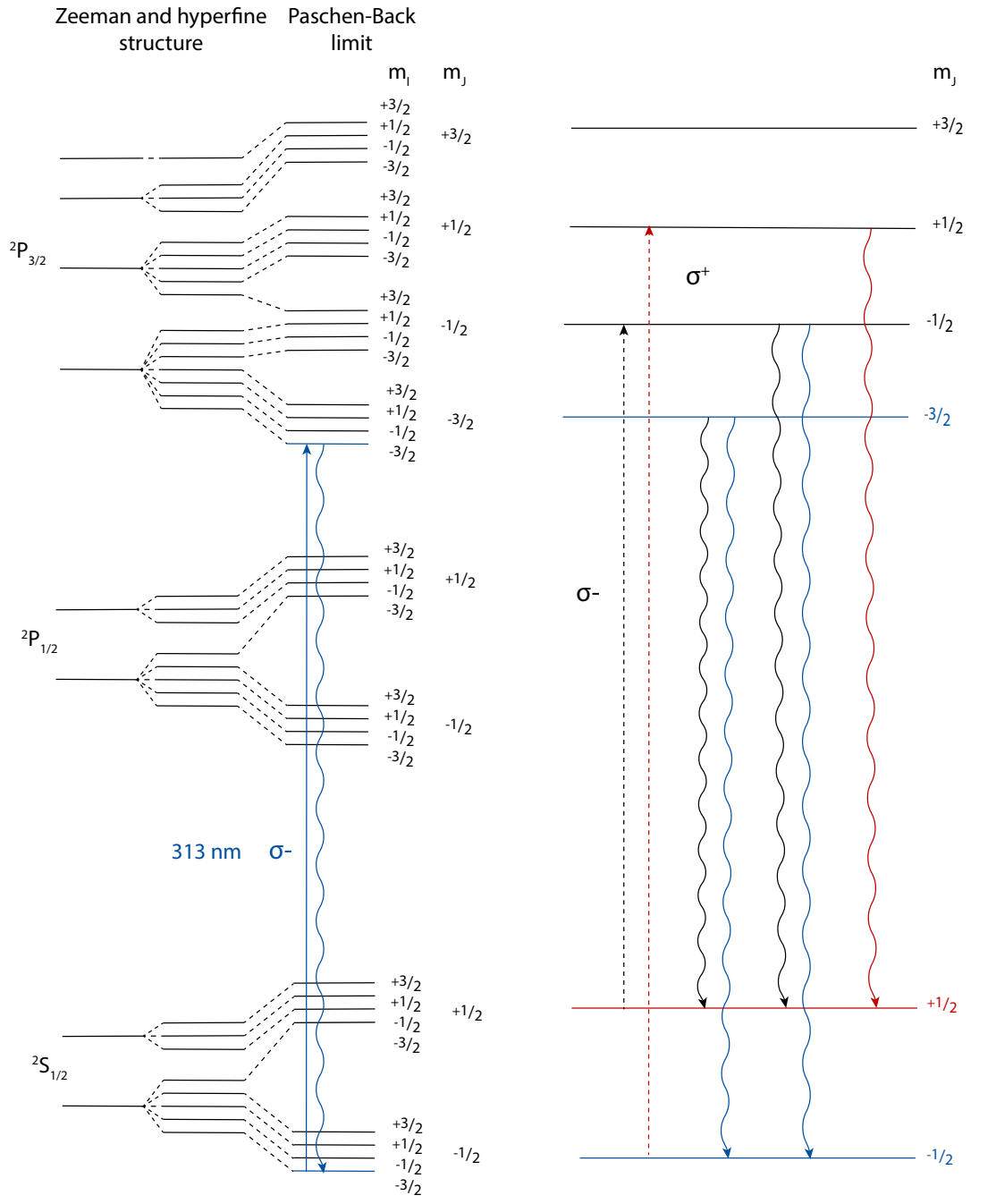

Figure 8.1: Energy levels and splitting of Be^+ in a strong magnetic field (not to scale). The cooling transition from $|m_{I,0}, m_{J,0}\rangle \rightarrow |m_{I,1}, m_{J,0}\rangle = |-3/2, -1/2\rangle \rightarrow |-3/2, -3/2\rangle$ is highlighted in blue while transitions to the dark state are highlighted in red. The repumping scheme described in the text is also illustrated, ignoring the nuclear spin quantum number m_I with the dark state again highlighted in red. The cooling cycle is closed by off resonant transitions that are preferentially driven by σ^- polarized light.

8.2 Image Current Interaction

The first indications of laser-ion interaction were observed with the axial image current detection system. As in Fig. 8.2, the laser can be far detuned, blue detuned, or red detuned from the cooling transition. In the first case, when the laser is far detuned the damping rate of the axial motion due to the photon scattering γ_L is much less than the dip width γ_{Be}, or coupling strength to the detector. As a result the ion is still able to "follow" the thermal noise of the detector i.e. the ion and detector are phase locked and the characteristic dip signal remains. When the laser is blue detuned with respect to the cooling transition however, the axial motion of the trapped particles is excited and appears as a clear peak on the image current detector. As in Fig. 8.2 **(b)**, heating of the radial modes also induces shifts of the axial frequency as described by Eq. (3.54) and Eq. (3.22). Finally and most importantly though, when the laser is near resonance and red detuned to cool the ions, the dip spectrum vanishes. Here, $\gamma_L \gg \gamma_{Be}$, and as a result the ions are no longer phase locked to the noise and do not thermalize at the noise temperature. These dynamics are also described in [87, 88].

This observation was a very important first step in realizing laser cooling in the new experiment. In particular, these first measurements were done before the fluorescence detection had been fully implemented. Moreover, the magnetic bottle measurement shown below relies exactly on the disappearing dip signal while the demonstration of sympathetic cooling in Chapter 9 uses a similar change in the dip-resonator spectrum as an indication of ion cooling.

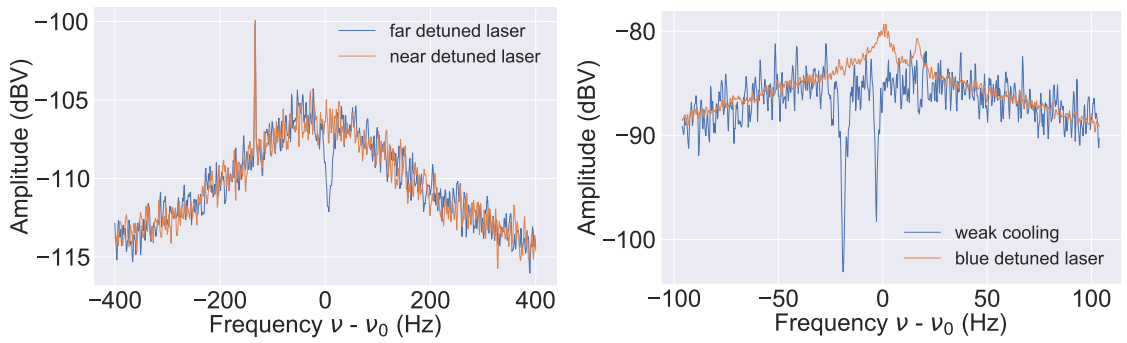

Figure 8.2: **(a)** Shown in blue, when the laser is far detuned from the cooling transition the dip spectrum remains visible. Meanwhile, shown in orange, the dip disappears when the cooling laser is near resonance and the ion is no longer coupled to the resonator. The peak on the left side of the resonator is noise from an axialization drive. **(b)** In a separate measurement the red detuned laser is weakly coupled to the ions resulting in the blue dip spectrum with the double dip due to coupling to the magnetron mode. Shown in orange, when the laser is blue detuned to the cooling transition the ions are heated and, result in a large peak.

8.3 Magnetic Bottle Temperature Measurement

The temperature of laser cooled ions is typically determined by measuring the width of an optical transition, as in, e.g. Refs. [89, 90], although other methods such as resolved sideband spectroscopy [91, 48] or fluorescence imaging [92] are also possible. However, because the proton temperature will ultimately be measured in the magnetic bottle and must remain cold for up to several minutes, an experimental goal was to perform a similar measurement with a beryllium ion while also demonstrating this as a new temperature measurement technique. Ultimately, these experiments had mixed results - while cooling was certainly observed, the measured temperatures were far above the Doppler limit. However, the reasons why are discussed and are readily solvable technical problems which should be overcome in a new apparatus designed for these measurements. Still, the measurement sequence is described here and the major results are presented - constituting the first magnetic bottle temperature measurement with laser cooled ions.

8.3.1 Experimental Sequence

During a measurement, a single beryllium ion is stored in the CT[1] and laser cooled with the disappearance of the dip is a signature of cooling. While laser cooled,

[1]The PT, while a larger and easier to work with trap, required large voltages to trap beryllium at the resonator frequency and was not used.

the axial mode is coupled to the cyclotron mode whose effective temperature can then be read out in the AT using the continuous Stern-Gerlach Effect. Ultimately with a temperature resolution of $\Delta\nu_z/\Delta E_+ k_\mathrm{B} \approx 9\,\mathrm{Hz/K}$, in principle a $\sim 10\,\mathrm{mK}$ level measurement is possible with enough statistics. Described here is the complete measurement sequence for temperature determination in the AT:

1. The trap frequencies are measured in the CT. During the sideband measurement of the cyclotron frequency, the cyclotron mode is thermalized by the axial resonator, again by the relation,

$$T_+ = T_{z,0}\,\nu_+/\nu_z, \tag{8.6}$$

   where $T_{z,0} \approx 6.7\,\mathrm{K}$ is the axial temperature when coupled to the detector.

2. The cooling laser is applied, the axial motion is Doppler cooled, and the dip signal vanishes. While the cyclotron mode will also be cooled by the laser there is no signal indicating that the cooling is successful as with the disappearing dip. As a result, the cyclotron sideband is applied and the resulting temperature is now given by

$$T_{+,L} = T_{z,L}\,\nu_+/\nu_z, \tag{8.7}$$

   where $T_{z,L}$ is the temperature of the axial mode when cooled by the laser. If cooled to the Doppler limit $T_{z,L} \approx 0.5\,\mathrm{mK}$.

3. The ion is now transported from the CT to the AT at $V_T = -6.5\,\mathrm{V}$ to minimize the heating rates described in the previous chapter.

4. The cyclotron energy E_+ is found by measuring the (voltage adjusted) axial frequency, $\nu_z\,(E_+)$.

5. The ion is transported back to the CT and the cycle begins again at Step 1.

Each data point produces a cyclotron energy E_+, or equivalently an axial energy E_z via Eq. (8.7). As in Section 1.2 and Section 1.3 a series of cyclotron energies,

$$S\,(T_+) = \{E_{+,0}, E_{+,1}, ...E_{+,n}\}, \tag{8.8}$$

is Boltzmann distributed and a fit to the data yields the temperature of the laser cooled ion. However, because the dark state population is non-zero and non-negligible, there is a roughly 1 in 10 (or 1 in 19 if σ^- polarized light is used) that the cooling stops when the ion is in the dark state and has begun to heat up by the resonator - illustrated in Fig. 8.3. As a result, $S(T_+)$ is not described by a single Boltzmann distribution of temperature T_+ but by,

$$S(T_+) = S\,(T_{+,L}) + S_\mathrm{dark}. \tag{8.9}$$

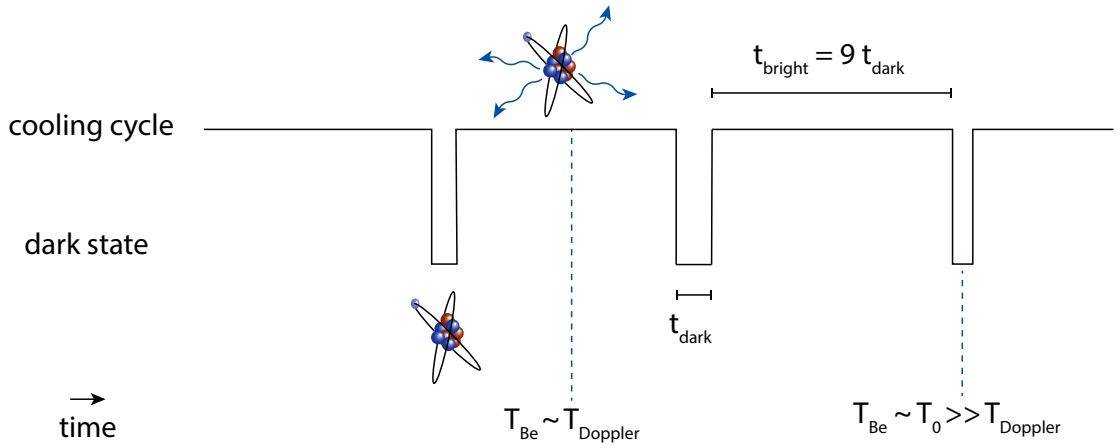

Figure 8.3: During a magnetic bottle temperature measurement the ion occupies the dark state for a time t_{dark}, before rempumping back into the cooling cycle. If the cyclotron mode is coupled during this time, the ion will have an effective temperature T_{dark} and the energy distribution measured in the AT will be only approximately Boltzmann distributed - see text for details.

This distribution S, is then the weighted sum of a Boltzmann distribution $B(T_{+,L})$ arising from the laser cooling and the distribution after leaving the dark state χ_{dark},

$$S\left(T_{+}\right) = B\left(T_{+,L}\right)\left(1 - P_d\right) + \chi_{\mathrm{dark}}\, P_d, \tag{8.10}$$

where the dark state population P_d given by Eq. (8.2) and $T_{+,L}$ is given by Eq. (8.7). In addition, the series $S\left(T_{+,L}\right)$ is on average around nine times longer than $S\left(T_0\right)$, again determined by the dark state population. Unfortunately, all of these parameters are not known a priori due to uncertainty in laser intensity at the ion's position and uncertainty in polarization state after passing through birefringent windows. As a result, we make the simplification that the distributions of both the ion energy measured in the AT, S_+ and the dark state energy S_{dark} are Boltzmann distributed and can be assigned an effective temperature $T_{+,\mathrm{eff}}$ and T_{dark}, respectively.

The effective temperature $T_{+,\mathrm{eff}}$ is a parameter that approximates the probability that a particle is found with energy E_+ by fitting a Boltzmann distribution to S_+. In this way, $T_{+,\mathrm{eff}}$ is found by a maximum likelihood parameter estimation and compared to Monte Carlo simulations with $P_d = 0.1$, $T_{+,L} = 0.5\,\mathrm{K}$, and $T_0 = 15\,\mathrm{K}$, shown in Fig. 8.5. Ultimately, we extract a minimum effective temperature of,

$$T_{+,\mathrm{eff}} = 7.0 \pm 1.0\,\mathrm{K} \tag{8.11}$$

$$T_{z,\mathrm{eff}} = 1.8 \pm 0.3\,\mathrm{K} \tag{8.12}$$

from the measurement shown in Fig. 8.4. This should be compared with temperatures when coupled to the resonator of $T_{+,0} = 26\,\mathrm{K}$ and $T_{z,0} = 6.7\,\mathrm{K}$, showing a reduction by a factor of 3-4. Note that the detector temperature in the ST is measured independently with a magnetic bottle temperature measurement, as described

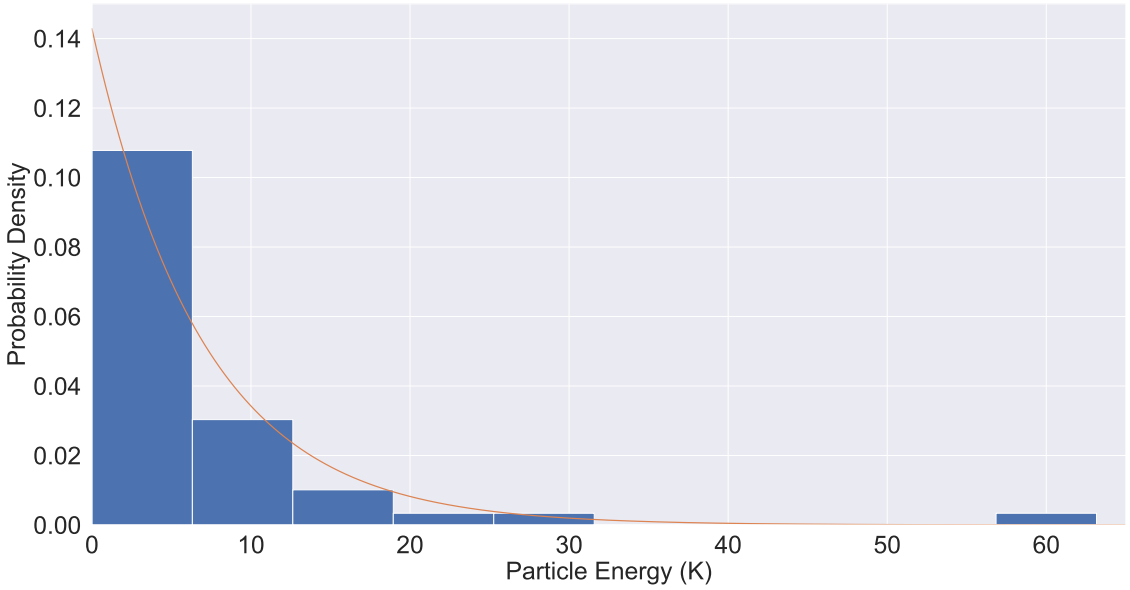

Figure 8.4: The blue histogram shows the cyclotron energy measured in the AT after coupling to the cooled axial mode. The measured data follows the distribution of particle energies measured in the magnetic bottle after laser cooling and coupling to the cyclotron mode. An effective temperature can be extracted of $T_{+,\text{eff}} = 7.0$ and $T_{z,\text{eff}} = 1.8$, with a fit to a Boltzmann distribution with free parameter, T shown in orange. $T_{+,z}$ is limited by the repumping rate out of the dark state and transportation induced heating. See text for details.

for the PT in Chapter 4. In addition to the dark state contributions, the transport heating also contributes to the final temperature and the complete heating effects are summarized in Table 8.2.

It is important to mention that these results should be thought of as a proof-of-principle measurement that can be immediately improved in future versions of the experiment. For example, the transport heating rates can be overcome, as discussed in the previous chapter, while the dark state population can be minimized with improved polarization and intensity control of the laser. Moreover, magnetic bottle temperature measurements improve dramatically when using protons. The transport heating effects are negligible and as the proton can be coupled to multiple ions, the dark state occupation time, t_{dark}, can be ignored. In this case the dark state population only contributes to the final temperature by $T_{\text{z},+} = T_{\text{min}}(1 - P_{\text{dark}})$ where T_{min} is the temperature with zero dark state population.

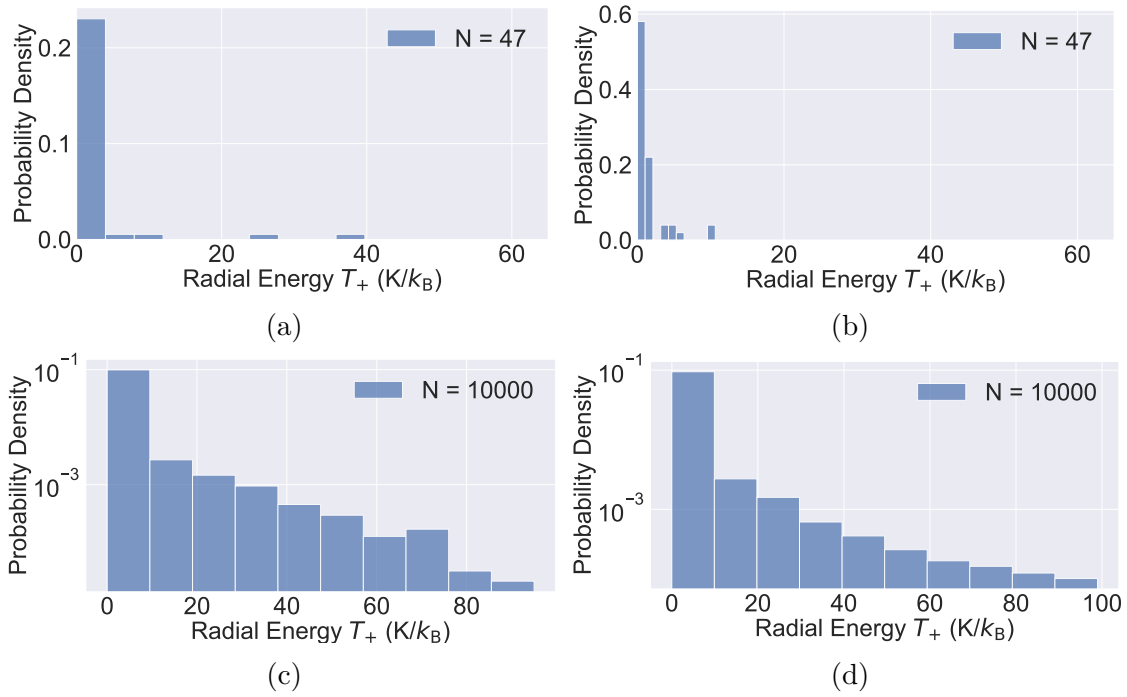

Figure 8.5: Monte Carlo simulations are performed at **(a)** $T_{+,L} = 0.1\,\mathrm{K}$ and **(b)** $T_{+,L} = 1\,\mathrm{K}$ with an equal number of data points as in Fig. 8.4. The full distribution of $N = 10000$ is shown in **(c)** and **(d)**, again for $T_{+,L} = 0.1\,\mathrm{K}$ and **(b)** $T_{+,L} = 1\,\mathrm{K}$. These simulations are illustrative of the distributions expected from Eq. (8.9) and Eq. (8.10) where $T_{\mathrm{dark}} = 15\,\mathrm{K}$ and $P_D = 0.1$. At large N, shown in logarithmic scale, the tail of the distribution is very long and reduces the probability of finding a low-energy particle from the expected laser-cooling distribution.

	Value (K)	Uncertainty (K)	Data Points
Transport Scatter	2.2	0.2	50
AT Ring Voltage Ramp	0.9	0.14	20
Magnetron Scatter	0.7	0.1	50
Minimum Cyclotron Temperature	7.0	1.0	47
Minimum Axial Temperature	1.8	0.3	47

Table 8.2: Summarized here are the heating effects during the magnetic bottle temperature measurement. The transport scatter and scatter induced by the AT ring voltage ramp are described in Chapter 6 and contribute to heating of the radial modes. In addition, scatter is introduced by thermalizing the magnetron mode.

8.4 Fluorescence Detection

One of the most successful measurements during the course of this work was the observation of fluorescence with the newly designed in-situ fluorescence detection system - described in Section 5.3. In fact, these measurements are the first to simultaneously utilize image current detection and fluorescence detection, and are the first to demonstrate fluorescence detection with silicon photomultipliers (SiPMs) in a cryogenic trapped ion experiment. While I designed the first implementation of this system, Markus Wiesinger put in the indispensable work of achieving single photon resolution without which the data shown here could not have been collected. Together we collected this data and further details, including a complete discussion of temperature limits and single photon SiPM operation, will be described in his thesis [65] and an upcoming publication [64].

A limiting factor in the fluorescence detection experiments was scattered background light leading to high background counts. However, with single photon sensitivity the signal can be clearly distinguished, as in Fig. 8.6, by scanning the laser frequency over the resonance. During a typical measurement with around 100 ions, again shown in Fig. 8.6, the laser frequency f_L is modulated at

$$f_L = f_{L,0} + A \sin\left(2\pi \times f_m\, t\right), \tag{8.13}$$

where A is a modulation amplitude of $\sim 150\,\mathrm{MHz}$, f_m is a modulation frequency of $\sim 0.1\,\mathrm{Hz}$. Both $f_{L,0}$ and A are set so that the maximum of f_L is just below the frequency at which the fluorescence signal is maximized. During such a scan, the photon counts and the image current signal are taken simultaneously and the disappearing dip phenomena is readily visible. When fluorescence counts are maximized the dip signal vanishes, while at larger detunings the dip spectrum becomes visible once again. As the a blue detuned laser rapidly heats the ions, the maximum modulation is set below the frequency for maximum cooling and fluorescence to account for jitter of the sinusoidal modulation.

Finally, in a separate measurement in which the laser frequency is swept over the entire resonance, the width of the fluorescence spectra yields a limit on the axial temperature via the Doppler width,

$$\Delta f_{\mathrm{FWHM}} = \frac{f_0}{c}\sqrt{\frac{2k_{\mathrm{B}}T}{m}}. \tag{8.14}$$

Here f_0 is the unshifted frequency and the resonance follows a Voigt profile with full width at half maximum (FWHM),

$$\Delta f_{\mathrm{FWHM}} = (33.8 \pm 0.07)\,\mathrm{MHz} \tag{8.15}$$

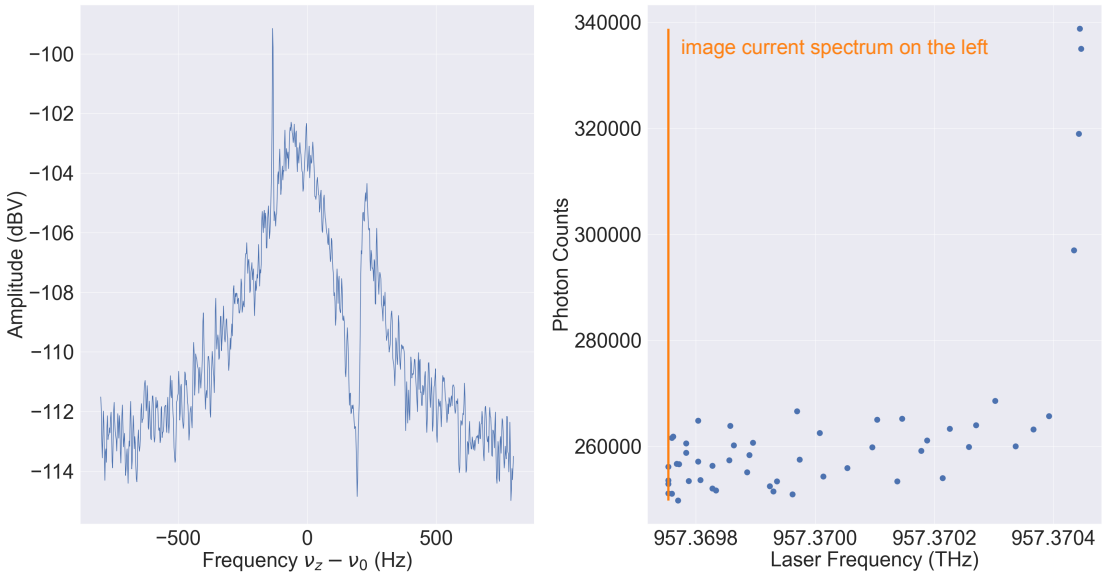

(a)

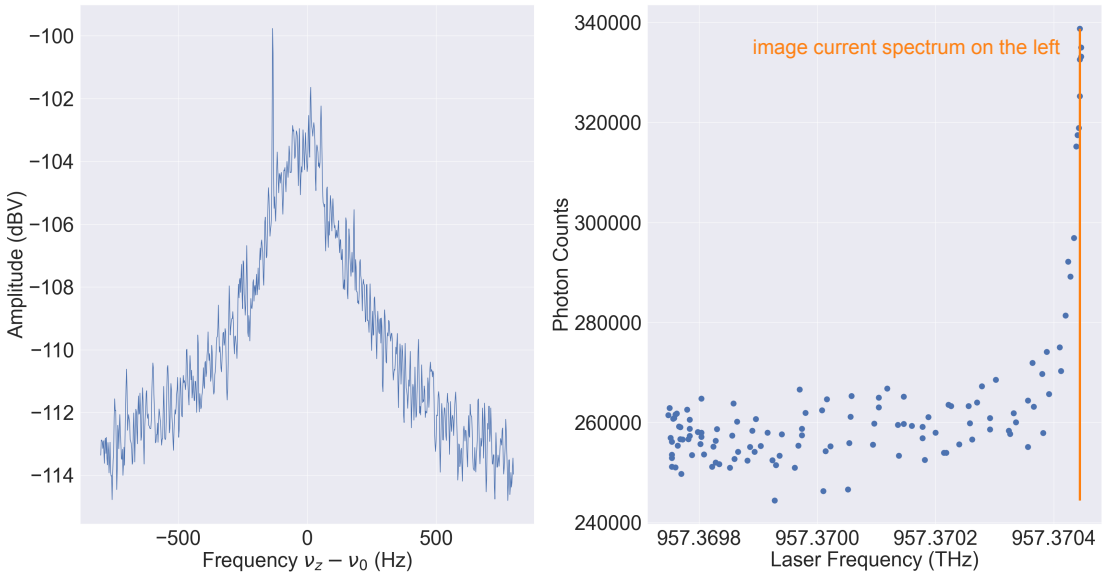

(b)

Figure 8.6: As in Section 2.2 and Fig. 8.2, the axial dip is visible when the laser is far detuned and Doppler cooling is negligible as in **(a)**, left. However when the cooling laser is brought close to resonance, Doppler cooling becomes efficient and the ions are cooled **(b)**, left. A similar cooling signal is also visible in the fluorescence spectrum (right) where, as expected, the photon count is maximized when the ions are coldest. The FFT spectrum shown on the left is taken when the laser frequency and fluorescence counts are marked by the orange line on the right.

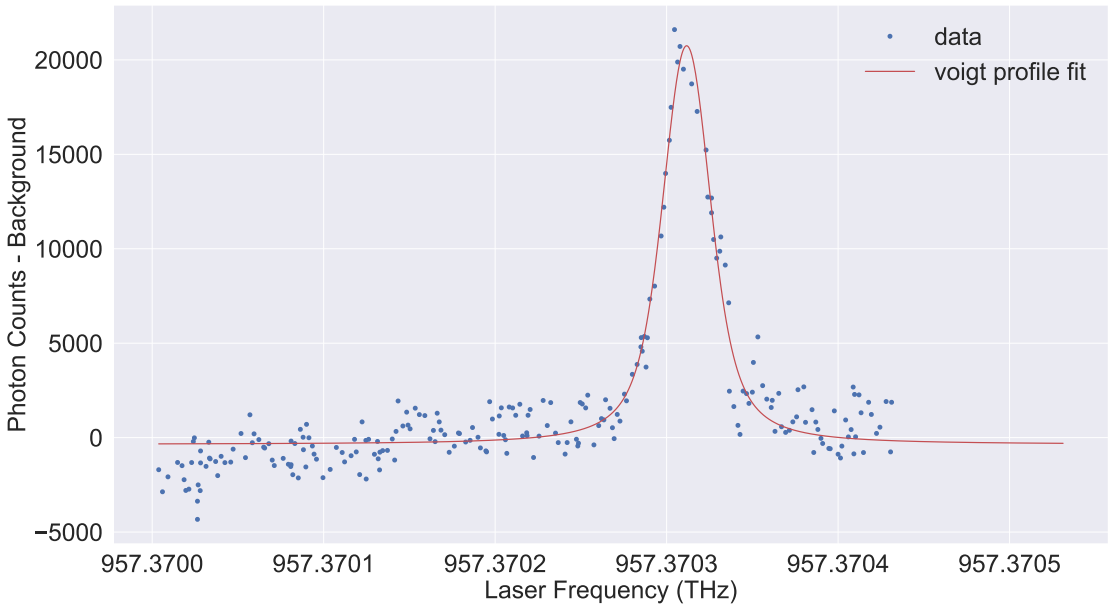

Figure 8.7: The axial temperature of the laser cooled beryllium ions can be extracted from the width of the fluorescence resonance. A fit of the Voigt profile to the data puts the axial temperature below 60 mK - see text for details.

which limits the axial temperature to,

$$T_z < 59.3\,\mathrm{mK}, \tag{8.16}$$

shown in Fig. 8.7. Note that when the laser intensity is larger, the resonance is asymmetric as the blue detuned laser quickly heats the ions.

Although the high photon background count necessitated measurements with many beryllium ions, improvements such as laser stabilization and additional in-trap shielding [67] mean that in the future it may be possible to work with single ions. This would open up an entirely new class of experiments, for example measurements with a co-trapped proton and beryllium ion.

Finally, it is important to note that these initial results, gathered in mid-2019, were a huge step forward both in this thesis work and in the development of a new proton g-factor experiment. In the end, we had three independent methods of observing beryllium cooling: the disappearance of the dip, the reduced temperature in the AT, and the narrow Doppler width fluorescence spectrum. Together these form a complete toolbox that acts as the foundation of the sympathetic cooling measurements discussed in the following chapters.

Chapter 9

Resonant Coupling

The highlights of my thesis work are the measurements demonstrating the first sympathetic cooling of protons with laser cooled ions. Instead of the common endcap coupling approach described in Chapter 2 and in Refs. [5, 50], we have developed a generalized resonant coupling scheme that couples ions in distant traps via a shared axial detection system. This approach does not rely on a shared endcap and, in addition, uses the large inductance of the resonator to compensate the capacitances of Eq. (3.66). However, in this configuration the ions are strongly coupled to the resonator throughout the entire cooling sequence and are cooled only by reducing the temperature of the complete resonant circuit. As a result, we simultaneously cool a mode of the cryogenic circuit to far below its environment temperature - similar to other experiments involving cooling macroscopic objects [93, 94, 95].

In the course of developing this technique, we developed a new theoretical model that allows us to extract the temperature of the proton, resonator, and laser cooled beryllium ions, while not neglecting the contributions of the resonator coupled to the environment. The first results are also shown, in which energy exchange is observed between distant, resonantly coupled traps. In additional measurements, a parametric excitation is applied to beryllium ions in one trap which then excite the proton in another trap. With this foundation, we were then able to cool both the resonator and the proton by exchanging energy with damped, laser cooled ions.

9.1 Theoretical Model

The measurements performed in this chapter all rely on the image current interaction of two ions in distant traps, mediated by the axial detection system. More specifically, a single proton is stored in the PT while one or more beryllium ions are stored in the ST. The PT and the ST share a common axial detection sys-

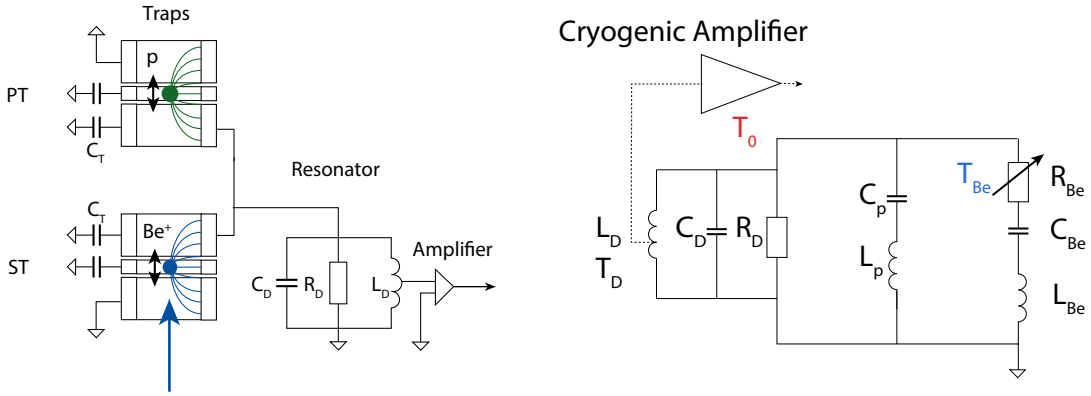

(a)

(b)

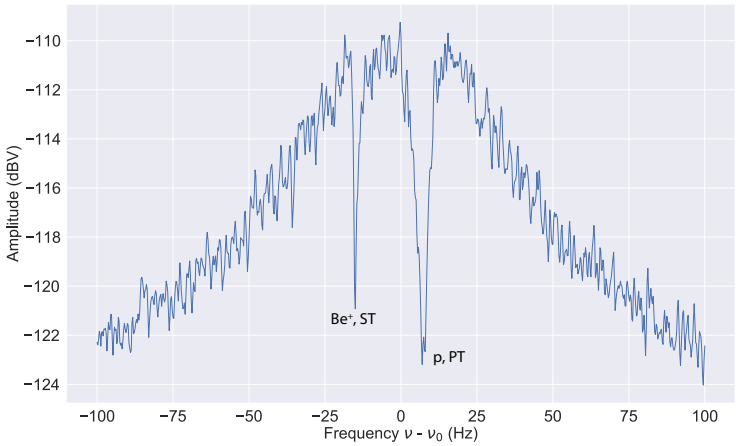

(c)

Figure 9.1: **(a)** The PT and the ST are capacitively decoupled and connected to a single axial resonator. **(b)** In this configuration the system can be modeled by the equivalent circuit shown here. **(c)** An example FFT spectrum of such a configuration is shown and the beryllium and proton dip can be distinguished by their respective dip widths, $\gamma_p \approx 2.5\gamma_{Be}$ for single particles. Here the beryllium ion is stored in the ST while the proton is stored in the PT.

tem and can be modeled by the equivalent circuit shown in Fig. 9.1. The simplest measurement with this system is an examination of the FFT spectrum at thermal temperatures. Shown in Fig. 9.1, the ring voltage of the ST is kept constant and the axial frequency of the beryllium ions is fixed. Meanwhile the ring voltage, V_r, in the PT is increased linearly with the axial frequency of the proton following. Measured away from the center of the resonator, both dips appear in an FFT spectrum when the axial frequencies are separated by more than the coupling frequency. However, when $\nu_{z,Be} \approx \nu_{z,p}$ an avoided crossing appears[1]. This splitting, which occurs in any system of two coupled oscillators, arises from the fact that the system is now best described by a set of normal modes, in analogy to secular motion in an rf trap or connected masses and springs. The same phenomenon can also be observed in the sideband spectra described in Section 2.1.5. Shown in Fig. 9.2, this splitting is extremely hard to resolve and in practice, means that fitting dip spectra becomes untenable. As a result, we instead plot the amplitude of each FFT bin as a function of the ring voltage and, equivalently, axial frequency of the "probe" particle - in this case the proton. The slight bending of the axial frequency is a clear indication of coupling between the two traps. Notably this data has been compared to simulations performed by Christian Will (who also developed the data visualization method of Fig. 9.2) and shows good agreement.

However, when resonantly coupling laser cooled ions, some of the assumptions of the previous chapters no longer hold. For example, until now the axial temperature of the trapped particle has been determined by the temperature of the axial detection system. While this remains true for the proton, laser cooled beryllium ions act as an additional damping force and change the temperature of both the ions and the resonator. More concretely, in the absence of laser cooling the following relations hold,

$$\langle P_D \rangle = k_B T_D \Delta f = \left\langle J_z^2 \right\rangle R = \gamma_{Be}\, k_B\, T_z = -\left\langle \frac{dE_z}{dt} \right\rangle . \tag{9.1}$$

Here, P_D is the power dissipated by the detector at temperature T_D due to image currents, J_z, induced by the beryllium ions at temperature T_z. In this case, the ions are damped exclusively by the detector so $T_z = T_D$ and the bandwidth Δf is equal to the full width at half maximum (FWHM) of the dip, γ_{Be}[2]. When laser cooling is applied, the system comes to thermal equilibrium and the temperature of the ions is given by a power balance equation,

$$-\left\langle \frac{dE_{Be}}{dt} \right\rangle = \langle P_D \rangle + \langle P_L \rangle . \tag{9.2}$$

[1] Although this is notably not the case when the ions are *exactly* on resonace. In this situation one of the dips "disappears" in analogy to electromagnetically induced transparency (EIT). This is described in more detail in [96]. Due to the narrow axial frequency splitting this phenomenon is difficult to resolve in our experiment.

[2] Note that the dip width used throughout this thesis, and by the group as a whole, is the 3 dB width, measured from the bottom of the dip whereas Δf is the FWHM. However, since in what follows γ_{Be} only appears as a ratio to other coupling factors, the notation γ_{Be} is retained.

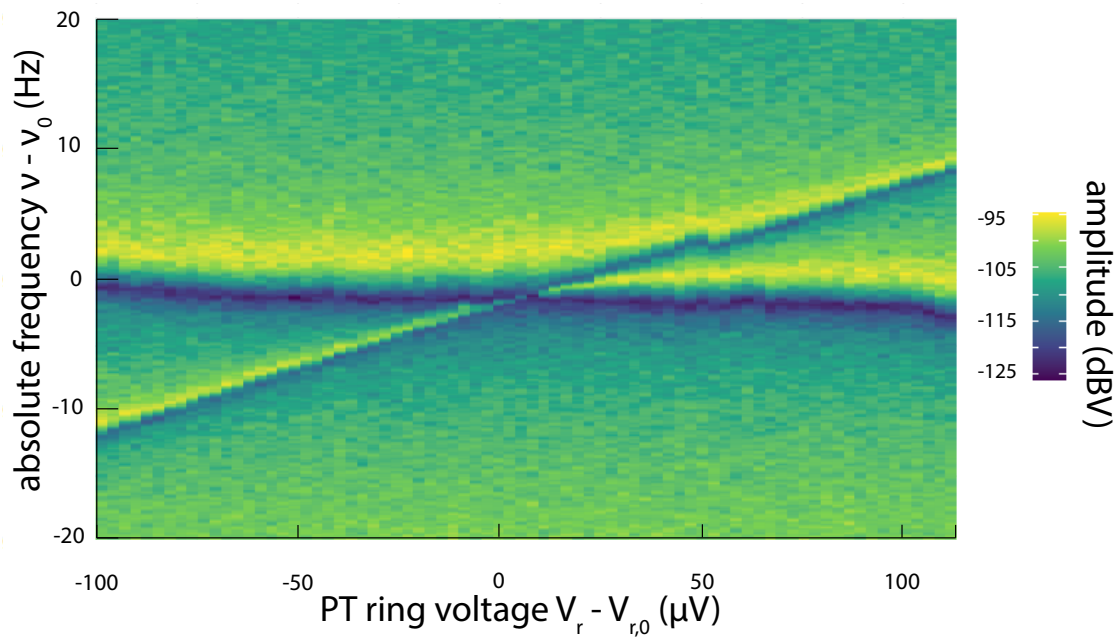

Figure 9.2: In a frequency region away from the center of the resonator, the axial frequency of the proton kept constant while the axial frequency of a single beryllium ion is increased by changing the ring voltage. Fitting dip spectra is difficult in the region of interest, instead only the amplitude of the FFT spectrum is shown. The avoided crossing, while small, is a signal of coupling between the two trapped particles - see text for details. Figure adapted from one provided by Christian Will.

That is, the power associated with the axial motion of the beryllium ions, $-\left\langle \frac{dE_{Be}}{dt} \right\rangle$, is dissipated exclusively by the detector and laser with power $\langle P_D \rangle$ and $\langle P_L \rangle$, respectively. This dissipation occurs on a time scale characterized by the coupling of the ions to each element i.e.,

$$-\left\langle \frac{dE_{Be}}{dt} \right\rangle = k_{\mathrm{B}}\, T_z \left(\widetilde{\gamma}_{Be} + \gamma_L\right). \tag{9.3}$$

Here the coupling to the detector, $\widetilde{\gamma}_{Be}$, is no longer just $2\,\gamma_{Be}$ but is reduced by the coupling of the beryllium ions to the laser with effective coupling time γ_L. Eqs. (9.1), (9.2), and (9.3) can then be combined to produce

$$T_{Be}(\widetilde{\gamma}_{Be} + \gamma_L) = T_D\widetilde{\gamma}_{Be} + T_L\gamma_L, \tag{9.4}$$

which generalizes the "disappearing dip" phenomenon described in Chapter 8. In fact, shown in Fig. 9.3, the amplitude of the dip is reduced by additional damping from the cooling laser with damping constant γ_L. The current induced by the ions while damped by the laser is then denoted $\widetilde{J}_z$ and the image current interaction is then described by,

$$k_{\mathrm{B}} T_D \widetilde{\gamma}_{Be} = \left\langle \widetilde{J}_z^2 \right\rangle R_p \tag{9.5}$$

where T_D is the reduced temperature of the detector. The coupling of the ions to the detector can then be written as

$$\widetilde{\gamma}_{Be} = \frac{T_D}{T_0} \frac{\left\langle \widetilde{J}_z^2 \right\rangle}{\langle J_z^2 \rangle} \gamma_{Be}, \tag{9.6}$$

by combining Eq. (9.1) and (9.5). We then introduce a measurable parameter, k, given as

$$k = \frac{\left\langle \widetilde{J}_z^2 \right\rangle}{\langle J_z^2 \rangle}. \tag{9.7}$$

In principle, k can be determined experimentally from a variety of methods, for example from the FFT spectrum, as in Fig. 9.3, using the equation

$$k = \frac{\int_0^{\mathrm{inf}} S_R(\nu) - S_{R,Be}(\nu, \gamma_L)\, d\nu}{\int_0^{\mathrm{inf}} S_R(\nu) - S_{R,Be}(\nu, \gamma_L = 0)\, d\nu}. \tag{9.8}$$

In this interpretation, k is the ratio of the area of the dip spectrum in the presence of the laser with damping constant γ_L to the area of the dip spectrum without the cooling laser. In Fig. 9.3, for example, $k \approx 0.55$. As a result, the difficult to measure $\widetilde{\gamma}_{Be}$ can be written as

$$\widetilde{\gamma}_{Be} = \frac{T_0}{T_D}\, k\, \gamma_{Be}, \tag{9.9}$$

where T_0 is the unperturbed resonator temperature, found in Chapter 4 to be $T_0 = (17.36 \pm 0.42)\,\mathrm{K}$.

Similarly, from the circuit model in Fig. 9.1, the coupling to the laser, γ_L, can be written as,

$$\gamma_L = \frac{I_L^2 R_L}{k_{\mathrm{B}} T_L}, \tag{9.10}$$

where I_L, R_L, and T_L are, respectively, the equivalent current, resistance, and temperature values arising from damping of the ions by the cooling laser. Kirchhoff's current and voltage laws can then be applied, yielding the equations:

$$I_L = \langle J_z \rangle - \left\langle \widetilde{J}_z \right\rangle \tag{9.11}$$

$$R_L I_L = R_D \left\langle \widetilde{J}_z \right\rangle, \tag{9.12}$$

where R_D is the equivalent resistance of the resonator. After rearranging terms, γ_L can be expressed as,

$$\gamma_L = \frac{T_0}{T_L} \gamma_{Be} \left(\sqrt{k} - k \right). \tag{9.13}$$

Finally, a power balance equation can be applied again to each element of the system to determine the temperature of the proton, beryllium ions and resonator where,

$$T_p = T_D \tag{9.14}$$

$$T_D = \frac{T_0 \gamma_D + T_{Be} \widetilde{\gamma}_{Be}}{\gamma_D + \widetilde{\gamma}_{Be}} \tag{9.15}$$

$$T_{Be} = \frac{T_D \widetilde{\gamma}_{Be} + T_L \gamma_L}{\widetilde{\gamma}_{Be} + \gamma_L}, \tag{9.16}$$

and γ_D is the width of the resonator. However, $\widetilde{\gamma}_{Be}$ and γ_L are not readily available from the experimental data and can be rewritten using only k and γ_{Be} by substituting in Eqs. (9.13) and (9.9).

Although T_p, T_D, and T_{Be} have algebraic solutions that are easily calculable with a computer algebra system (CAS), the results are very long and not reproduced here. However, the temperature during resonant cooling can be expressed with independently measured quantities and show that dip detection even during of laser cooling is possible. Shown in Fig. 9.4, one of the most important parameters describing such a system is k. Qualitatively, for a fixed dip width, increasing k lowers the temperature of the detector and proton until reaching a saturation point and increasing again when the beryllium ions completely decouple from the detector near $k = 1$ and the dip vanishes.

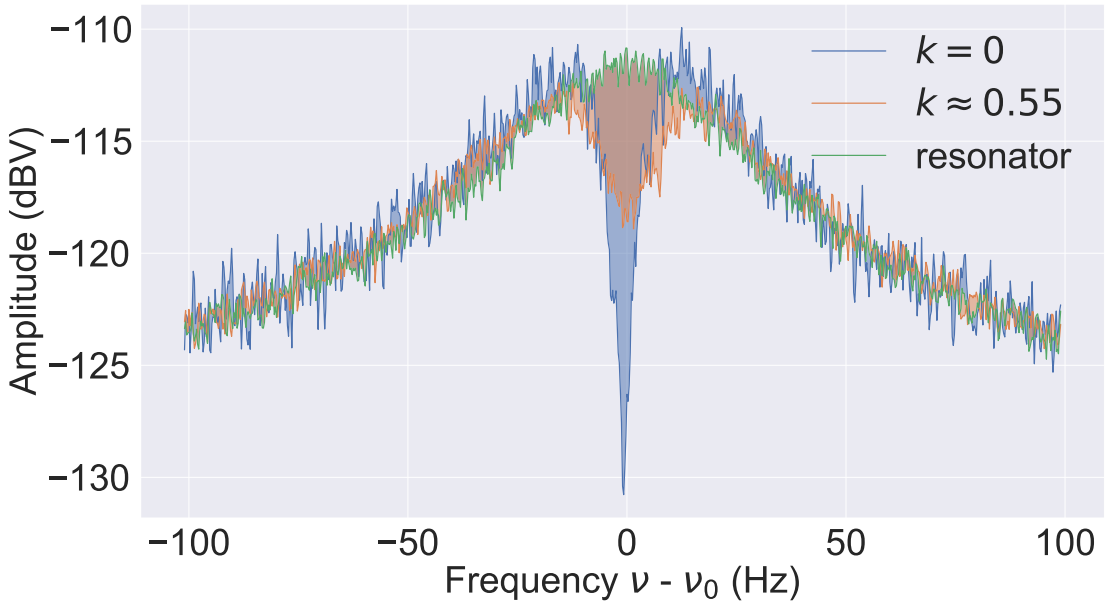

Figure 9.3: The FFT spectrum of the resonator in addition to the resonator with and in the absence of additional damping of the beryllium ions from the laser. γ_L and γ_{Be} are defined in the text k is given by the ratio of the blue to orange shaded region.

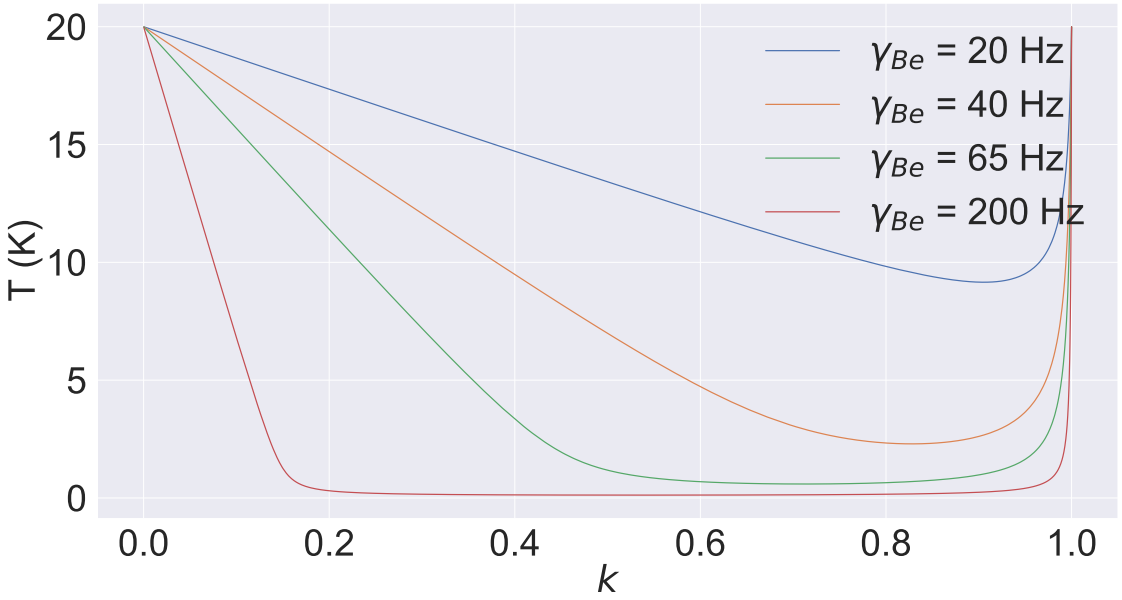

Figure 9.4: The temperature of the detector and thus proton is shown as a function of k. For fixed coupling to the detector, γ_{Be}, and an effective "laser temperature" of $T_L = 50\,\text{mK}$ the temperature of the detector and resonator decrease nearly linearly with k until reaching a saturation point and rapidly increasing near the $k = 1$ discontinuity point.

9.2 Resonant Excitation

However, the first demonstration of ion-ion coupling via the resonant circuit was not with sympathetic cooling but rather with energy exchange from excited ions. More specifically, as shown in Fig. 9.5, we apply a small parametric excitation at frequency $2\nu_z$ to the ST which excites the beryllium ions. This lowers the SNR of the dip, but does not result in a peak on the detector. We also confirm experimentally that this drive does not heat the proton in the absence of beryllium ions. After the excited beryllium ions and the proton are brought into resonance, the beryllium ions excite a narrow band of the resonator which in turn excites the proton. We can then tune the proton temperature by changing the amplitude of the drive in the ST, thus changing the energy of the ions. The experimental sequence is as follows:

1. First, we measure the axial frequency of the proton in the PT, $\nu_{z,1}$, while the beryllium ions, in the ST, are detuned by adjusting the ring voltage.

2. The beryllium ions are then brought into resonance with the proton and the detector and are parametrically excited with a drive in the ST at $\nu_{\mathrm{rf}} = 2\nu_z$. In this instance, the beryllium ions and the proton have the same axial frequency but the parametric drive is weak enough and applied far enough away that it does not directly excite the proton.

3. During this excitation the axial mode of the proton, in resonance with the axial mode of the beryllium ions, is coupled to the cyclotron motion with a sideband drive at $\nu_{SB+} = \nu_+ - \nu_z$. This translates the axial energy of the proton, in thermal interaction with the excited beryllium ions, to the cyclotron mode of the proton.

4. The beryllium ions are once again detuned, and the axial frequency of the proton, $\nu_{z,2}$, is measured again.

At low energy the resulting frequency shift, $\Delta\nu_z = \nu_{z,2} - \nu_{z,1}$, arises from a nonzero B_2 component of the magnetic field, due mainly to contributions from the ferromagnetic ring electrode in the AT. Again, the shift of 3.54 can be written with the experimental parameter $\kappa_{B_2,PT}$, and in this case,

$$\Delta\nu_z = \kappa_{B_2,PT}\, T_+ = -85\,\mu\mathrm{Hz/K} \approx 1\,\mathrm{Hz/eV}. \tag{9.17}$$

At higher energies, as shown in Fig. 9.6, the radial energy of the proton can be up to several thousand kelvin or a few eV where $T_+ > T_z \gg T_0$. At such high energies, the axial frequency shifts are no longer Boltzmann distributed and the energy distribution arises from the amplitude noise of the rf drive. As a result, it is no longer possible to assign a temperature to the proton but instead the mean

energy and the spread around the mean are given. In addition, higher order terms become relevant, namely,

$$\Delta\omega_z \propto C_n\, T^{n/2} \tag{9.18}$$

$$\Delta\omega_z \propto B_m\, T^{m/2} \tag{9.19}$$

with $n, m \geq 4$. However, Monte-Carlo simulations with shifts due to these additional terms do match the data of Fig. 9.6.

Again, and importantly, we also confirm that the proton is excited only by the beryllium ions - not by coupling to the excitation drive. Shown in Fig .9.5 **(a)**, the FFT spectrum is taken with no excitation drive applied and appears identical to the spectrum in Fig .9.5 **(c)** in which the excitation drive is applied in the ST but with the beryllium ions detuned. In addition, shown in Fig .9.5 **(b)**, while the drive is applied, the proton detuned, and the beryllium ions on resonance, the SNR of the beryllium dip is reduced but no peak appears. It is only in Fig .9.5 **(d)**, in which the drive is in resonance with the beryllium ions which are in turn resonance with the proton in which a large peak appears, confirming that the energy exchange between the traps is mediated by the detector and the ions - not by the drive itself. In fact, the entire experimental sequence described above was performed at varying detunings of the beryllium axial frequency. Unless on resonance, the energy scatter was consistent with the scatter of the cyclotron sideband, as in Section 6.4.1.

With this measurement we make a number of important steps. First, we conclusively show the resonant exchange of energy from a particle in one trap to a particle in another, relying exclusively on the image current interaction. Importantly, this energy transfer is independent of the resonator energy meaning that it is possible to bring the entire system to a temperature not determined by the axial amplifier or the cryogenic environment. This ultimately lays the foundation for cooling - the capstone of this entire work.

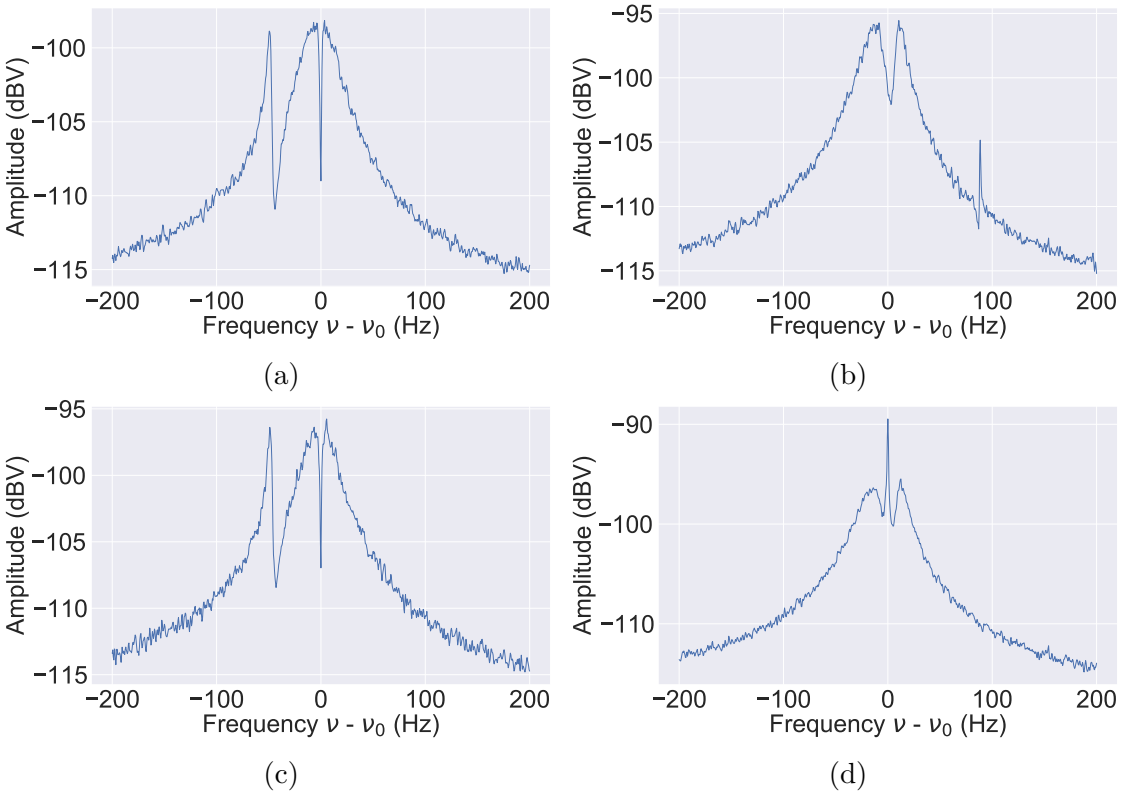

Figure 9.5: **(a)** The proton is on resonance is in resonance with the detector, while the beryllium ions are detuned, and no drives applied. **(b)** The proton is detuned from the resonator while the beryllium ions are on resonance and the $2\nu_z$ excitation is applied. Note that the drive strength is chosen to reduce the signal-to-noise ratio of the beryllium dip but not to result in a peak. **(c)** The $2\nu_z$ drive is applied as in **(b)**, but the beryllium ions are detuned and the proton remains at the thermal temperature of the resonator. **(d)** The proton and beryllium ions are both in resonance with the detector and the excitation is applied. The proton appears as a peak above the thermal noise of the resonator.

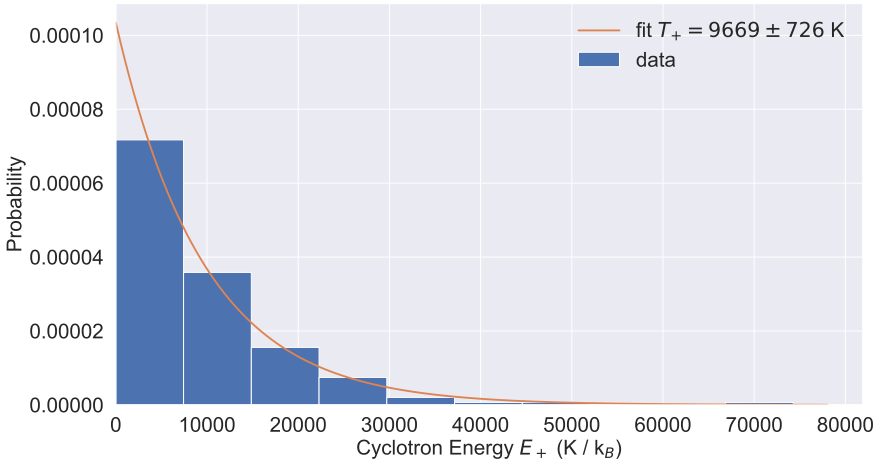

(a)

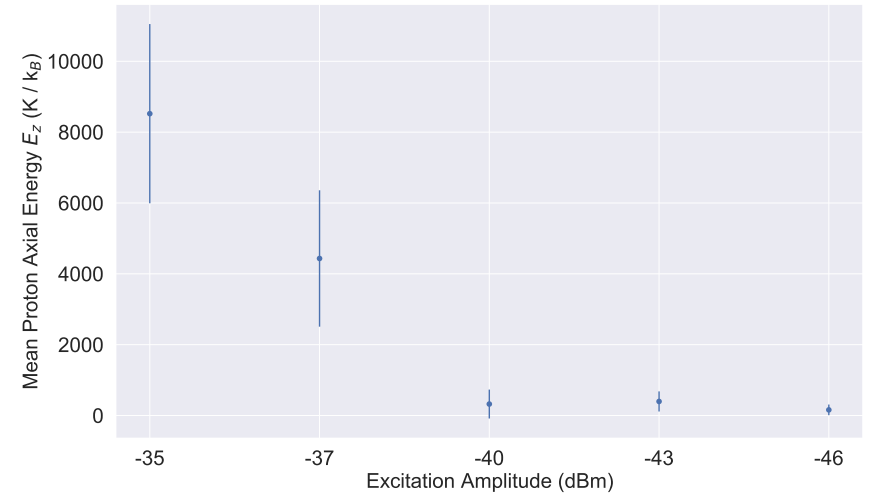

(b)

Figure 9.6: **(a)** A single measurement of the resulting temperature of a proton in the PT coupled to beryllium ions in the ST with an excitation drive at $-46\,\mathrm{dBm}$. The resulting temperature is measured to be $T_+ = 9669 \pm 726\,\mathrm{K} \rightarrow T_z = 160 \pm 12\,\mathrm{K}$ by a maximum likelihood parameter estimation. **(b)** The mean proton energy as a function of the amplitude of the excitation drive applied to the beryllium ions is shown and at low amplitude we observe the behavior in **(a)** - see text for details.

9.3 Proton Cooling

With the coupling between the ions and the proton clearly seen in both the avoided crossing and the resonant excitation measurements, the next step was to include the laser for Doppler cooling. In both of these previous measurements though, the coupling signal was the axial dip spectrum. With the "disappearing dip" phenomenon described in Chapter 8, however, that signal goes away during the most straightforward application of laser cooling. As a result, using the model described earlier, we instead chose to operate at large laser detunings and cool the entire system. In this configuration beryllium ions in the ST are cooled with a laser frequency set so that the dip spectrum looks similar to the orange spectrum in Fig. 9.3. The proton is then brought into resonance, resulting in a spectrum like the one shown in Fig. 9.7. In the theoretical model developed in this thesis, a large area dip corresponds to a small k-value, while the disappearing dip corresponds to $k \approx 1$.

We can then use the C_4 induced shift of the axial frequency, described in Section 4.4.2, to measure the temperature of the proton and the axial detection system. In fact, this measurement is extremely similar to the one described there, i.e. we measure

$$\Delta\nu_z = \kappa_{D_4}\, T_z\, \Delta\mathrm{TR}, \tag{9.20}$$

but instead of changing T_z with electronic feedback, the circuit is sympathetically cooled by the beryllium ions. In addition we performed a complete measurement campaign, tuning $T_z = T_D = T_p$ through the coupling to the detector, $\gamma_{Be} \propto N$, and the "laser temperature" with the laser detuning $T_L(\delta)$.

The experimental sequence for a given laser detuning δ follows below.

1. The axial frequency of the proton, $\nu_{z,1}$, is measured.

2. Beryllium ions are brought into resonance with the proton and the detector, and the Doppler cooling laser is applied. No additional excitations are used and the axial frequency of the proton, $\nu_{z,2}$, is measured again while the beryllium ions are still present.

3. This is then repeated at different tuning ratios, yielding shifts, $\Delta\nu_z = \nu_{z,1} - \nu_{z,2}$ as a function of TR.

The results of an individual measurement are shown in Fig. 9.8 in which the slope m of the blue axial frequency shifts gives the change in temperature of the cooled proton and equivalently the temperature of the axial detection system by

$$\Delta T_D = \Delta T_p = \frac{m}{\kappa_{D_4}}. \tag{9.21}$$

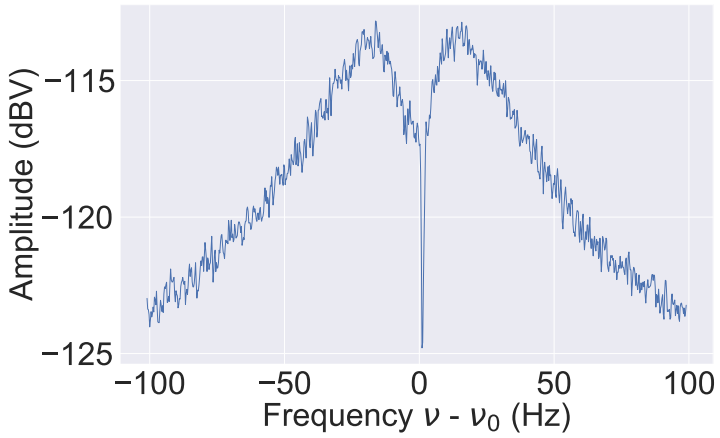

Figure 9.7: The FFT spectrum of the proton, beryllium ions, and resonator with additional damping of the beryllium ions from the laser is shown for a typical setting. The axial frequency of the proton is shifted slightly due to the C_4T_z shift.

The orange points in Fig. 9.8 show a control measurement, in which we apply the same measurement routine, but with the axial frequency of the beryllium ions detuned from the proton frequency. As expected, when the ions are far detuned from resonance there is no change in temperature and no axial frequency shift. However, in the resonant case we see a clear modification of the axial frequency through a frequency shift $\nu_{z,1} - \nu_{z,2}$, which indicates sympathetic cooling of the single trapped proton by means of resonant coupling to laser-cooled ions.

We also qualitatively observe behavior consistent with the temperature model described above by measuring the temperature of the proton as a function of the number of beryllium ions, changing γ_{Be} by increasing the number of trapped beryllium ions by, $\gamma_{Be} \propto N_{Be}$ with results shown in Fig. 9.9. Notably though, k varies with N_{Be} and we need to bring k to a value at which the frequency of the proton dip can still be observed. However, modifications of the resonator spectrum at varying N_{Be} and fluctuating noise temperature due to laser cooling mean that extraction of k from the FFT spectrum can be unreliable. As a result, a full quantitative analysis remains as a goal for the future. With increasing γ_{Be} the beryllium dip remains visible on the detector at detunings δ closer to $\delta = f_0 - \Gamma_0/2$ - i.e. the detuning at which the Doppler limit is reached where f_0 is the center of the cooling transition and Γ_0 is the natural linewidth. The temperature model used here however, required significant refinement and was not fully developed until after the experimental run had been completed. As a result, while used to guide some of the discussion in the following outlook, the temperature model should be fully tested in the future. For example, although the data used in Fig. 9.9 can, in principle, be used to extract k, via Eq. (9.8), in practice such an analysis is difficult. While the axial energies of both the proton and beryllium ions are Boltzmann distributed - effectively broadening the axial dip - the SNR of the proton dip is constant and shorts the noise of the resonator. The beryllium dip, on the other hand, is "smeared out" not only in frequency but in

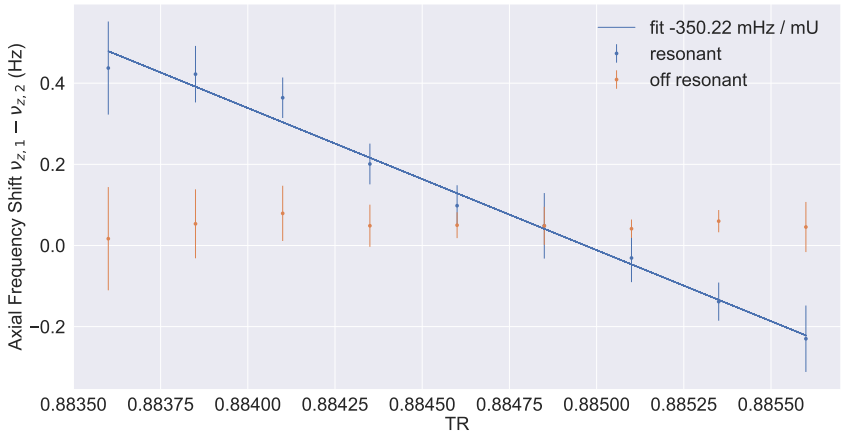

Figure 9.8: The axial frequency shift $\nu_{z,1} - \nu_{z,2}$ is shown as a function of the tuning ratio which is applied to the correction electrodes. For beryllium ions tuned to resonance (blue) a fit to the data yields the change in temperature, ΔT_D and when the beryllium ions are tuned away from resonance (orange) $\Delta T_D = 0$. See text for details.

the SNR. In future experiments, e.g. with fluorescence detection, k can be extracted independently and the behavior of the system can be fully characterized.

Finally, we assigned a minimum temperature by measuring the temperature of the proton with large beryllium ion clouds. Although larger ion numbers are likely possible, we ultimately found a minimum temperature, limited by the measurement resolution, of,

$$T_{p,\min} = T_0 + \Delta T_{p,\max} = 17.34 - 14.52\,\mathrm{K} = 2.82^{+3.35}_{-2.82}\,\mathrm{K}. \tag{9.22}$$

Here, $\Delta T_{p,\max}$ is the maximum reduction in temperature and is determined by the weighted average of the three minimum points around the gray line in Fig. 9.9. The uncertainty is limited by the C_4 shift method and the zero bound $T_p > 0$ and is determined by the average error of the two feedback temperature measurements shown in Table 12.2.

Ultimately, T_p here was likely limited by the ion number and the high temperature of the axial detection system. In the future, with an axial detector temperature closer to 4 K (well demonstrated in our previous experiments [2, 1, 3]), the goal of an improved g-factor measurement campaign with sympathetically cooled protons using exactly this method is well within reach. We have demonstrated, for the first time, sympathetic cooling of a particle with no optical spectrum by coupling via image currents to laser cooled ions. It is the first realization of a 30 year old idea, with considerable potential to enhance precision measurements of fundamental properties of fundamental particles - most importantly the proton and the antiproton. Moreover, this newly developed resonant coupling technique has broader application to a wide range of experiments. The remainder of this thesis

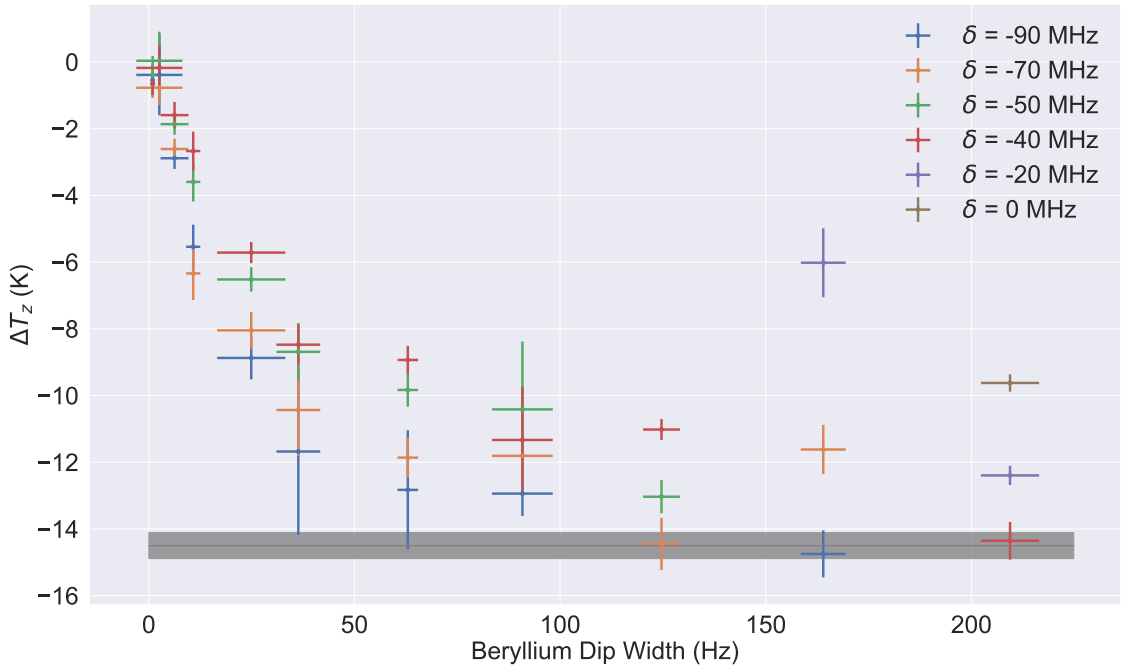

(a)

Figure 9.9: The coupling of the beryllium ions to the detector, k, is varied by changing the number of ions $N_{Be} \propto \gamma_{Be}$ and δ, the laser detuning from the highest frequency used in the measurement campaign. Note that when k is close to one, $\mathrm{SNR}_p - \mathrm{SNR}_{Be}$ is small and it is difficult to resolve the proton axial frequency, resulting in large uncertainties at some detunings. The minimum ΔT_d is shown by the gray band and is the weighted average of the minimum three points.

discusses some of these possibilities and places the measurements in the context of larger physics goals.

Chapter 10

Outlook

While important and the culmination of several years of work, these results are preliminary. Sympathetic cooling of a particle with no optical spectrum is a big step forward, but the minimum temperatures given at the end of Chapter 9 cannot be resolved to high enough precision for an improved proton g-factor measurement at high duty cycle. In a very real sense then, there is a decision to make going forward, about how to prepare cold particles in Penning traps. In my opinion, there are essentially, four related, but ultimately unique approaches that each have considerable value. This chapter aims to describe the benefits and drawbacks of each approach, with an emphasis placed on the resonant coupling. In particular, my goal is to take the resonant coupling technique seriously and think about how a new experiment could be designed that would maximize its utility.

10.1 How to Proceed?

10.1.1 Dilution Refrigeration

In some sense the most obvious approach, the bath cryostat could be replaced by a dilution fridge. In fact, it is not necessary to even cool the entire apparatus - all that is required is that the resonators and amplifiers are cooled with the dilution fridge, all other components could remain at 4 K. Of course, dilution fridges have very little cooling power (roughly three orders of magnitude less than the current thermal load), but if our group had chosen to pursue this approach I think it's very likely that we would have an improved value for the proton g-factor now. It would certainly be a similar challenge to engineer a new mechanical assembly but all other techniques used in the 2017 g-factor measurement would still be applicable. Critically, nothing would need to change inside the trap chamber.

On the other hand this simplicity means that new methods would necessarily not be developed. The techniques used in rf traps with optically addressable ions are still vastly underdeveloped in Penning traps - in fact underdeveloped in a large number of precision physics experiments. Ultimately, the question is of priorities - is it more important to produce a new, higher precision value of a fundamental constant or is it more important to develop new techniques that can enable a new class of measurements? Our aim, decided nearly ten years ago, was to use the Mainz experiment as a test bed for new developments that could ultimately be applied to the CERN experiment as well. I'm happy to have contributed to this goal.

10.1.2 Quantum Logic Spectroscopy

On the other end of this technology spectrum lies quantum logic spectroscopy (QLS). This is the technique used to great success in, e.g. atomic and molecular ion clocks [97, 98] and is the approach taken by the Hannover group to improve the g-factor of the proton and antiproton [8, 99]. Again the benefits are striking - just as atomic clocks were able to improve dramatically by switching from a lower $Q \sim \delta\nu/\nu$ microwave oscillator to a higher Q optical oscillator, similar gains in precision might be achieved by optically driving cyclotron and Larmor transitions of a proton. Of course, there is a reason why Penning traps are so underdeveloped with lasers. While it's relatively straightforward to Doppler cool ions in a Penning trap the results from the Imperial College group have shown that the large magnetic field can introduce many complications [48, 100]. In addition, the magnetic field itself can be a challenge - fluctuations decrease the coherence time of any operation, whether cyclotron or Larmor frequencies or atomic transition frequencies.

It seems clear that the QLS approach is the right one in the long term. Aside from the fact that optical clocks based on QLS are the most precisely realized physical systems, image current detection is inherently slow. FFT spectra take roughly one minute, whereas an generic optical "gate operation" takes at most a few ms to perform and read out. In the short term though, these techniques not quite ready for an improved g-factor measurement. Finally, it's important to mention that while the QLS approach taken by the Hannover group uses particles stored in two close, but separate traps (as is necessary for the measurements with the antiproton) - measurements with a proton can be performed with a co-trapped single beryllium ion - building on the success of the "two-ion crystal" [101, 7, 102].

10.1.3 Common Electrode Coupling

Of course, as the focus of my thesis work I have some bias towards this technique. As a medium term approach, common electrode coupling has significant value for precision measurements in Penning traps and beyond. There is a big question about

which approach to common electrode coupling is correct though. The original approach, described at the end of Chapter 2, is what we've started referring to as capacitive coupling. With this approach, and a switchable resonator, there is no fundamental limit to the particle temperature as additional heating rates are negligible. However, it is also extremely slow with coupling rates, as designed, of around a minute. Resonant coupling is dramatically faster - around two orders of magnitude. However, without clever sequencing (coming at the cost of the coupling rate) the particle temperature will be limited, roughly by the ratio of the dip width to the resonator width.

The immediate plans for the Mainz apparatus are to implement the capacitive coupling and finally demonstrate particle temperatures near the Doppler limit by implementing the high-Q capactive switch described in Chapter 2. This is a good approach and will fully implement the cooling scheme first described 30 years ago [5]. In what follows though, I propose a new design that fully exploits the resonant coupling technique to achieve very cold particle temperatures, with high coupling rates.

10.1.4 Resonant Coupling - Proposal for a New Experiment Design

Discussed in Chapter 4, there is little to optimize with trap design - especially for the capactive coupling. While the number of beryllium ions certainly appears to be an attractive tuning knob, in practice we find it difficult to work with more than a few hundred ions. Namely the ion-ion interactions and slow cooling times can lead to unpredictable shifts and continuous operation can be a challenge. Similarly, while the trap capacitance was minimized during the design process it's not feasible to bring this down further - at least with the current design in which large metal electrodes are separated by quartz or sapphire rings. As a result, the trap radius and thus effective electrode distance, $D_{\text{eff}} \propto r$ seems to be a relatively unoptimized element. However, even with sub-mm traps, the coupling rate for the capacitive coupling will be below a Hz.

However, when thinking about the resonant coupling case things become much different. The cooling rate will essentially be given by the dip width of the proton while the temperature is set by the dip width of the beryllium ions. The limitations on trap radius have typically been set by concerns about patch potentials and voltage stability at low voltages. However the following relations are useful to

r (mm)	C_2 (m^{-2})	D_{eff}	V_r (V)	γ_{Be} (Hz)	$T_{N=1}$ (K)	$T_{N=10}$ (mK)
0.25	6.0×10^6	0.4	0.17	480	0.12	57
0.50	1.5×10^6	0.8	0.69	120	0.38	77
1.0	3.8×10^5	1.6	2.8	19	2.4	240

Table 10.1: Shown here are the parameters for a proposed new, small coupling trap. At $r = 0.5\,\text{mm}$, the trap is still relatively large but yields a very large dip width $\gamma_{\text{Be}} \approx 120\,\text{Hz}$ with reasonable ring voltage V_r at $\nu_z = 750\,\text{kHz}$. The minimum temperature of the proton and detection system is given for a single ion and ten ions assuming the beryllium ions are cooled to the 50 mK demonstrated in the fluorescence measurements. Cooling to the Doppler limit dramatically increases performance.

consider:

$$\gamma \propto \frac{1}{r^2} \tag{10.1}$$

$$V_r \propto m\sqrt{C_2} \propto m\,r \tag{10.2}$$

$$m_{Be} \approx 9\,m_p. \tag{10.3}$$

$$\tag{10.4}$$

Although challenging to construct, I propose using a small $r = 0.5\,\text{mm}$ trap, to fully exploit the resonant coupling methods developed in this thesis. Table 10.1 shows the approximate values of important trap parameters assuming a 5-pole, orthogonal, and compensated trap.[1]

At $r = 0.5\,\text{mm}$, the trap is still macroscopic and could, in theory, be developed without micro-fabrication processes and still be trapped with voltages on the scale we are comfortable working with. Of course, if the micro-fabrication is desired or necessary, an even smaller $r = 0.25\,\text{mm}$ trap produces an even larger dip width γ_{Be} - trap parameters for $r = 0.25\,\text{mm}$, $r = 0.5\,\text{mm}$, and $r = 1\,\text{mm}$ are given in Table 10.1.

Similar performance also seems possible by developing a much higher Q resonator without changing the oscillator type. In particular, the dominant limitation on the resonator Q-value at present is the amplifier but an amplifier is not necessarily required for the coupling. With relatively marginal improvements to the resonator (e.g. using a superconducting housing and further minimizing losses in

[1] Alternately, similar performance could be achieved by replacing the superconducting circuit with an alternative oscillator. As discussed in [93], the resonant coupling can be mediated not by the traditional image current detector coil but with a high-Q quartz resonator, nano-mechanical acoustic resonator, or even superconducting circuits. In fact, the use of a quartz resonator in Penning traps has already been demonstrated in [103], although the coupling of the resonator to the ion depends on more than just the Q-value and in many cases there will be no gain in performance.

the magnetic field) at least an order of magnitude could be gained. In fact, during resonator testing we have seen resonator widths on the order of 1 Hz, compared to the $\sim$ 30 Hz used during the measurements of Chapter 9. In fact, with a switchable detector, a "hybrid" coupling method can be imagined in which the benefits of both the capacitive and resonant coupling techniques are utilized. Namely, each trap would be connected to two resonators, first a "readout" resonator similar to those described in this thesis. This resonator would be used to readout the axial frequency and would be detuned in a measurement - exactly as with the capacitive coupling. However an additional, narrow detector with no amplifier could remain during the coupling - enhancing the exchange time while only minimally heating the ions. A "dream experiment" then could consist of combining this method and a small radius trap.

Importantly though, even if these approaches are not followed large gains could be made in a proton g-factor measurement using an apparatus very similar to the one used in this thesis. Even with high cyclotron temperatures, e.g. on the order of 1 K, selective cooling such as used with selective resistive cooling in Section 3.2.1 and Section 4.1 the time cycle of a measurement could be reduced dramatically. Compared to the $\sim$ 1 min cooling time of a cyclotron resonator there is an immediate gain of several minutes per cycle just by switching to the fast $\sim$ Hz level coupling times of resonant sympathetic cooling. If cooled to less than one Kelvin, even with a large trap selective resonant sympathetic cooling could be competitive with the much colder temperatures of the much slower capacitive common endcap cooling.

10.1.5 Quantum Engineering and Quantum Information

With an optimized experiment even single ions could be used to prepare protons with cyclotron temperatures below 100 mK using the same procedure shown in Chapter 9. Critically, with such low temperatures there is a high probability, that the proton is prepared in the cyclotron ground state - opening up an entirely new frontier of measurements. Moreover, if the resonator is cooled close to the ground state, experiments can be performed to confirm basic quantum mechanical predictions with massive objects or constrain new decoherence theories [93, 104].

This probability of preparing particles with low quantum numbers is extremely important. In this system, beryllium has a rather uniquely low Doppler temperature of $\sim$ 500 µK while the ground state energy, $E = h\nu$, at 750 kHz is relatively high. As a result, this new method is competitive with electromagnetically induced transparency (EIT) cooling in which a large ion crystal can be prepared with motional quantum numbers around $\bar{n} \approx 0.3$ [105]. Particles could reasonably be prepared with probability $P(n = 0) > 0.1$ and offer a new possibility of cooling exotic species to the ground state or many particles to near the ground state, using only simple lasers. Such cooling could be useful for preparing many body systems for quantum simulation and with single ions possibly used for quantum simulation

itself [106].

Chapter 11

Conclusion

My thesis work began in 2016[1] when the g-factor measurement was first being set up. Since then the proton group at Mainz has both begun collecting data for this measurement, concluded this campaign, designed commissioned and ultimately demonstrated new methods with a next generation apparatus. This last part in particular was the focus of my thesis work. After cooling down the new apparatus in 2017 for the first time, we demonstrated a new (for us) ion production method with the laser ablation ion source that ultimately replaced the electron gun. Although this in turn caused additional problems and necessitated warming up and cooling down the apparatus several times it was an important experimental milestone. In addition, while the very first laser cooling signals came relatively quickly, it took a significant amount of time to collect new and compelling data such as the fluorescence data and the magnetic bottle temperature measurement. In the end, the minimum temperature of less than 3 K achieved during the magnetic bottle measurement is not the most impressive but commissioning the AT itself (several times) was a massive undertaking and troubleshooting the temperature measurement was a frustrating but rewarding experience.

Ironically, the measurements that I (and the rest of the team) are most proud of - those in Chapter 9 demonstrating sympathetic cooling with resonant coupling - were some of the easiest. We often reflected that we could have made our lives much, much easier by just coming up with the idea for these measurements a year or two earlier. Nevertheless, we are very happy with the outcome. With the resonant coupling technique we have demonstrated energy exchange between trapped particles separated by arbitrary distances. Moreover, we have used this energy exchange to reduce the temperature of the axial detection system to less than 20 % of the environment temperature and subsequently sympathetically cool a proton. This is the first realization of an idea from 30 years ago, before I was even born, and the culmination of decades of work. In the future, when technical

[1] as part of the 4+4 program in Heidelberg

problems with the apparatus are solved and upgrades added the temperature can even be reduced to a level enabling improved g-factor measurements and CPT tests - with immediate applicability to the antiproton. Even more, the broad applicability of this method suggests an even wider range of experiments could benefit.

With that I conclude my thesis. I hope this work proves useful to the Mainz group and to others. Precision penning-trap experiments are an invaluable part of precision physics and new techniques make them more relevant than ever.

Chapter 12

Appendix

For reference some important trap parameters are presented here, and there is naturally lots of overlap with the most recent thesis of the Mainz group from Georg Schneider [30]. As in there, the values of many of these parameters changed monthly, weekly, or even daily and are intended only as a approximate constants. In addition, the main results of this thesis were conducted in the PT (with ST connected to the same resonator) along with the AT so there is more focus on these parameters.

12.1 Hardware parameters

		PT	AT	ST	CT/BT
trap radius a	(mm)	4.5	1.8	2.5	2.0
ring electrode length l_r	(mm)	1.3099	0.4402	0.6656	0.5046
correction electrode length l_c	(mm)	3.5300	1.3309	1.9007	1.4937
endcap electrode length l_e	(mm)	9.0000	4.4780	3.7870	7.9480
effective electrode distance D_c	(mm)	10.0	4.2	5.7	4.6
effective electrode distance D_e	(mm)	25.6	9.7	14.1	10.9
effective electrode distance D_{c+e}	(mm)	7.2	2.9	4.1	3.2

Table 12.1

		PT	AT	ST	CT/BT
TR_{id}	(U)	0.8810	0.8804	0.8807	0.8806
ν_z	(kHz)	479	515	479	725
C_2	(m^{-2})	18 510	115 360	59 900	93 500
B_0	(T)	1.98	1.18	1.98	1.98
B_2	(Tm^{-2})	−0.39	297 000	-	-
D_4	(m^{-4})	1.28×10^9	4.98×10^{10}	1.34×10^{10}	3.27×10^{10}
$\kappa_{D_4,p}$	(Hz/K/mU)	45.4	-	-	-
$\kappa_{B_2,p}$	(Hz/K)	-8.6×10^{-5}	100	-	-
$\kappa_{B_2,Be}$	(Hz/K)	-	11	-	-

Table 12.2

12.2 Laser Cooling Parameters

- cooling transition: $2S_{1/2} \rightarrow 2P_{3/2}$
- cooling transition wavelength λ_L: 313.11 nm
- cooling transition frequency ν_L: 957.370 59 THz
- cooling transition natural linewidth Γ: 19 MHz
- laser linewidth linewidth Γ: < 100 MHz [88]

Bibliography

[1] S. Ulmer, C. Smorra, A. Mooser, et al. High-precision comparison of the antiproton-to-proton charge-to-mass ratio. *Nature*, 524(7564):196–199, 2015. doi: 10.1038/nature14861.

[2] G. Schneider, A. Mooser, M. Bohman, et al. Double-trap measurement of the proton magnetic moment at 0.3 parts per billion precision. *Science*, 358(6366): 1081–1084, 2017. ISSN 0036-8075. doi: 10.1126/science.aan0207.

[3] C. Smorra, S. Sellner, M. J. Borchert, et al. A parts-per-billion measurement of the antiproton magnetic moment. *Nature*, 550(7676):371–374, 2017. doi: 10.1038/nature24048.

[4] R. S. Van Dyck, P. B. Schwinberg, and H. G. Dehmelt. New high-precision comparison of electron and positron g factors. *Phys. Rev. Lett.*, 59:26–29, Jul 1987. doi: 10.1103/PhysRevLett.59.26.

[5] D.J. Heinzen and D.J. Wineland. Quantum-limited cooling and detection of radio-frequency oscillations by laser-cooled ions. *Physical Review A*, 42(5): 2977, 1990.

[6] N. Daniilidis, T. Lee, R. Clark, S. Narayanan, and H. Häffner. Wiring up trapped ions to study aspects of quantum information. *Journal of Physics B: Atomic, Molecular and Optical Physics*, 42(15):154012, jul 2009. doi: 10.1088/0953-4075/42/15/154012.

[7] M. J. Gutiérrez, J. Berrocal, F. Domínguez, et al. Dynamics of an unbalanced two-ion crystal in a Penning trap for application in optical mass spectrometry. *Phys. Rev. A*, 100:063415, Dec 2019. doi: 10.1103/PhysRevA.100.063415.

[8] M. Niemann, T. Meiners, J. Mielke, et al. Cryogenic ^{9}Be+ Penning trap for precision measurements with (anti-)protons. 31(3):035003, 2019. doi: 10.1088/1361-6501/ab5722.

[9] P. Micke, T. Leopold, S. A. King, et al. Coherent laser spectroscopy of highly charged ions using quantum logic. *Nature*, 578(7793):60–65, 2020. doi: 10.1038/s41586-020-1959-8.

[10] P. Pérez, D. Banerjee, F. Biraben, et al. The GBAR antimatter gravity experiment. *Hyperfine Interactions*, 233(1):21–27, 2015. doi: 10.1007/s10751-015-1154-8.

[11] A. Mooser, S. Ulmer, K. Blaum, et al. Direct high-precision measurement of the magnetic moment of the proton. *Nature*, 509(7502):596–599, 2014. doi: 10.1038/nature13388.

[12] L. Canetti, M. Drewes, and M. Shaposhnikov. Matter and antimatter in the universe. 14(9):095012, 2012. doi: 10.1088/1367-2630/14/9/095012.

[13] G. Lüders. On The Equivalence of Invariance Under Time Reversal and Under Particle-Antiparticle Conjugation for Relativistic Field Theories. *Dan. Mat. Fys. Medd.*, 28:1–17, 1954.

[14] B. Schwingenheuer, R. A. Briere, A. R. Barker, et al. *CPT* Tests in the Neutral Kaon System. *Phys. Rev. Lett.*, 74:4376–4379, May 1995. doi: 10.1103/PhysRevLett.74.4376.

[15] M. Ahmadi, B. X. R. Alves, C. J. Baker, et al. Investigation of the fine structure of antihydrogen. *Nature*, 578(7795):375–380, 2020. doi: 10.1038/s41586-020-2006-5.

[16] M. Ahmadi, B. X. R. Alves, C. J. Baker, et al. Characterization of the 1S–2S transition in antihydrogen. *Nature*, 557(7703):71–75, 2018. doi: 10.1038/s41586-018-0017-2.

[17] G. W. Bennett, B. Bousquet, H. N. Brown, et al. Final report of the E821 muon anomalous magnetic moment measurement at BNL. *Phys. Rev. D*, 73:072003, Apr 2006. doi: 10.1103/PhysRevD.73.072003.

[18] D. Colladay and V. A. Kostelecký. CPT violation and the standard model. *Phys. Rev. D*, 55:6760–6774, Jun 1997. doi: 10.1103/PhysRevD.55.6760.

[19] D. Colladay and V. Alan Kostelecký. Lorentz-violating extension of the standard model. *Phys. Rev. D*, 58:116002, Oct 1998. doi: 10.1103/PhysRevD.58.116002.

[20] Y. Ding and V. A. Kostelecký. Lorentz-violating spinor electrodynamics and Penning traps. *Phys. Rev. D*, 94:056008, Sep 2016. doi: 10.1103/PhysRevD.94.056008.

[21] Christian Smorra, Klaus Blaum, L Bojtar, et al. BASE–the baryon antibaryon symmetry experiment. *The European Physical Journal Special Topics*, 224(16):3055–3108, 2015.

[22] C. Smorra, Y. V. Stadnik, P. E. Blessing, et al. Direct limits on the interaction of antiprotons with axion-like dark matter. *Nature*, 575(7782):310–314, 2019. doi: 10.1038/s41586-019-1727-9.

[23] John R Pierce. Electron device of the magnetron type, January 14 1947. US Patent 2,414,121.

[24] L. S. Brown and G. Gabrielse. Geonium theory: Physics of a single electron or ion in a Penning trap. *Rev. Mod. Phys.*, 58:233–311, Jan 1986. doi: 10.1103/RevModPhys.58.233.

[25] G. Gabrielse, L. Haarsma, and S.L. Rolston. Open-endcap Penning traps for high precision experiments. *International Journal of Mass Spectrometry and Ion Processes*, 88(2):319 – 332, 1989. ISSN 0168-1176. doi: https://doi.org/10.1016/0168-1176(89)85027-X.

[26] Stefan Ulmer. *First Observation of Spin Flips with a Single Proton Stored in a Cryogenic Penning Trap*. PhD thesis, Ruperto-Carola University of Heidelberg, 7 2011.

[27] Florian Köhler. *Bound-Electron g-Factor Measurements for the Determination of the Electron Mass and Isotope Shifts in Highly Charged Ions*. PhD thesis, Ruperto-Carola University of Heidelberg, 7 2015.

[28] F. Heiße, F. Köhler-Langes, S. Rau, et al. High-Precision Measurement of the Proton's Atomic Mass. *Phys. Rev. Lett.*, 119:033001, Jul 2017. doi: 10.1103/PhysRevLett.119.033001.

[29] I. Arapoglou, A. Egl, M. Höcker, et al. g Factor of Boron-like Argon $^{40}Ar^{13+}$. *Phys. Rev. Lett.*, 122:253001, Jun 2019. doi: 10.1103/PhysRevLett.122.253001.

[30] Georg Schneider. *300 ppt Measurement of the Proton g-Factor*. PhD thesis, Johannes Gutenberg University Mainz, 12 2017.

[31] X. Feng, M. Charlton, M Holzscheiter, R.A. Lewis, and Y. Yamazaki. Tank circuit model applied to particles in a Penning trap. *Journal of Applied Physics*, 79:8 – 13, 02 1996. doi: 10.1063/1.360947.

[32] D. J. Wineland and H. G. Dehmelt. Principles of the stored ion calorimeter. *Journal of Applied Physics*, 46(2):919–930, 1975. doi: 10.1063/1.321602.

[33] S. Ulmer, J. Verdu, K. Blaum, et al. Currents Induced in Penning Trap Electrodes.

[34] Hans Dehmelt. Triton,... electron,... cosmon,...: An infinite regression? *Proceedings of the National Academy of Sciences*, 86(22):8618–8619, 1989. ISSN 0027-8424. doi: 10.1073/pnas.86.22.8618.

[35] D. Wineland, P. Ekstrom, and H. Dehmelt. Monoelectron Oscillator. *Phys. Rev. Lett.*, 31:1279–1282, Nov 1973. doi: 10.1103/PhysRevLett.31.1279.

[36] E. A. Cornell, R. M. Weisskoff, K. R. Boyce, and D. E. Pritchard. Mode coupling in a Penning trap: π pulses and a classical avoided crossing. *Phys. Rev. A*, 41:312–315, Jan 1990. doi: 10.1103/PhysRevA.41.312.

[37] Joseph Tan. *Cooperative Behavior in Cavity-cooled Parametrically-pumped Electron Oscillators*. PhD thesis, Harvard University, 9 1992.

[38] Hans Dehmelt. Continuous Stern-Gerlach effect: principle and idealized apparatus. *Proceedings of the National Academy of Sciences*, 83(8):2291–2294, 1986.

[39] A. Mooser, H. Kracke, K. Blaum, et al. Resolution of Single Spin Flips of a Single Proton. *Phys. Rev. Lett.*, 110:140405, Apr 2013. doi: 10.1103/PhysRevLett.110.140405.

[40] B. D'Urso, R. Van Handel, B. Odom, D. Hanneke, and G. Gabrielse. Single-Particle Self-Excited Oscillator. *Phys. Rev. Lett.*, 94:113002, Mar 2005. doi: 10.1103/PhysRevLett.94.113002.

[41] H. Nagahama, G. Schneider, A. Mooser, et al. Highly sensitive superconducting circuits at 700 kHz with tunable quality factors for image-current detection of single trapped antiprotons. *Review of Scientific Instruments*, 87(11):113305, 2016. doi: 10.1063/1.4967493.

[42] C. J. Foot. *Atomic physics*. Oxford University Press, 2005.

[43] W. M. Itano and D. J. Wineland. Laser cooling of ions stored in harmonic and Penning traps. *Phys. Rev. A*, 25:35–54, Jan 1982. doi: 10.1103/PhysRevA.25.35.

[44] D. Kielpinski, B. E. King, C. J. Myatt, et al. Sympathetic cooling of trapped ions for quantum logic. *Phys. Rev. A*, 61:032310, Feb 2000. doi: 10.1103/PhysRevA.61.032310.

[45] B. B. Blinov, L. Deslauriers, P. Lee, et al. Sympathetic cooling of trapped Cd^+ isotopes. *Phys. Rev. A*, 65:040304, Apr 2002. doi: 10.1103/PhysRevA.65.040304.

[46] M. D. Barrett, B. DeMarco, T. Schaetz, et al. Sympathetic cooling of $^9Be^+$ and $^{24}Mg^+$ for quantum logic. *Phys. Rev. A*, 68:042302, Oct 2003. doi: 10.1103/PhysRevA.68.042302.

[47] J. W. Britton, B. C. Sawyer, A. C. Keith, et al. Engineered two-dimensional Ising interactions in a trapped-ion quantum simulator with hundreds of spins. *Nature*, 484(7395):489–492, 2012.

[48] J. F. Goodwin, G. Stutter, R. C. Thompson, and D. M. Segal. Resolved-sideband laser cooling in a Penning trap. *Physical review letters*, 116(14): 143002, 2016.

[49] K. R. Brown, C. Ospelkaus, Y. Colombe, et al. Coupled quantized mechanical oscillators. *Nature*, 471(7337):196–199, 2011. doi: 10.1038/nature09721.

[50] M. Bohman, A. Mooser, G. Schneider, et al. Sympathetic cooling of protons and antiprotons with a common endcap Penning trap. *Journal of Modern Optics*, 65(5-6):568–576, 2018. doi: 10.1080/09500340.2017.1404656.

[51] Lowell S Brown. Geonium lineshape. *Annals of Physics*, 159(1):62 – 98, 1985. ISSN 0003-4916. doi: https://doi.org/10.1016/0003-4916(85)90192-7.

[52] C. Smorra and A. Mooser. Precision measurements of the fundamental properties of the proton and antiproton. In *Journal of Physics: Conference Series*, volume 1412, page 032001. IOP Publishing, 2020.

[53] P. J. Mohr, D. B. Newell, and B. N. Taylor. CODATA recommended values of the fundamental physical constants: 2014. *Rev. Mod. Phys.*, 88:035009, Sep 2016. doi: 10.1103/RevModPhys.88.035009.

[54] M. Schuh, F. Heiße, T. Eronen, et al. Image charge shift in high-precision Penning traps. *Phys. Rev. A*, 100:023411, Aug 2019. doi: 10.1103/PhysRevA.100.023411.

[55] R. X. Schüssler, H. Bekker, M. Braß, et al. Detection of metastable electronic states by Penning trap mass spectrometry. *Nature*, 581(7806):42–46, 2020. doi: 10.1038/s41586-020-2221-0.

[56] S. Rau, F. Heiße, Florian Köhler-Langes, et al. Penning trap mass measurements of the deuteron and the HD+ molecular ion. *Nature*, 585(7823):43–47, 2020. doi: 10.1038/s41586-020-2628-7.

[57] S. Sturm, A. Wagner, B. Schabinger, and K. Blaum. Phase-Sensitive Cyclotron Frequency Measurements at Ultralow Energies. *Phys. Rev. Lett.*, 107:143003, Sep 2011. doi: 10.1103/PhysRevLett.107.143003.

[58] D. M. Segal, M. Vogel, R. C. Thompson, and S. Bharadia. Dynamics of laser-cooled Ca+ ions in a Penning trap with a rotating wall. *Applied Physics B: lasers and optics*, 2012. doi: 10.1007/s00340-012-4871-6.

[59] Andreas Mooser. *Der g-Faktor des Protons*. PhD thesis, 12 2013.

[60] H. Nagahama, C. Smorra, S. Sellner, et al. Sixfold improved single particle measurement of the magnetic moment of the antiproton. *Nature Communications*, 8(1):14084, 2017. doi: 10.1038/ncomms14084.

[61] Stefan Ulmer. entwicklung eines experimentellen Aufbaus zur Messung des g-Faktors des Protons in einer Penning Falle, 2006.

[62] Y. Colombe, D. H. Slichter, A. C. Wilson, D. Leibfried, and D. J. Wineland. Single-mode optical fiber for high-power, low-loss UV transmission. *Opt. Express*, 22(16):19783–19793, Aug 2014. doi: 10.1364/OE.22.019783.

[63] C.D. Marciniak, H.B. Ball, A.T.H. Hung, and M.J. Biercuk. Towards fully commercial, UV-compatible fiber patch cords. *Opt. Express*, 25(14):15643–15661, Jul 2017. doi: 10.1364/OE.25.015643.

[64] M. Wiesinger, M. Bohman, V. Grunhofer, et al. Fluorescence Detection with Cryogenic Silicon Photomultipliers. In preparation.

[65] Markus Wiesinger. PhD thesis, Ruperto-Carola University of Heidelberg.

[66] M. Biroth, P. Achenbach, W. Lauth, and A. Thomas. Performance of sensl C-Series SiPM with high photoelectron resolution at cryogenic temperatures. In *2016 IEEE Nuclear Science Symposium, Medical Imaging Conference and Room-Temperature Semiconductor Detector Workshop (NSS/MIC/RTSD)*, pages 1–3, 2016.

[67] Valentin Grunhofer. Cyclotron cooling of a single proton in a Penning trap and improvements towards sympathetic cooling. Master's thesis, Johannes Gutenberg University Mainz, 7 2020.

[68] Natalie Schön. Optimizing catching efficiencies of antiprotons in a Penning trap and Developments towards resonant coupling of single protons and laser cooled beryllium ions. Master's thesis, Johannes Gutenberg University Mainz, 4 2018.

[69] Sven Sturm. *The g-factor of the electron bound in* $^{28}Si^{13+}$*: The most stringent test of bound-state quantum electrodynamics.* PhD thesis, Johannes Gutenberg-Universität Mainz, 12 2011.

[70] Sven Sturm. personal communication.

[71] S. Sellner, M. Besirli, M. Bohman, et al. Improved limit on the directly measured antiproton lifetime. *New Journal of Physics*, 19(8):083023, aug 2017. doi: 10.1088/1367-2630/aa7e73.

[72] I. Sukuba, A. Kaiser, S. E. Huber, J. Urban, and M. Probst. Energetics and reactivity of small beryllium deuterides. *Journal of molecular modeling*, 23(7): 203–203, 07 2017. doi: 10.1007/s00894-017-3362-4.

[73] D. B. Pinegar, S. L. Zafonte, and R. S. Van Dyck. The UW-PTMS. *Hyperfine Interactions*, 174(1):47–53, 2007. doi: 10.1007/s10751-007-9563-y.

[74] Kurt Franke. The BASE Experiment and Analysis Tools for G-Factor Resonances. unpublished, 2015.

[75] L. Deslauriers, S. Olmschenk, D. Stick, et al. Scaling and Suppression of Anomalous Heating in Ion Traps. *Phys. Rev. Lett.*, 97:103007, Sep 2006. doi: 10.1103/PhysRevLett.97.103007.

[76] I. A. Boldin, A. Kraft, and C. Wunderlich. Measuring Anomalous Heating in a Planar Ion Trap with Variable Ion-Surface Separation. *Phys. Rev. Lett.*, 120:023201, Jan 2018. doi: 10.1103/PhysRevLett.120.023201.

[77] M. J. Borchert, P. E. Blessing, J. A. Devlin, et al. Measurement of Ultralow Heating Rates of a Single Antiproton in a Cryogenic Penning Trap. *Phys. Rev. Lett.*, 122:043201, Jan 2019. doi: 10.1103/PhysRevLett.122.043201.

[78] M.I. Krivoruchenko, Fedor Šimkovic, Dieter Frekers, and Amand Faessler. Resonance enhancement of neutrinoless double electron capture. *Nuclear Physics A*, 859(1):140 – 171, 2011. ISSN 0375-9474. doi: https://doi.org/10.1016/j.nuclphysa.2011.04.009.

[79] M. Harlander, M. Brownnutt, W. H.änsel, and R. Blatt. Trapped-ion probing of light-induced charging effects on dielectrics. *New Journal of Physics*, 12(9): 093035, sep 2010. doi: 10.1088/1367-2630/12/9/093035.

[80] M. Brownnutt, M. Kumph, P. Rabl, and R. Blatt. Ion-trap measurements of electric-field noise near surfaces. *Rev. Mod. Phys.*, 87:1419–1482, Dec 2015. doi: 10.1103/RevModPhys.87.1419.

[81] D. J. Berkeland, J. D. Miller, J. C. Bergquist, W. M. Itano, and D. J. Wineland. Minimization of ion micromotion in a Paul trap. *Journal of Applied Physics*, 83(10):5025–5033, 2020/09/25 1998. doi: 10.1063/1.367318.

[82] T. Andersen, K. A. Jessen, and G. Sørensen. Mean-Life Measurements of Excited Electronic States in Neutral and Ionic Species of Beryllium and Boron. *Phys. Rev.*, 188:76–81, Dec 1969. doi: 10.1103/PhysRev.188.76.

[83] D. J. Wineland, J. C. Bergquist, Wayne M. Itano, and R. E. Drullinger. Double-resonance and optical-pumping experiments on electromagnetically confined, laser-cooled ions. *Opt. Lett.*, 5(6):245–247, Jun 1980. doi: 10.1364/OL.5.000245.

[84] W. M. Itano and D. J. Wineland. Precision measurement of the ground-state hyperfine constant of $^{25}Mg^{+}$. *Phys. Rev. A*, 24:1364–1373, Sep 1981. doi: 10.1103/PhysRevA.24.1364.

[85] H. F. Powell, D. M. Segal, and R. C. Thompson. Axialization of Laser Cooled Magnesium Ions in a Penning Trap. *Phys. Rev. Lett.*, 89:093003, Aug 2002. doi: 10.1103/PhysRevLett.89.093003.

[86] E. S. Phillips, R. J. Hendricks, A. M. Abdulla, et al. Dynamics of axialized laser-cooled ions in a Penning trap. *Phys. Rev. A*, 78:032307, Sep 2008. doi: 10.1103/PhysRevA.78.032307.

[87] Sandro Kraemer. *Towards Laser Cooling of Beryllium Ions at the ALPHA-TRAP Experiment*. PhD thesis, Ruperto-Carola University of Heidelberg, 2017.

[88] Alexander Egl. *High-Precision Laser Spectroscopy of the Fine Structure in $^{40}Ar^{13+}$ at ALPHATRAP*. PhD thesis, Ruperto-Carola University of Heidelberg, 4 2020.

[89] W. Nagourney, G. Janik, and H. Dehmelt. Linewidth of Single Laser-Cooled 24Mg+ Ion in Radiofrequency Trap. *Proceedings of the National Academy of Sciences of the United States of America*, 80(2):643–646, 1983. ISSN 00278424.

[90] Z. Andelkovic, R. Cazan, W. Nörtershäuser, et al. Laser cooling of externally produced Mg ions in a Penning trap for sympathetic cooling of highly charged ions. *Phys. Rev. A*, 87:033423, Mar 2013. doi: 10.1103/PhysRevA.87.033423.

[91] C. Monroe, D. M. Meekhof, B. E. King, et al. Resolved-Sideband Raman Cooling of a Bound Atom to the 3D Zero-Point Energy. *Phys. Rev. Lett.*, 75: 4011–4014, Nov 1995. doi: 10.1103/PhysRevLett.75.4011.

[92] B. Srivathsan, M. Fischer, L. Alber, et al. Measuring the temperature and heating rate of a single ion by imaging. *New Journal of Physics*, 21(11):113014, nov 2019. doi: 10.1088/1367-2630/ab4f43.

[93] S. Kotler, R. W. Simmonds, D. Leibfried, and D. J. Wineland. Hybrid quantum systems with trapped charged particles. *Phys. Rev. A*, 95:022327, Feb 2017. doi: 10.1103/PhysRevA.95.022327.

[94] L. Qiu, I. Shomroni, P. Seidler, and T. J. Kippenberg. Laser Cooling of a Nanomechanical Oscillator to Its Zero-Point Energy. *Phys. Rev. Lett.*, 124: 173601, Apr 2020. doi: 10.1103/PhysRevLett.124.173601.

[95] J. Chan, T. P. M. Alegre, A. H. Safavi-Naeini, et al. Laser cooling of a nanomechanical oscillator into its quantum ground state. *Nature*, 478(7367): 89–92, 2011. doi: 10.1038/nature10461.

[96] Felix Hahne. *Investigation of a Novel Method for Sympathetic Laser Cooling of Highly Charged Ions in a Penning Trap*. PhD thesis, Ruperto-Carola University of Heidelberg, 2020.

[97] S. M. Brewer, J.-S. Chen, A. M. Hankin, et al. $^{27}Al^{+}$ Quantum-Logic Clock with a Systematic Uncertainty below 10^{-18}. *Phys. Rev. Lett.*, 123:033201, Jul 2019. doi: 10.1103/PhysRevLett.123.033201.

[98] F. Wolf, Y. Wan, J.C. Heip, et al. Non-destructive state detection for quantum logic spectroscopy of molecular ions. *Nature*, 530(7591):457–460, 2016. doi: 10.1038/nature16513.

[99] T. Meiners, M. Niemann, J. Mielke, et al. Towards sympathetic cooling of single (anti-)protons. *Hyperfine Interactions*, 239(1):26, 2018. doi: 10.1007/s10751-018-1502-6.

[100] G. Stutter, P. Hrmo, V. Jarlaud, et al. Sideband cooling of small ion Coulomb crystals in a Penning trap. *Journal of Modern Optics*, 65(5-6):549–559, 03 2018. doi: 10.1080/09500340.2017.1376719.

[101] S. Rainville, J. K. Thompson, E. G. Myers, et al. A direct test of E=mc2. *Nature*, 438(7071):1096–1097, 2005. doi: 10.1038/4381096a.

[102] D. R. Crick, H. Ohadi, I. Bhatti, R. C. Thompson, and D. M. Segal. Two-ion Coulomb crystals of Ca+ in a Penning trap. *Opt. Express*, 16(4):2351–2362, Feb 2008. doi: 10.1364/OE.16.002351.

[103] S. Lohse, J. Berrocal, S. Böhland, et al. Quartz resonators for penning traps toward mass spectrometry on the heaviest ions. *Review of Scientific Instruments*, 91(9):093202, 2020/10/12 2020. doi: 10.1063/5.0015011.

[104] Oriol Romero-Isart. Quantum superposition of massive objects and collapse models. *Phys. Rev. A*, 84:052121, Nov 2011. doi: 10.1103/PhysRevA.84.052121.

[105] E. Jordan, K.A. Gilmore, A. Shankar, et al. Near Ground-State Cooling of Two-Dimensional Trapped-Ion Crystals with More than 100 Ions. *Phys. Rev. Lett.*, 122:053603, Feb 2019. doi: 10.1103/PhysRevLett.122.053603.

[106] M. Raghunandan, G. Wolf, C. Ospelkaus, P. O. Schmidt, and H. Weimer. Initialization of quantum simulators by sympathetic cooling. *Science Advances*, 6(10):eaaw9268, 03 2020. doi: 10.1126/sciadv.aaw9268.

Acknowledgments

None of this of course would have been possible without the hard work and support of many people and I'm grateful for all them. Thank you!

My supervisor Klaus Blaum has been extremely supportive throughout the entire PhD process. If there ever a need for anything he would answer quickly and make sure we were able to continue. There was a period of time when results were extremely hard to attain and Klaus assured me that they would come - eventually they did and I'm thankful for his confidence and support.

Stefan Ulmer was a huge help with the physics and the experiment. His knowledge and experience were very valuable and as was his constant support. I especially appreciate his empathy while setting up the AT - looking at an FFT screen trying to find signals out of nothing makes you feel like you're losing your mind and Stefan was able to commiserate.

To both Klaus and Stefan, thank you also for your support professionally an helping me develop as a physicist.

Christian Smorra has been helpful beyond belief in taking analyzing the biggest results in this thesis. Thank you for putting up with me throughout all of this and for putting in a ton of work when it really mattered. And of course, when the experiment or writing was driving me insane I really appreciated having you to talk to.

Andi Mooser and Georg Schneider were both great to work with and critical in building an experiment that actually worked. Their experience and hard work during the early days of the new experiment I'm really glad to have had them around.

Markus Wiesinger has taught me a lot and is an excellent physicist. Both of us have had challenging PhDs but I'm extremely grateful for his patience and ability to drive the experiment forward. We put in lots of hours together assembling and disassembly the experiment and I had lots fun. Thank you for everything and I wish you the best in upcoming measurements.

Christian Will has been a great office mate and was kind enough to let

share the office with me while I was writing despite the pandemic. His work with simulations has been really valuable and gave him a fresh perspective that we all needed.

The proton team has grown and shrunk over the years but I also want to thank Natalie Schön, Marcel Gerhard, and Valentin Grunhofer.

Of course the larger Mainz trapping group has also been lots of fun to be around, to go to lunch with (back when that was possible), and discuss physics and everything else. A big thank you to LIONTRAP - Florian Köhler-Langes, Sacha Rau, Fabian Heiße, Sven Sturm, and Sangeetha Puthukodath as well as the STEP masters' students Daniel Popper and Steffen Gavranovic.

The rest of the BASE team at CERN and the other Penning trap groups at MPIK were also great to work with and fun to be around.

A special thank you as well to James Harrington for commiserating with me about everything. He has been a great friend throughout all of this and helped keep me (relatively) sane.

And finally my friends family back home has been hugely supportive during my time in Germany. I'm very thankful Branden Livermore and Dylan Monroe in particular and for my parents Mark and Lisa Bohman and my sisters Kelsey Smith and Karley Durst. The person I can never thank enough is my mom, Sandy Bohman, who has always been there for me. I will never forget the last minute trip she took to Mainz to spend Thanksgiving with me - thank you!